ARTIFICIAL GUT SIMULATOR FOR SIMULTANEOUS EVALUATION OF DRUG DISSOLUTION AND ABSORPTION

A DISSERTATION

SUBMITTED TO THE FACULTY OF THE

UNIVERSITY OF MINNESOTA

BY

Krutika Harish Jain

IN PARTIAL FULFILLMENT OF THE REQUIREMENTS

FOR THE DEGREE OF

DOCTOR OF PHILOSOPHY

Advisor

Ronald A. Siegel, ScD

August 2021

Acknowledgements

I would like to thank Dr. Ronald A. Siegel for his excellent tutelage, unwavering support and encouragement during my graduate studies. I have always been inspired by his fierce curiosity and by the breadth of his knowledge that extends far beyond the realm of pharmaceutical sciences.

I would like to extend my gratitude to Genentech Inc. for funding this research. I would also like to thank our collaborator, Dr. Helen Hao Hou for her invaluable inputs throughout this study. Her expertise in the field of drug solid- and solution-state characterization is unparalleled, and it was a privilege to work with her.

I would like to thank Ishaan Duggal for laying a foundation for pharmacokinetic model development of BCS-II drug molecules and making crystalline solubility measurements of the model drugs used in this study. I am also grateful to Kiki Gai for assisting me with designing and fabricating prototypes of osmotic implant as a part of my non-thesis project. I'd like to thank past and current Siegel and Sury lab members, Dr. Davin Rautiola, Xueyao Hu, Dr. Anasuya Sahoo, Dr. Michelle Fung, Dr. Kweku Konadu, Dr. Allison Siehr, Ceren Karahan, Dr. Ahmad Hivechi, Dr. Muhammed Safdar, Dr. Naveen Thakral, Dr. Seema Thakral, Joel Updyke, Jayesh Sonje and Sichen Song, for routinely providing helpful feedback and invaluable insights. I would especially like to thank Dr. Allison Siehr for being extremely resourceful with analytical instruments and her technical knowledge.

A very special thanks to Steven Thomalla, Cara Piazza, Grace Aysta and Geoffrey Dybicz for maintaining an excellent facility at the Earl E. Bakken Medical Devices Center and for training me in various rapid prototyping techniques that were used to develop the initial prototypes and final product of the artificial gut simulator. Part of the gut simulator fabrication was also carried out at the Anderson Student Innovation Labs. Amorphous solid dispersion preparation and solid-state characterization were performed in Dr. Raj Suryanarayanan's lab with assistance from Dr. Michelle Fung, Dr. Kweku Konadu, Dr. Sampada Korrane, Rahul Lalge and Jinghan Li. Polarized light microscopy studies and cryo-milling were carried out in Dr. Changquan Calvin Sun's lab with assistance from Dr. Chenguang Wang. Fluorescence spectroscopy studies were performed in Dr. Courtney

Aldrich's lab with assistance from Dr. Neeraj Mishra and Pooja Hegde. Ultracentrifugation was carried out in Dr. Gregory Connell's lab. Nanoparticle tracking analysis was conducted at the Minnesota Nano Center with assistance from Dr. James Marti.

I am grateful for the financial support in the form of Bighley Graduate Fellowship (2017-2018, 2018-2019) and Rowell Fellowship (2018-2019). I would like to thank the faculty, staff and students of the Department of Pharmaceutics for their support in all my endeavors.

I feel extremely fortunate to have a big family and for every single one for being a pillar of strength and support throughout my grad school journey in the United States. Thank you, Mom, for being so wonderful, for pushing me to excel since I can remember, for working so hard on me and with me and for all your sacrifices. Thank you, Dad, for going above and beyond in all your endeavors, for inspiring and for teaching me a valuable lesson of adding 'value' to everyone's lives and work. I'm immensely grateful to my grandparents for being visionaries, for breaking the many shackles laid by the society so that I could fulfil my dreams, and for just being my best friends. Dadiji, your absence is so palpable, and I miss you dearly every single day.

Special thanks to Dr. Chandrashekar, Dr. Ranjini, Yogesh, Sonu, Neelu, Sharada and Madhulika for being my home away from home. I'd also like to thank my wonderful friends in Bangalore, Boston and Seattle for just being a call away. I am also so grateful to my cats, Ginger and Ale, for being my constant source of endorphins since 2017 and helping me in ways they'll never know.

Finally, I'd like to thank Dr. Ronald A. Siegel (advisor), Dr. Raj Suryanarayanan (chair), Dr. William Elmquist and Dr. David Wood for agreeing to serve on my thesis committee, for their valuable feedback during my preliminary oral examination and for setting aside time from their busy schedules to review my dissertation and participate in my oral defense.

Dedication

To Shiv.

Abstract

Over the past three decades, high-throughput screening has resulted in a discovery pipeline consisting mostly of highly potent but lipophilic compounds exhibiting poor aqueous solubility and classified as Biopharmaceutics Classification System (BCS) Class II. Since poor solubility limits absorption and bioavailability, efforts have been made to develop supersaturating delivery systems such as amorphous solid dispersions (ASD) that enhance the apparent solubility of the drug without sacrificing its thermodynamic activity. The performance of these dispersions is often tested in 'closed', non-sink compendial dissolution testing apparatus that lacks an absorptive sink. The supersaturated solution generated upon ASD dissolution is metastable with respect to the stable crystalline phase and can undergo amorphous and/or crystalline precipitation. The rate of precipitation depends upon the degree of supersaturation.

In the absence of absorption, during non-sink dissolution testing, high supersaturation can drive more precipitation than that which occurs *in vivo* where continuous drug absorption from the intestinal lumen decreases drug concentration, which in turn decreases the driving force for precipitation. Unsurprisingly, many *in vitro* studies with non-sink dissolution testing have failed to predict the *in vivo* performance of formulations of BCS-II drugs, which by definition, have high intestinal permeability. A simultaneous dissolution and absorption testing apparatus called the side-by-side diffusion cell allows drug to diffuse from the donor to a receiver compartment across a membrane that separates the two. However, small surface area of the membrane results in very low rates of drug absorption and very long, unphysiological experimental time scales.

The first goal of this study was to develop and validate an artificial gut simulator apparatus (AGS) consisting of a hollow fiber-based absorption module suspended in the drug donor. The hollow fibers provide a large surface area for absorption, significantly improving mass transfer rate of drugs from the donor into the aqueous receiver media in the hollow fiber lumen. Continuous pumping of the drug-free receiver media into the lumen helps maintain an absorptive sink. A theory for mass transfer across the hollow fiber membrane was developed and validated using caffeine. Physiological rate of drug

absorption was attained by tuning the AGS operating parameters per the theoretical model. This is an important step in developing a biorelevant test for BCS-II drugs.

The next goal of this project was to understand how absorption impacts dissolution of ASDs and subsequent crystallization from supersaturated solutions of a model BCS-II compound, ketoconazole. Relative to a non-sink 'control', continuous drug removal by absorption enhanced ASD dissolution and significantly decreased both amorphous and crystalline precipitation. This can be attributed to both a decreased driving force for precipitation due to lower drug concentration in the AGS donor as well as to redissolution of any precipitate that is formed to replenish the drug in solution lost to absorption. On the other hand, polymer excipient added to the ASD to stabilize the drug against crystallization during storage and dissolution reduced the drug's absorption rate by possibly interacting favorably with the free drug species and reducing the drug's thermodynamic activity. Simple analytical techniques used in conjunction with the AGS helped decouple and understand the impact of dissolution, precipitation and speciation on absorption and vice-a-versa.

The final goal of this project was to implement a scheme to establish *in vitro/in vivo* correlation with another BCS-II drug, dipyridamole, by inputting the drug concentration absorbed by the AGS receiver media into a compartment-based disposition model to ultimately predict the *in vivo* plasma concentration-time profile of the drug. The human intestinal absorption rate constant of dipyridamole, determined from Caco-2 cell monolayer permeability coefficient, was used to tune the AGS. Gastric emptying was simulated at a physiological rate to ensure a physiological rate of supersaturation generation as the weakly basic dipyridamole is solubilized and emptied from acidic gastric compartment into a neutral duodenum. This methodology of simulating gastric emptying and absorption enabled accurate prediction of drug *in vivo* intestinal and plasma concentration-time profiles. This approach and apparatus is anticipated to be of great utility during drug product development for screening and optimization of potential oral formulations.

Table of Contents

List of Figures

List of Tables

Chapter 1: Introduction

1.1 Background

1.1.1 Physical chemistry of supersaturated solutions

Oral drug administration, to date, remains the most preferred and common route of drug delivery. Following oral administration, the drug first dissolves in the gastrointestinal (GI) media and then permeates across the GI membrane to enter systemic circulation. Per Lipinski's 'Rule of Five', proposed more than two decades ago, the desirable physicochemical properties for efficient oral delivery include high aqueous solubility and high phospholipid membrane permeability.[1]

However, in the last three decades, powerful computational chemistry and high-throughput screening technologies employed in the drug discovery phase have resulted in a pipeline consisting mostly of highly potent but lipophilic, large molecular weight compounds that exhibit poor aqueous solubility.[1–4] The Biopharmaceutics Classification System (BCS) categorizes drugs into four classes based on their solubility and permeability. BCS-II drugs include those with low aqueous solubility and high intestinal membrane permeability, and now constitute 40% of the marketed drugs and 90% of new drug candidates.[5]

To improve oral bioavailability, several formulation strategies have been adopted that have a theoretical basis in the Noyes-Whitney equation coupled with the Nernst-Brunner diffusion layer model which describes dissolution of a solid.[6]

$$\frac{dM}{dt} = \frac{DA}{h}(C_s - C) \tag{1.1}$$

Eq. (1.1) states that the rate of drug dissolution from a tablet particle is a function of the surface area *A* that is available for dissolution, the concentration gradient between the tablet surface (drug solubility, C_s) and bulk of the solution (C) as well as boundary layer thickness *h* and diffusion coefficient *D*. Now *D* and *h* are somewhat beyond the control of the formulation scientist. They depend on the media that is available in the gut and the existing hydrodynamics. As a result, many solubility enhancing formulation strategies to improve C_s have emerged. The most common approaches used in the marketed products include incorporation of cosolvents, surfactants and cyclodextrins and formulation of salts, polymorphs, cocrystals, lipid-based systems, and amorphous solids.[7] These strategies result in an enhanced solution concentration either by increasing the drug's equilibrium solubility or by generating supersaturated solutions.

The fundamental difference between a solubilized solution and a supersaturated solution is the thermodynamic activity of the drug in solution; in a supersaturated solution, by definition, it exceeds the thermodynamic activity of the crystalline drug, while in a solubilized solution, the thermodynamic activity of the drug remains at or below that of the crystalline form.[6] Thermodynamic activity refers to the free or unbound fraction of the drug in solution. The other species include drug molecules bound to solubilizing excipients such as cyclodextrin complexes, surfactants micelles and cosolvents.

It is now widely recognized that only the free drug molecules provide the driving force for absorption and that solubilization by micelles and complexes can lead to a reduction in the absorption rate.[8,9] For instance, Miller et al. demonstrated that with an increase in sodium lauryl sulfate and sodium taurocholate concentration beyond the critical micelle concentration, a decrease in permeability of progesterone in a single-pass rat jejunal

perfusion assay was observed.[10] This lack of correlation between solubility and permeability is known as the "solubility-permeability" interplay wherein the increased apparent solubility of a drug is alone insufficient to result in an increase in oral bioavailability.[10–14]

Formulation strategies like amorphization of the crystalline drug to generate high free energy state and disordered lattice structures, on the other hand, can lead to a remarkable enhancement of dissolution rate and dissolved drug concentrations. The supersaturated solutions result in an increased fraction of free drug available, or in other words, enhanced thermodynamic driving force, for absorption.[6] The concentration of the dissolved drug, however, cannot exceed a critical miscibility concentration or the *amorphous solubility* of the drug in a given aqueous media.[6]

Amorphous solubility is the concentration of drug attained in solution following equilibration between the solution phase and amorphous material.[6] Strictly speaking, such an equilibrium is impossible since the crystalline material is the thermodynamically stable form and the high free energy amorphous polymorph or the metastable supersaturated solution will crystallize into the next stable polymorph as per Ostwald's rule of stages.[15–17] However, if crystallization is slow, then a metastable equilibrium can exist between the amorphous material and crystalline solid, which enables determination of amorphous solubility.[6] The amorphous solubility advantage has resulted in the commercial success of many drugs. For example, amorphous glibemclamide displayed 14 times higher solubility than its crystalline form in an aqueous buffer.[18] Likewise, amorphous pranlukast had enhanced its solubility by approximately 5.8 times in water and 19.4 times in phosphate buffer saline over the crystalline polymorph.[19]

However, the inherent instability of the amorphous form caused by high free energy remains a major barrier to its widespread adoption as a formulation strategy. Amorphous solids are typically stabilized by formulating homogeneous dispersions with polymers. Such formulations are known as *amorphous solid dispersions* (ASDs).[20] Polymers increase the stability of the solid amorphous form during manufacturing and storage as well as of supersaturated solutions upon ASD dissolution by various mechanisms, such as forming a physical barrier to prevent aggregation of drug molecules, decreasing the configurational entropy, decreasing the drug's thermodynamic activity through favorable drug-polymer interactions, and decreasing the drug's molecular mobility by increasing the formulation's glass transition temperature (T_g).[21] Nontoxic polymers including polyvinylpyrrolidone (PVP), hypromellose (HPMC), polyvinylpyrrolidone/vinyl acetate (PVP/VA), and hypromellose acetate succinate (HPMCAS) have been approved to use as excipients by the United States Food and Drug Administration (FDA) for oral dosage forms and have been adopted to manufacture several commercial ASDs.[21] In spite of the stabilizing polymer, upon ASD dissolution, the metastable supersaturated solution generated in the GI media is susceptible to precipitation, the rate and type of which depends upon the degree of supersaturation.

Amorphous precipitation or liquid-liquid phase separation (LLPS) refers to the separation of a metastable, drug-rich amorphous phase when the concentration of drug added to the media exceeds its amorphous solubility.[6] The separated phase is mostly in the liquid state since the amorphous phase in contact with the aqueous phase absorbs moisture which results in a reduction of its T_g below the physiological body temperature (there are

drug molecules whose separated amorphous phase does not exhibit a reduction in T_g, in which case the precipitation phenomenon is called glass-liquid phase separation[22]).

It has been previously observed that the solute chemical potential or thermodynamic activity, a_{aq}, and therefore, the flux, J, across a membrane increases linearly with an increase in supersaturated solution concentration up till the onset of LLPS or amorphous solubility concentration, S [Eq. (1.2)-(1.4)].[14]

$$J = \frac{DA}{h}\frac{a_{aq}}{\gamma_m} \tag{1.2}$$

$$\left.\begin{aligned} C &< S \\ a_{aq} &= \gamma_{aq} C \end{aligned}\right\} \tag{1.3}$$

$$\left.\begin{aligned} C &\geq S \\ a_{aq} &= \gamma_{aq} S \end{aligned}\right\} \tag{1.4}$$

where C is the apparent drug concentration and γ_{aq} is the activity coefficient of the drug in the aqueous media. The drug flux also depends on the drug diffusion coefficient, D, membrane surface area, A, and thickness, h, for absorption and activity coefficient of the drug in the membrane γ_m.

Further increase in concentration does not lead to an increase in flux due to amorphous precipitation. Instead, a constant flux is observed.[23] However, the separated amorphous phase, due to its high free energy and large surface area in contact with the aqueous media, is in dynamic equilibrium with the free drug, serving as a reservoir and rapidly redissolving to replenish the drug in solution lost to absorption.[24,25]

Separation of the liquid into two phases results in a less energetic system than the initial homogeneous highly supersaturated system but still does not afford the lowest energy state which is a stable crystal in equilibrium with the saturated solution.[6] The transient, metastable drug-rich phases would eventually transform into thermodynamically stable crystals.[6] Several possible transformation pathways are schematically summarized in ***Figure 1.1***.[5] This, however, still does not present a complete picture. The drug-rich phases may grow, coalesce, or aggregate to further reduce the free energy of the system.[5] For example, the diameter of drug-rich phases in the supersaturated danazol aqueous solution was shown to increase with time when monitored using dynamic light scattering (DLS).[26] Similarly, Ricante et al. showed that the metastable amorphous nanodroplets present in a supersaturated phenytoin-HPMCAS aqueous solution aggregated into irregularly shaped droplets prior to the formation of crystals, as measured by cryo-TEM and SAXS.[27] Although the growth, coalescence or aggregation of metastable phases is favored over the formation of crystalline nuclei due to the smaller free energy barrier (Ostwald's rule of stages), nucleation will still occur, most likely within the drug-rich phases where a higher supersaturation with respect to the crystalline solubility is present, which will in turn trigger its transformation into thermodynamically stable crystalline phases.[5] For example, the transformation of metastable amorphous probucol nanoparticles into crystalline ones was indicated by a gradual increase in the particle stiffness measured by atomic force microscopy (AFM).[28] Similarly, crystallization within transient drug-rich nanodroplets was revealed in the nifedipine-HPMCAS supersaturated solution using NMR.[29,30] Upon onset of crystallization, the concentration of the drug decreased in the solution, whereas the concentration of polymer increased. Interestingly, these results indicate the HPMCAS

polymer was distributed in the drug-rich phase, which might assist the formation of such phase as well as inhibit the crystallization within it.

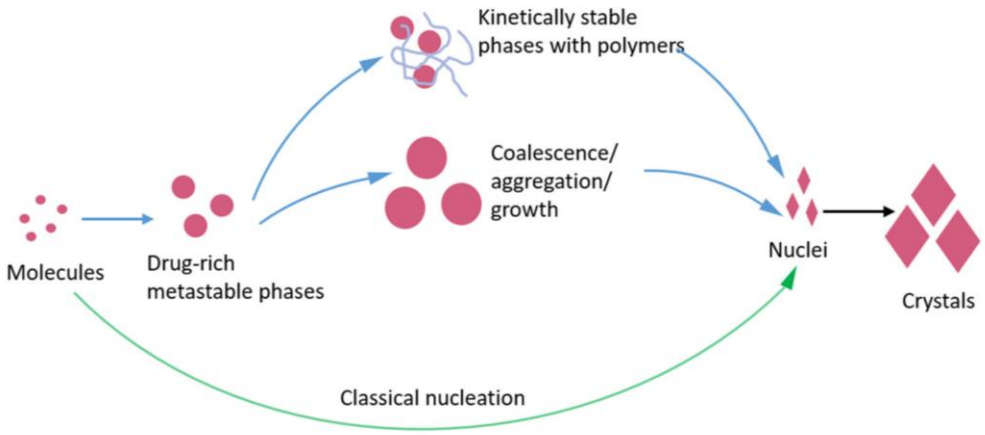

Figure 1.1. Schematic illustration of the possible nucleation pathways (classical or non-classical) of drug in a solution.[5]

Transformation of the metastable drug-rich phases into crystals is a thermodynamically inevitable process, but the kinetics of this process can be significantly altered by the presence of certain excipients such as polymers, so that precipitation from supersaturated solutions may not be observed within a reasonable experimental timescale. For example, Ueda et al. suggested that an increase in steric and electrostatic repulsion between amorphous nanodroplets caused by surface adsorption of certain polymers can significantly reduce the rate of nanodroplet aggregation and growth.[31] The suppressing effects can be varied by the choice of excipient materials, as demonstrated with the PVP, HPMC and its derivative HPMCAS in the danazol-rich nanodroplet system. Moreover, many polymers have been observed to inhibit the formation of crystalline nuclei or their

subsequent growth within the drug-rich phases. Jha et al. investigated the drug and excipient performance in aqueous solutions using all-atom molecular dynamics simulations, where the effect of excipients on the mobility of drugs can be screened.[32] They found that the aggregation and diffusivity of phenytoin can be reduced by as much as five orders of magnitude by the presence of HPMC and HPMCAS, indicating a significant role of excipient in reducing the transformation kinetics of metastable drug-rich phases during the dissolution of ASD.

1.1.2 In vivo dissolution and absorption of insoluble drugs from ASDs

When solid dosage forms are administered orally, the drug needs to dissolve in the human gastrointestinal fluids before the drug molecules can be absorbed into the systemic circulation and subsequently be transported to the site(s) of action. The human gastrointestinal fluid, however, is a complex milieu consisting of water, micelle-forming surfactants such as bile acids and lecithin and lipids.[6] The media is buffered and highly dynamic. For example, the amount of bile acid and lipid secretion varies depending on food intake. In addition the media may contain food components as well as excipients released from pharmaceutical dosage forms.[6] The highly complex and dynamic human GIT presents significant difficulties in understanding the dissolution and subsequent in vivo performance of pharmaceutical oral dosage forms.[6] Conceptually, however, we can simplify the system to aid understanding. As shown in ***Figure 1.2***, we can view the human GIT as a collection of interconnected "compartments".[6] The central compartment is the aqueous compartment into which drug dissolves and from which passive absorption of only unionized, unbound drug species can take place across the intestinal epithelium.[33] Here, an equilibrium can

exist between ionized and unionized drug depending on the pK_a of the molecule and the microenvironment pH. Peripheral to the central aqueous compartment, there are many other compartments or microenvironments that the bound drug can reside in. The drug in the peripheral compartments is not directly available for absorption. However, these compartments can act as reservoirs whereby drug will dissociate from these compartments into the central compartment to replenish the free drug that is lost to absorption. If dissolution from the dosage forms leads to supersaturated aqueous solutions, the drug can crystallize or undergo LLPS and that can eventually also redissolve to replenish drug in solution lost to absorption.

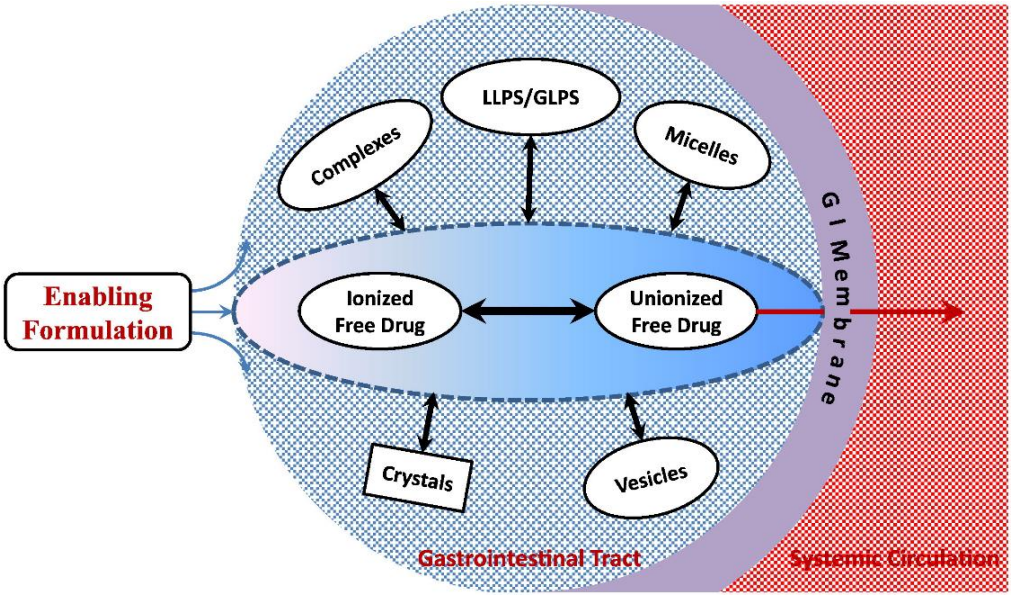

Figure 1.2. Schematic representation of ASD dissolution, gastrointestinal exchange processes and passive drug uptake.[6]

1.1.3 In vitro Dissolution Testing of ASDs

For oral solid dosage forms, the dissolution profile is an important in vitro characteristic of a formulation under development. Compendial dissolution testing, defined by the United States Pharmacopeia (USP), is widely used to obtain information during drug product development process such as selection of appropriate excipients or a suitable solid form of the compound for the desired dissolution profile.[34] USP I (basket), II (paddle) and III (reciprocating cylinder) apparati, most commonly used for dissolution testing, had been primarily developed for routine quality control and batch release with little consideration to biorelevance.[35] However, with the FDA's specification to minimize bioavailability testing in humans, clinical scientists place increasing reliance on biorelevant *in vitro* dissolution testing in combination with mathematical modeling to predict *in vivo* performance.[36] Physiological conditions such as fluid volume, media composition, hydrodynamics and transit time can have significant influence on the rate of dissolution and concentration of drug available for absorption. Significant efforts have been made towards understanding and mimicking *in vivo* hydrodynamics in the dissolution vessels and developing buffer media whose pH, buffer capacity, ionic strength, and bile acid composition mimic those of the *in vivo* gastric and intestinal fluids.[37–39] However, the USP apparati are still closed with respect to the released drug, and any effects of drug absorption, which will tend to lower drug concentration in the intestinal fluid and possibly reduce the rate of precipitation, are suppressed.[40] In this sense, the standard dissolution test may be more stringent than necessary, *underestimating* efficacy, especially for BCS-II drugs which, by definition, have good intestinal permeability properties. The USP Apparatus 4 or the flow-through cell when optimized can mimic *in vivo* rates of drug removal from the

intestinal lumen.[41] The USP Apparatus 4 establishes sink conditions by maintaining a continuous flow of drug-free dissolution medium to replace the drug-laden medium when operated in an open-loop mode. However, the volumes employed are usually unphysiologically large.[42] Moreover, manual sampling (e.g. using microfilters) and analytical techniques (e.g. UV spectroscopy, HPLC) used with all the above compendial tests usually do not distinguish between free drug and nano-sized drug aggregates or drug that is complexed to the excipient polymers.[43] While free drug is available for intestinal absorption, nano-aggregated or complexed drug probably is not.[14] The analytical technique may significantly *overestimate* the ability of an SSDF to provide drug in a supersaturated, highly bioavailable form.

1.2 Simultaneous Dissolution and Absorption Testing

1.2.1 State-of-art technology

To perform simultaneous dissolution-absorption measurements, a two-compartment system separated by a membrane barrier can be used wherein drug present in the donor compartment diffuses across the membrane into a receiver compartment. Several studies have been performed to develop an *in vitro* methodology using dissolution-absorption systems and to correlate the results with *in vivo* performance. Ginski and Polli were among the first to develop a dissolution/Caco-2 system to evaluate fast and slow dissolving immediate release formulations and correlated the performance with the clinical data.[44] Since then several modifications have been made to the membrane, fluid composition and configuration of the apparatus. Kataoka et al. carried out simultaneous dissolution and absorption studies of solid oral dosage forms in a side-by-side diffusion cell with a Caco-

2 monolayer mounted in between, to predict oral absorption.[45–48] They identified the rate-limiting step in oral absorption and distinguished formulations based on whether the absorption was dissolution rate-, solubility- or membrane permeability-limited. Motz et al. demonstrated use of a flow-through diffusion cell to study permeation of drug dissolved from tablets across a Caco-2 monolayer.[49] However, these cell based assays often suffer from high inter- and intra-lab variability, time consuming and expensive preparation steps, relative incompatibility with certain pharmaceutical excipients, and lower absorption surface area compared with the intestinal membrane.[50,51] Moreover, considering that 80-95% of commercial compounds are absorbed primarily by passive diffusion, there is a great interest in rapid and inexpensive simultaneous dissolution-permeation assays.[52]

Some absorption studies have been performed using artificial membranes as well. The most standard membrane-based assay is the parallel artificial membrane permeability assay (PAMPA) wherein the setup consists of 96-well microtiter plate containing hydrophobic filters that are saturated with lecithin – organic solvent mixtures.[53,54] A double artificial membrane permeability assay (DAMPA) was also developed to incorporate an intracellular aqueous compartment between two hydrophobic artificial membranes separating the donor and receiver compartments. A number of studies have demonstrated the use of artificial membranes to study membrane flux and to evaluate formulation performance of poorly soluble drug compounds.[23,55–57] The major limitation of these systems is, however, the small surface area for absorption relative to the volume for dissolution (~0.2 cm^{-1}), resulting in lengthy, non-physiological experimental time scales (e.g. 16 hours with a side-by-side diffusion cell compared to 2-4 hours of gut transit time).[58,59]

The challenge of a small surface area for absorption may be overcome by use of hollow fibers in the absorption module instead of flat-sheet membranes used in the earlier simultaneous dissolution and absorption testing systems. The ends of multiple hollow fibers are bundled into input and output ports. The hollow fibers are suspended in the drug dissolution/donor media. Either a syringe or a peristaltic pump drives the receiver fluid through the fiber lumen via the inlet port and out the outlet port. Drug diffusion occurs across the hollow fiber membrane along the concentration gradient from the donor to the receiver. The drug containing receiver media is continuously replaced by drug-free media, thereby maintaining an absorptive sink.

Commercial hollow fibers of varying pore sizes are available (10 nm to 200 nm). For the application of simulating *in vivo* drug absorption, hollow fibers with low pore size may be employed to ensure diffusion of only free drug species. A hollow fiber membrane module was first used to simulate intestinal absorption in a multicompartmental, dynamic, computer-controlled model of human upper gastrointestinal tract (TIM-1).[60] Hydrodynamics in this apparatus were controlled by altering the water pressure on the flexible membranes containing luminal contents.[60] However, most of the studies using TIM-1 have been reported for digestion and bioaccessibility of nutritional compounds, with only limited data available for evaluating pharmaceutical product performance.[61] Blanquet et al. studied the impact of transit time and food on oral drug absorption and the results were consistent with the *in vivo* data.[62] However, the complexity of the apparatus and lengthy experimental setup time are important limitations of using this system for evaluating drug performance.[61] Recently, a simple system with commercial hollow fiber module was introduced to facilitate rapid mass transfer across the membrane.[63] The authors

demonstrated the importance of fast absorption occurring simultaneously as dissolution of amorphous solid dispersion and mesoporous silica-based drug delivery systems in reducing the crystallization tendency in a seeded environment and ensuring more complete drug release, respectively.[64,65] However, close packing of hollow fibers in a commercial module may cause shell-side boundary layer interferences, especially at low fluid flow rate, resulting in inconsistent mass transfer rates over time.[66] Moreover, the authors did not optimize the operating parameters of the absorption module for absorption to take place at a physiological rate.

1.2.2 Artificial Gut Simulator

In this study, an artificial gut simulator (AGS) was developed consisting of a hollow-fiber based absorption module suspended in a 3 mL UV-Vis spectrophotometer cuvette that serves as a drug donor. Receiver media is pumped continuously, first through the intraluminal space of the hollow fibers to maintain an absorptive sink and next, to a UV-Vis spectrophotometer flow-through cell. The drug donor, absorption module and the flow-through cell are all placed in a UV-Vis spectrophotometer where continuous measurements of drug concentration in the donor and receiver media are made. The advantages of this supersaturation-absorption testing system are as follows:

- Large absorption surface area-to-donor volume ratio (> 2 cm^{-1}) allows attainment of physiologically relevant absorption rate constant within reasonable experimental time.
- A low molecular weight cut-off of hollow fibers excludes most non-bioavailable drug aggregates and complexes.
- Low volume for testing (3 ml or less) is important for early-stage drug development tests conducted in a material sparing manner.

- In-line, continuous measurement of drug concentration profiles in both donor and receiver media reduces sampling errors.
- The operating parameters are directly controlled by the designer/operator of the absorption module and can be easily varied to attain physiological absorption rate constant for a particular drug.
- The simple construction and easy operation lends potential to the AGS to screen formulations in a high-throughput manner.

The overall goal of this dissertation is to design and validate the AGS and demonstrate its utility in decoupling the GI exchange processes occurring simultaneously upon ASD dissolution (***Figure 1.2***) and ultimately in predicting *in vivo* intestinal and plasma concentration-time profiles of BCS-II drug formulations.

1.3 Chapter Descriptions

1.3.1 Chapter 2. Introduction and Validation of the Artificial Gut Simulator using Caffeine

Hypothesis 1. The theory of mass transport developed to describe drug diffusion from the AGS donor to receiver media across the hollow fiber membrane can be used to tune the AGS operating parameters to obtain an in vitro absorption rate constant that matches the in vivo absorption rate constant of a drug.

Summary: The purpose of this study was to develop and validate a simultaneous dissolution and absorption testing tool, the 'artificial gut simulator (AGS)', for oral drug formulations. The AGS was constructed using hollow fibers and housed in a 3 mL UV spectrophotometric cuvette that provided a large surface area-to-volume ratio to simulate absorption at a physiological rate. A steady-state model describing absorption was

developed and validated using a high aqueous solubility, BCS-I model compound, caffeine. This model was used to optimize the AGS operating parameters to simulate physiological gastric emptying and caffeine absorption that was further input into a one compartment pharmacokinetic (PK) model. The *in vivo* caffeine plasma concentration-time profiles matched those predicted by the PK model with *in vitro* input from the AGS. Ultimately, this work provides a framework for establishing *in vitro/in vivo* correlation with especially high permeability, BCS-II supersaturating drug formulations which will be explored in the future studies.

1.3.2 Chapter 3. Simultaneous Evaluation of Desupersaturation and Absorption from Ketoconazole Supersaturated Solutions using the Artificial Gut Simulator

Hypothesis 2. Degree of crystallization from metastable supersaturated solutions of a BCS-II model compound, ketoconazole, will be lower in the AGS donor relative to a closed, non-sink 'control' as absorption depletes drug from the AGS donor, thereby reducing the driving force for crystallization.

Summary: For supersaturating formulations of BCS-II compounds, which by definition have high intestinal permeability, a closed USP apparatus does not provide the necessary absorptive conditions during dissolution. To address this, an artificial gut simulator (AGS) has been constructed consisting of a 2.5 mL donor compartment in which a hollow fiber-based absorption module is suspended. Drug from donor diffuses across the hollow fiber membrane to be absorbed by the continually flowing intraluminal receiver fluid. The membrane surface area and intraluminal fluid flow rate are tuned to obtain the physiologically observed absorption rate constant for a weakly basic, poorly water-soluble model compound, ketoconazole (KTZ). Supersaturated solutions of KTZ were generated

in the donor in pH 6.5 phosphate buffer by pH-shift method in the absence (closed system, control) and presence (open system, test) of an optimally or suboptimally tuned absorption module. Drug concentrations in the donor and intraluminal fluids were determined by in-line UV spectroscopy. The presence of an absorptive sink reduced the supersaturated solution's crystallization propensity, more so in the case of the optimally tuned AGS. This study demonstrates the significance of simulating absorption of drug at a physiological rate during dissolution studies, especially to predict the performance of formulations of BCS-II drugs.

1.3.3. Chapter 4: Understanding the Impact of Absorption on In Vitro Dissolution, Speciation and Precipitation of Amorphous Solid Dispersions

Hypothesis 3. Drug absorption from the AGS donor can (i) enhance dissolution of amorphous solid dispersions as drug depletion from the donor can drive release of more drug from the formulation and, (ii) decrease the driving force for drug precipitation by decreasing the degree of supersaturation in drug donor. Also, drug bound to precipitate and colloidal polymer species can reduce the absorptive flux across the hollow fiber membrane due to a reduction in the drug's thermodynamic activity in solution.

Summary: Upon dissolution, amorphous solid dispersions (ASDs) of poorly water-soluble compounds can generate supersaturated solutions consisting of bound as well as 'free' drug species that are in dynamic equilibrium with each other. It is only the 'free' drug that is available for absorption. Drug bound to bile micelles, polymer excipient, amorphous and crystalline precipitate can reduce the drug solute's thermodynamic activity to permeate; but they can also serve as reservoirs to replenish the free drug in solution lost to absorption. However, with multiple processes of dissolution, absorption and speciation occurring

simultaneously, it may become quite challenging to understand which of the processes is leading to an increase or decrease in drug solution concentration. A closed, non-sink dissolution testing method used routinely, in the absence of drug removal, allows only for static equilibrium to exist and obscures the impact of each drug species on absorption. An artificial gut simulator (AGS) introduced recently consists of a hollow fiber-based absorption module and allows mass transfer of drug from the dissolution media at a physiological rate after tuning the operating parameters. ASDs of varying drug loadings were prepared with BCS-II model compound, ketoconazole (KTZ) and hypromellose acetate succinate (HPMCAS) polymer. Simultaneous dissolution and absorption testing of the ASDs was conducted with the AGS and simple analytical techniques were utilized to elucidate the impact of bound drug species on absorption. In all cases, lower amount of crystalline precipitate was formed in the presence of absorption relative to the non-sink dissolution 'control'. However, formation of HPMCAS-bound drug species and crystalline precipitate significantly reduced KTZ absorption. Moreover, at high drug loading, inclusion of an absorption module was shown to enhance ASD dissolution. The rank ordering of the ASDs was significantly different when non-sink dissolution versus AGS was used and this discrepancy could be mechanistically elucidated by understanding drug dissolution and speciation in the presence of absorption.

1.3.4. Chapter 5: A Scheme to Establish In Vitro/In Vivo Correlation with a Weakly Basic BCS-II Drug, Dipyridamole

Hypothesis 4. Simulation of gastric emptying and absorption are key to predicting the dissolved and precipitated concentration of BCS-II drugs in vivo in the intestinal lumen since the former process will generate supersaturated solution in a controlled manner

while the latter will reduce the degree of supersaturation. Both these processes are essential for controlling the rate of precipitation. By accurately predicting in vivo precipitation using the AGS, correct predictions of systemic drug exposure can be made, thereby establishing in vitro/in vivo correlation.

Summary: The objective of this study was to develop a scheme to establish IVIVC with weakly basic BCS-II drug, dipyridamole (DPD) using the artificial gut simulator (AGS) integrated with a compartment-based disposition model. The *in vivo* data for this study was obtained from previously published literature. A 3-compartment disposition model was developed using the plasma concentration-time profile of DPD following an intravenous bolus dose. The AGS consisting of a donor cell and a hollow fiber-based absorption module was tuned to absorb DPD saturated solution at a physiological rate constant, 0.0402 min^{-1}, based on the measured Caco-2 cell monolayer permeability coefficient. The dose dumping technique commonly used during dissolution testing can generate excessively high initial supersaturation and precipitation which is not physiologically relevant. In this study, fractions of DPD dose were added every 15 min to the AGS donor to simulate first-order gastric emptying. The concentration absorbed by the hollow fiber receiver media was scaled up and input into the central compartment of the disposition model. The predicted plasma concentration-time profile matched the human *in vivo* profile of DPD obtained after oral administration of a 50 mg dose. For 30 and 90 mg oral doses, time profiles of concentration and fraction precipitated in the AGS donor agreed well with human duodenal measurements. This study introduces a method to develop IVIVC with a BCS-II drug and demonstrates the importance of simulating drug absorption in IVIVC establishment.

Chapter 2: Introduction and Validation of the Artificial Gut Simulator using Caffeine

2.1 Graphical Synopsis

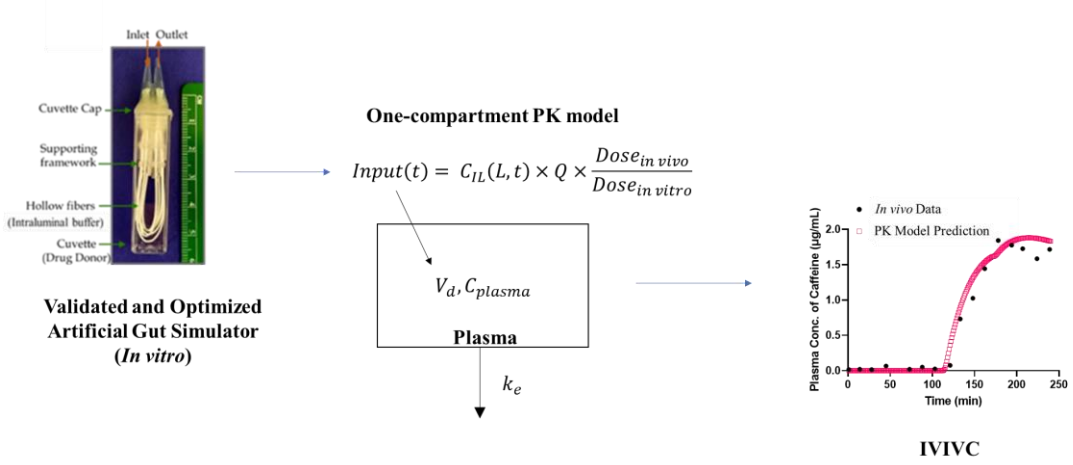

Figure 2.1. A scheme to establish *in vitro/in vivo* correlation using input from a validated and optimized *artificial gut simulator* in a 1-compartment disposition model for a high aqueous solubility, BCS-I model compound, caffeine.

2.2 Introduction

Drug dissolution testing is a mainstay in evaluating drug formulations for drug release and solution-state stability afforded by various excipients during product development, both for quality control and as a prognostic tool for drug absorption.[67–69] USP I and II dissolution testing apparati are closed vessels with dissolution media volumes up to 900 mL. Significant efforts have been made towards developing buffer media whose pH, buffer capacity, ionic strength and bile acid composition mimic those of *in vivo* gastric and intestinal fluids assuming that, especially for Biopharmaceutical Classification System (BCS)-II compounds, absorption is only solubility or dissolution rate limited.[38,39] If that is the case, one might be able to establish *in vitro/in vivo* correlation (IVIVC) to discriminate between formulations with different bioavailabilities.[70,71]

However, BCS-II compounds are often formulated as supersaturating solid forms (SSFs) such as high energy polymorphs, cocrystals, salts, and amorphous solid dispersions.[18,72–74] These forms dissolve to generate solutions that are supersaturated, albeit metastable to rapid desupersaturation or crystallization into a stable form. Only drug in solution is available for absorption whereas drug in the crystalline and/or amorphous phase is not. In this case, absorption may be reduced due to crystallization.[24,75] The rate of desupersaturation depends upon the concentration of drug in the media. A higher degree of crystallization has been observed in *in vitro* closed dissolution vessels compared to that observed in the intestinal lumen.[76,77] This observation may be attributed to decreasing drug concentration due to absorption from the lumen, which in turn decreases the driving force for crystallization. Clearly, USP I and II closed dissolution testing apparati do not accurately predict the fate of drug upon dissolution and often underestimate the efficacy of SSFs.[76,77]

Several membrane-based assay systems such as Parallel Artificial Membrane Permeability Assays (PAMPAs), side-by-side, or MicroFLUX™ (μFLUX) and MacroFLUX™ diffusion cells have been developed in recent years to simulate drug absorption.[54,55,78,79] However, their small membrane surface areas prevent their utilization in simulating drug absorption at physiological rates.[58,59] Recently, a hollow fiber-based simultaneous drug dissolution and absorption testing tool was introduced to facilitate rapid mass transfer across the membrane owing to its large surface area for absorption.[80] However, close packing of hollow fibers in a commercial module may cause shell side boundary layer interferences, especially at low fluid flow rate, resulting in inconsistent mass transfer rates over time.[66]

In this study we introduce a hollow fiber based simultaneous drug dissolution and absorption testing tool called the 'Artificial Gut Simulator' (AGS). Hydrophilic, poly(ether sulfone) (PES) hollow fibers are cut from a commercial module and arranged on a well spaced supporting framework to prevent shell side boundary layer interference. This hollow fiber-based absorption module is engineered to fit into a UV spectrometer cuvette to enable continuous in-line measurements of the drug dissolution media while minimizing sampling errors. The small volume of the cuvette enables testing in a sample sparing manner. As will be shown, this tool can be configured to "match" the physiological absorption rate constant (k_a) of a drug, and hence provide a more realistic emulation of the drug's "phase behavior" during dissolution and absorption.

In the following sections, we first describe the AGS design and operation, followed by the theory behind its operation. We then validate the theory and demonstrate its scope using caffeine as a high aqueous solubility, BCS-I model compound. (Although the AGS is expected to be most beneficial for low solubility BCS-II drugs, it is easier to work with a high solubility drug to validate the theory of operation). As an application, the AGS is optimized to simulate physiological gastric emptying dynamics and caffeine absorption. The *in vitro* absorption data from the AGS is then input into a one-compartment pharmacokinetic (PK) model to predict *in vivo* plasma concentration-time profiles obtained from a previously published study [81] describing oral caffeine absorption as a function of gastric emptying, to establish Level A IVIVC.[82] Finally, a framework for establishing IVIVC is presented for future studies that will explore the use of the AGS with low solubility, BCS-II compounds.

2.3 Artificial Gut Simulator Design and Operation

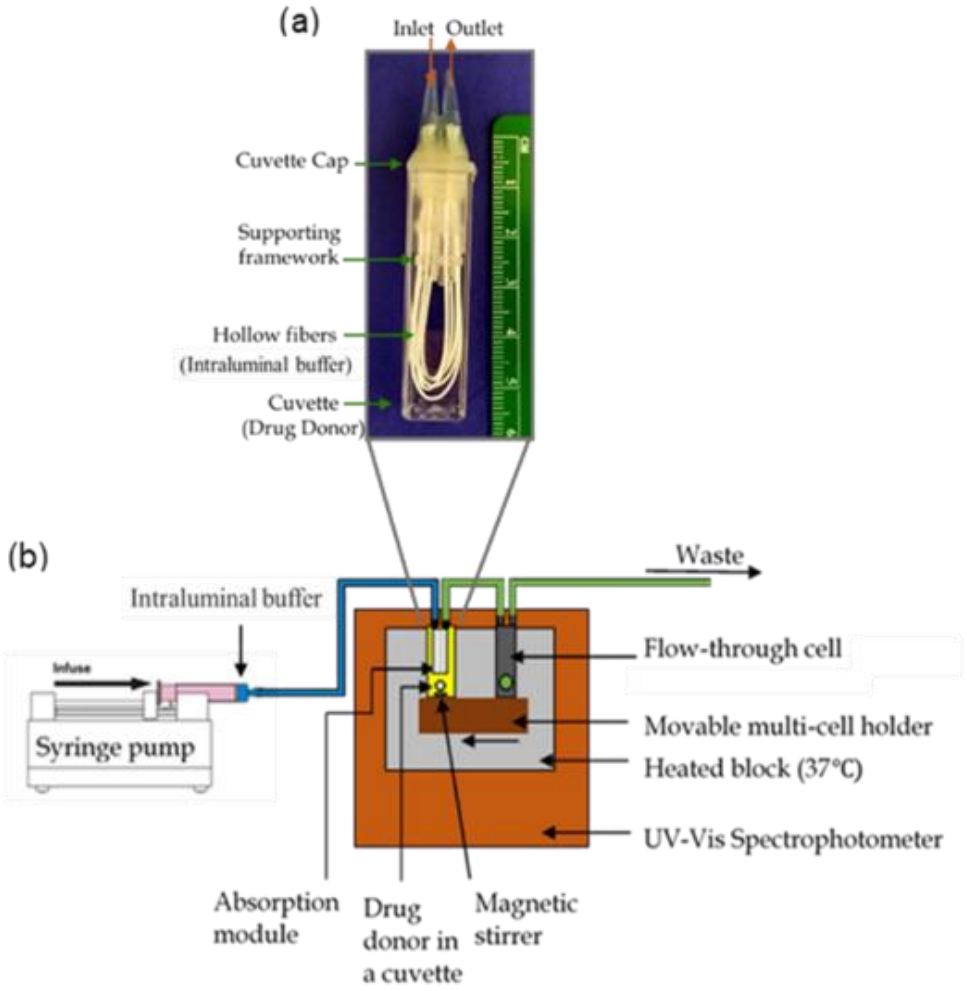

Figure 2.2. (a) AGS consisting of a hollow fiber-based absorption module suspended in drug donor solution in a UV-Vis spectrophotometer sample cuvette (Scale bar: 1 division = 1 mm). **(b)** Schematic representation of complete AGS set-up.

The AGS (***Figure 2.2*****)** consists of a) a cuvette that serves as a donor of drug dissolved/suspended in an aqueous medium and, b) an absorption module consisting of hollow fibers suspended from the lid of the cuvette, providing an absorptive sink (***Figure 2.2a***). The large surface area of the hollow fibers enables attainment of physiologically relevant rates of mass transfer. Hollow fibers are arranged on a plexiglass supporting framework and their ends are bundled into inlet and outlet ports for flow of intraluminal buffer. Concentrations of drug in the donor/extraluminal and receiver/intraluminal media are determined using a UV-Vis spectrophotometer equipped with a temperature controlled and magnetically stirred automatic multi-cell changer (***Figure 2.2b***). Constant stirring ensures homogenous distribution of drug throughout the extraluminal medium. Buffer (intraluminal medium) is pumped continuously through the hollow fiber manifold using a syringe pump. As drug diffuses across the hollow fiber membrane from the extra- into the intraluminal medium, the intraluminal absorbate is continuously replaced by drug-free buffer, thereby maintaining an absorptive sink.

A spectrophotometric assay of extraluminal medium in the cuvette is conducted every minute. Next, the concentration of drug in the intraluminal medium is determined when it is pumped to a flow-through cell placed in the cell slot adjacent to the donor cuvette. By this means, alternating absorbance measurements of extra- and intraluminal media are made continuously over the duration of the study.

As will be discussed in the following sections, the operating parameters of the AGS are directly controlled by the designer/operator.

2.4 Theory

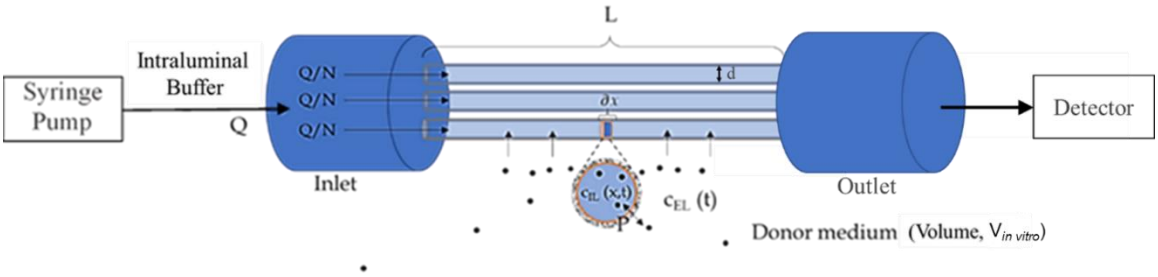

Figure 2.3. Schematic representation of AGS in operation.

Figure 2.3 is a schematic representation of the AGS, which consists of a well-stirred donor vessel (in practice a cuvette) containing drug solution of volume *V*. A manifold of *N* hollow fibers, each of length *L*, intraluminal diameter *d*, and membrane permeability *P* to the drug, is introduced into the vessel as the absorption module. The manifold's inlet is connected to a syringe pump, which delivers drug-free intraluminal buffer at a constant total flow rate, *Q*, and its outlet is connected to tubing leading to a detector, where the exiting drug concentration, C_{IL}, is assayed. Flow through a single fiber is given by *Q*/*N*, and the average fluid velocity in the fiber is $v = (Q/N)/(\pi d^2/4)$. The uniform extraluminal drug concentration in the vessel, C_{EL}, is also available for assay.

As buffer is pumped through the manifold, free drug diffuses across the hollow fiber membranes into the hollow fiber lumens and is carried out of the vessel by convection. Assuming rapid radial mixing in the lumen, $d^2/D << L/v$, where D is the diffusion coefficient of drug in the luminal fluid, and also assuming that concentration gradients develop rapidly in the hollow fiber membrane, we write the following mass balance,

$$\pi(d/2)^2 \frac{\partial C_{IL}}{\partial t} = -(Q/N)\frac{\partial C_{IL}}{\partial x} + (\pi d)P(C_{EL} - C_{IL}) \qquad 0 < x < L \tag{2.1}$$

where $C_{IL} = C_{IL}(x,t)$ is the local intraluminal concentration and $C_{EL} = C_{EL}(t)$ is postulated to be uniform due to the well-stirred condition. Making substitutions and rearranging,

$$\frac{\partial C_{IL}}{\partial t} = -v\frac{\partial C_{IL}}{\partial x} + \frac{4P}{d}(C_{EL} - C_{IL}) \qquad 0 < x < L \tag{2.2}$$

We ignore axial diffusion in this development. This assumption is justified by the long length of the hollow fiber relative to the short distance that a drug molecule can diffuse axially during its residence time in the lumen. If we may assume that $C_{EL}(t)$ changes slowly with time compared to $C_{IL}(x,t)$, then we can invoke the quasi-steady state assumption, wherein $\partial C_{IL}/\partial t$ is set to zero, and Eq. (2.2) is rewritten as

$$\frac{\partial C_{IL_{qss}}}{\partial x} + \frac{4P}{dv} C_{IL_{qss}} = \frac{4P}{dv} C_{EL} \qquad 0 < x < L \tag{2.3}$$

At any time, the entry point of the hollow fiber is drug free, i.e. $C_{IL}(0,t) = 0$ and $C_{IL_{qss}}(0,t) = 0$. Combining the latter boundary condition with Eq. (2.3), we obtain

$$C_{IL_{qss}}(x,t) = C_{EL}(t)\left[1 - exp\left(-\frac{4Px}{vd}\right)\right] \qquad 0 \le x \le L \tag{2.4}$$

In particular,

$$C_{IL_{qss}}(L,t) = C_{EL}(t)\left[1 - exp\left(-\frac{4PL}{vd}\right)\right] \quad (2.5)$$

Substituting for *v* and considering the intraluminal surface area of each hollow fiber, $A_{IL} = \pi dL$, the latter equation takes the form

$$C_{IL_{qss}}(L,t) = C_{EL}(t)\left[1 - exp\left(-\frac{NPA_{IL}}{Q}\right)\right] \quad (2.6)$$

At quasi-steady state the rate of drug removal from the AGS is $QC_{IL_{qss}}(L,t)$, hence the absorption clearance is

$$CL_{abs} = \frac{QC_{IL_{qss}}(L,t)}{C_{EL}} = Q\left[1 - exp\left(-\frac{NPA_{IL}}{Q}\right)\right] \quad (2.7)$$

When drug is introduced into the donor (extraluminal) medium at time $t = 0$ at concentration $C_{\mathrm{EL}}(0)$ at or below saturation, its concentration $C_{\mathrm{EL}}(t)$ will decay according to

$$C_{\mathrm{EL}}(t) = C_{\mathrm{EL}}(0)e^{-k_{\mathrm{a,AGS}}t} \quad (2.8)$$

where

$$k_{\mathrm{a,AGS}} = \frac{CL_{\mathrm{abs}}}{V} = \left(\frac{Q}{V}\right)\left[1 - exp\left(-\frac{NPA_{IL}}{Q}\right)\right] \quad (2.9)$$

is the apparent "absorption rate constant" of the AGS, which can be matched to the target physiologic value (k_a) by varying the parameters in the RHS of Eq. (2.9).

Of particular interest in this design is that one can work with small vessel volumes. Reduction of donor volume can be compensated by reducing absorption clearance to obtain the target k_a. As long as the *in vivo* and *in vitro* dose-to-volume ratios are matched, one need not work with USP sized dissolution vessels or even intestinal luminal volumes (as in the case of TIM gastrointestinal systems [83]). Thus studies can be carried out in a sample sparing manner.

It is useful to explore certain limits. In the flow-limited case, where $Q << NPA_{IL}$, $k_{a,AGS}$ approaches Q/V, whereas in the opposite, permeation-limited case where $Q >> NPA_{IL}$, Taylor expansion of Eq. (2.9) yields $k_{a,AGS} \rightarrow NPA_{IL}/V$. Consideration of these limits enables the operator to select, for example, the number of hollow fibers (*N*) and the flow rate *(Q)* once the other parameters are determined.

2.5 Materials and Methods

2.5.1 Materials

Caffeine was purchased from Fisher Scientific International, Inc. (Fair Lawn, NJ) and was used as received. 50 mM sodium phosphate buffer, pH 6.5, was used as the aqueous medium in the extra- and intraluminal media.

To construct the absorption module, 1.5 mm thick plexiglass was laser cut and welded into a hollow fiber supporting framework. PES hollow fibers of 5 kDa MWCO (molecular weight cutoff), length *L*=5 cm and internal diameter *d*=1 mm, were cut from a filtration

module purchased from Spectrum Laboratories Inc. (C06-E005-10-N, Rancho Dominguez, CA). Cuvette caps were purchased from Azzota Scientific (Claymont, DE). UV-cure silicone glue, used as potting material to fix the hollow fibers in the inlet and outlet tubes emerging from the cuvette cap, was purchased from Henkel Corporation (Westlake, OH).

2.5.2 Caffeine Permeability Coefficient across PES Hollow Fiber Membrane

Mass transport of caffeine across PES hollow fiber membranes from solutions at different sub-solubility concentrations was evaluated using the AGS setup shown in ***Figure 2.2***. 50 mM pH 6.5 phosphate buffer was pumped at Q=160 µL/min into the intraluminal space of N=5 hollow fibers in the absorption module using a syringe pump. Caffeine solutions of concentrations 20, 30, 40, 50 and 60 µg/mL were prepared separately in 50 mM pH 6.5 phosphate buffer. In a given run, V=2.5 mL of a particular solution was introduced into the donor cuvette at 37℃, at time t=0. Drug concentration in the extraluminal fluid was continuously monitored by UV spectrophotometry (Cary 100 Bio, Agilent, CA) at 278 nm for 120 min. Runs for each concentration of caffeine were carried out in duplicate. The permeability coefficient, P, of caffeine cross the PES membrane was estimated by fitting the experimental donor concentration-time profiles to Eq. (2.8) and then using Eq. (2.9).

2.5.3 Theoretical Model Validation

Theoretical model predictions describing mass transport of solute across the hollow fiber membrane were validated against the experimental caffeine extra- and intraluminal concentration-time profiles obtained by varying the operating parameters of the AGS. The permeability coefficient estimate of caffeine obtained from the previous experiment was used to generate model predictions using Eqs. (2.6) and (2.9). A 40 µg/mL caffeine solution

was prepared in 50 mM pH 6.5 phosphate buffer and introduced into the cuvette as the donor drug solution. Volume of the donor drug solution was 2.5 mL. In the first test, drug-free pH 6.5 phosphate buffer was pumped into hollow fiber modules of three different total surface areas for absorption, 9.42, 6.28 and 3.14 cm^2 (corresponding to N = 6, 4, and 2 hollow fibers) while maintaining a constant pumping rate through each fiber. In the second test, intraluminal fluid was pumped at three different flow rates, 40, 80 and 160 µL/min through a hollow fiber module of surface area 9.42 cm^2 (N= 6). A summary of the experimental design is given in ***Table 2.1***. Absorbance measurements from the donor (extraluminal fluid) and the flow through (intraluminal fluid) cells were taken every minute at 278 nm. Measurements were conducted in duplicate.

Table 2.1. Experimental design to validate AGS theoretical model. The operating parameters, surface area of hollow fibers and intraluminal fluid flow rate through each hollow fiber, were varied one at a time.

Number of hollow fibers (N)	Surface area of hollow fibers (N x A_{IL}, cm^2)	Intraluminal fluid flow rate (Q, µL/min)	Intraluminal fluid flow rate through each hollow fiber (µL/min)
6	9.42	40	6.7
6	9.42	80	13.3
6	9.42	160	26.7
4	6.28	106	26.5
2	3.14	54	27.0

2.5.4 Simulating In Vivo Absorption of Caffeine using the AGS

As an application, the AGS was used to simulate a previously published case study[81], in which the time dependent oral absorption of caffeine in humans was correlated with gastric motor activity. In that *in vivo* study[81], 100 mg doses of caffeine in the form of enteric coated pellets were administered to subjects so that caffeine absorption occurred only in the intestine. Absorption of caffeine was a function of the measured gastric motor activity in each individual subject, which directly influenced gastric emptying of caffeine into the small intestine. Subjects 4, 5 and 6 (out of 12 total subjects) from the study were considered here to approximately represent the range of gastric emptying dynamics. *In vivo* data was extracted from figures using WebPlotDigitizer (https//apps.automeris.io/wpd/). Parameters from Ref. [[81]] are summarized in ***Table 2.2***.

The study revealed large inter-individual differences with complicated gastric motor activity-time profiles and time-dependent gastric emptying rate constant $k_{g,n}$ (t) ('n' indexing the phase of gastric motility) (***Table 2.2***). Gastric emptying occurred following an initial quiescent phase lasting 1-2 hours. This was followed by an active phase during which more than 50% of the dose administered was emptied in a first-order manner. More than 90% of the dose was emptied from the stomach in the next 2 hours with one or two more quiescent periods between the active phases. There were also inter-subject differences in caffeine absorption rate constant. Absorption rate constant (k_a) values varied from 0.029 – 0.089 min^{-1}. Assuming 100 mL intestinal volume, the *in vivo* dose-to-intestinal volume ratio ($D_{in\ vivo}$: $V_{in\ vivo}$) was 1 mg/mL.

The volume of extraluminal, pH 6.5 phosphate buffer used as donor fluid in the *in vitro* study with AGS was 2.95 mL. To match the $D_{in\ vivo}$: $V_{in\ vivo}$ of 1 mg/mL, a highly

concentrated stock solution containing 2.95 mg caffeine in 10 μL pH 1.5 HCl buffer was prepared. Fractions of this stock solution were spiked into the extraluminal buffer at times corresponding to the start of active phases of gastric motility, as summarized in ***Table 2.2***. (An enteric coated formulation was not used here as it was stipulated in the human *in vivo* study that the enteric coating and drug dissolution in the intestine was rapid[81].)

Table 2.2. Summary of caffeine *in vivo* parameters used as inputs in the PK model and *in vitro* dosing schedule to simulate gastric emptying with AGS for subjects 4, 5 and 6 in Ref. [81]. $k_{g,n}$ (t), gastric emptying rate constant during the n'th phase of gastric motility; k_a , absorption rate constant; k_e , elimination rate constant; V_d , volume of distribution; $D_{in\ vivo}$, *in vivo* dose administered; $V_{in\ vivo}$, *in vivo* intestinal volume; $D_{in\ vitro}$, *in vitro* Dose; $V_{in\ vitro}$, *in vitro* donor volume.

	Subject 4	Subject 5	Subject 6
	***In vivo* Parameters**		
$k_{g,n}$ (t)	Time (min) / k_g (min^{-1}): 0-41 / 0.0021; 42-56 / 0.0326; 57-65 / 0.0085; 66-75 / 0.0620; 76-121 / 0.0024; 122-146 / 0.0442; 147-192 / 0.0054; 193-216 / 0.0081; 217-240 / 0.0005	Time (min) / k_g (min^{-1}): 0-100 / 0; 101-109 / 0.1031; 110-114 / 0.0321; 115-123 / 0.2400; 124-213 / 0.0019; 214-235 / 0.0828; 236-240 / 0.0074	Time (min) / k_g (min^{-1}): 0-112 / 0.0021; 113-134 / 0.0326; 135-171 / 0.0085; 172-176 / 0.0620; 176-240 / 0.0024
k_a	0.0395 min^{-1}	0.0315 min^{-1}	0.0290 min^{-1}
k_e	0.00410 min^{-1}	0.00168 min^{-1}	0.00371 min^{-1}
V_d	39150 mL	39444 mL	40107 mL
$D_{in\ vivo}\ (100\ mg) : V_{in\ vivo}(100\ mL)$	1 mg/mL	1 mg/mL	1 mg/mL
	***In vitro* Parameters**		
$D_{in\ vitro} : V_{in\ vitro}$	1 mg/mL	1 mg/mL	1 mg/mL
$D_{in\ vitro}$ schedule	Time (min) / Dose added (mg): 41 / 1.27; 65 / 0.86; 120 / 0.62; 146 / 0.20; **Total** / **2.95**	Time (min) / Dose added (mg): 100 / 1.68; 110 / 1.12; 213 / 0.15; **Total** / **2.95**	Time (min) / Dose added (mg): 112 / 2.55; 171 / 0.40; **Total** / **2.95**
$V_{in\ vitro}$	2.95 mL	2.95 mL	2.95 mL

To account for the differing values of k_a observed across subjects, hollow fiber module parameters, specifically intraluminal fluid flow rate, *Q*, and number of hollow fibers, *N* (therefore, surface area of the follow fibers) were varied to obtain the desired $k_{a,AGS}$ [Eq. (2.9)] for each subject. Caffeine concentration in the intraluminal fluid was measured by UV spectroscopy every minute. The high caffeine concentration in the donor medium saturated the spectrophotometer and could not be measured.

To investigate IVIVC, a one-compartment PK model for drug in plasma was set up in SimBiology (MATLAB R2020b). The parameters, elimination rate constant, k_e and volume of distribution, V_d reported in the *in vivo* study [81] are summarized in ***Table 2.2*** for subjects 4, 5 and 6 and were used as inputs for the PK model. The *in vitro* drug concentration absorbed by the intraluminal fluid, $C_{IL}(L,t)$, was used to generate an input function $I(t)$ to describe the *in vivo* amount of drug absorbed with time [Eq. (2.10)].

$$I(t) = C_{IL}(L,t) \times Q \times time\ interval\ between\ measurements \times \frac{Dose_{in\ vivo}}{Dose_{in\ vitro}} \qquad (2.10)$$

Ultimately, $I(t)$ was input into the PK model to predict the *in vivo* plasma-concentration time profile of caffeine [Eq. (2.11)] and establish Level A IVIVC:

$$\frac{dC_{plasma}}{dt} = \frac{I(t)}{V_d} - k_e \times C_{plasma} \qquad (2.11)$$

where the values of V_d and k_e are subject dependent and listed in ***Table 2.2***.

2.6 Results

2.6.1 Caffeine Permeability Coefficient across PES Hollow Fiber Membranes

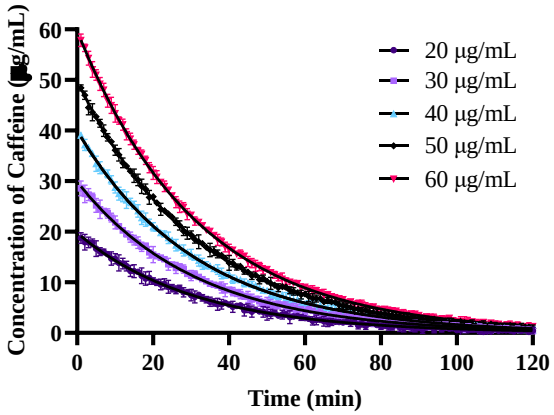

Figure 2.4. Donor drug concentration-time plots at five different starting concentrations of caffeine. Error bars represent standard deviations of duplicate measurements. The experimental data sets were fit to Eqs. (2.8) and (2.9) (black lines) to obtain average *P*.

The caffeine mass transfer study across the hollow fiber membrane was conducted using concentrations at sub-solubility levels in pH 6.5 phosphate buffer at 37 ℃. The AGS was operated at an intraluminal fluid flow rate of 160 µL/min, hollow fiber area for absorption of 7.85 cm^2 (N=5) and donor volume of 2.5 mL for all the runs. ***Figure 2.4*** shows the cumulative donor (extraluminal) concentration-time profiles of caffeine obtained from continuous UV spectrophotometric measurements. The donor drug concentration decreased in all cases due to absorption across the hollow fiber membrane into the intraluminal buffer. The decline in donor drug concentration due to absorption was exponential and after 120 minutes, about 95% of the drug was cleared from the donor solution. Membrane permeability, *P*, was estimated by fitting the respective donor

concentration-time series obtained to Eq. (2.8) and then using Eq. (2.9). From these curves P was estimated to be $(2.34 \pm 0.02) \times 10^{-4}$ cm/s.

2.6.2 Theoretical Model Validation

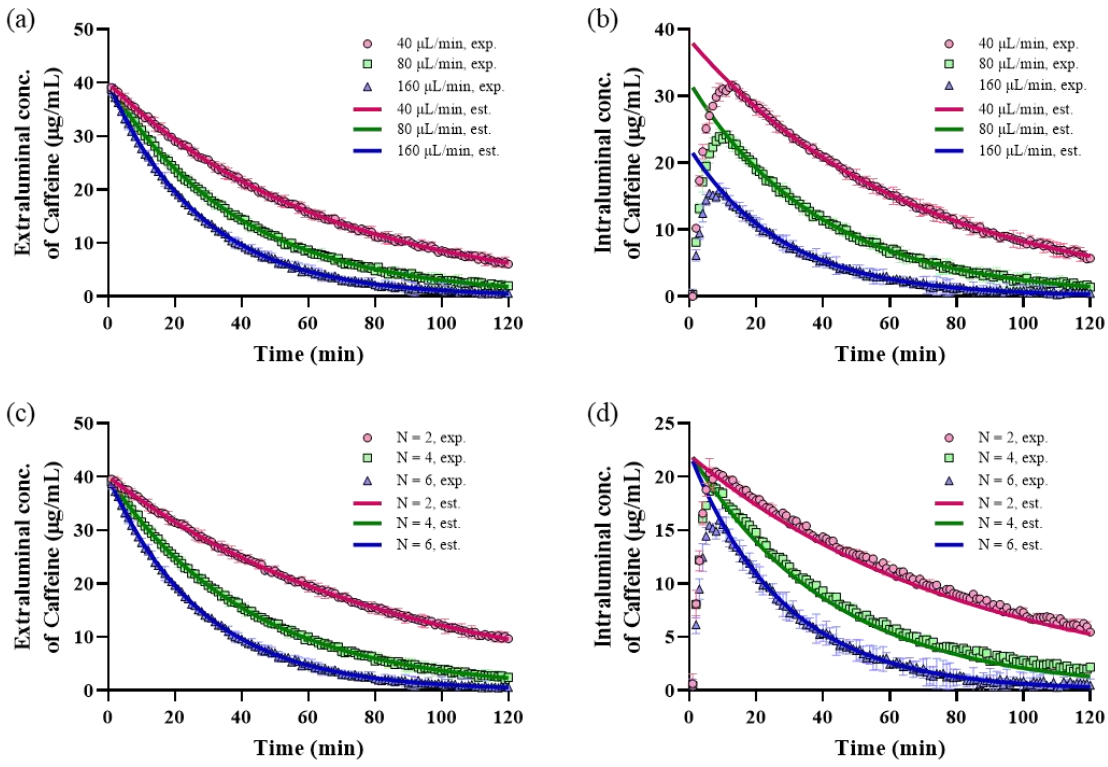

Figure 2.5. Predicted [Eqs. (2.8) and (2.6), respectively; lines] and experimental (symbols) concentrations of extraluminal and intraluminal caffeine. **(a)** Extraluminal and **(b)** intraluminal concentration-time plots obtained by varying intraluminal fluid flow rate, Q, through a hollow fiber module of surface area 9.42 cm^2 (N = 6). **(c)** Extraluminal and **(d)** intraluminal concentration-time plots obtained by varying N, the number of hollow fibers (in other words, total hollow fiber surface area), while maintaining a constant intraluminal fluid flow rate of approximately 27 μL/min through each hollow fiber. Error bars represent standard deviations of duplicate measurements.

Using the value of permeability, P, estimated in the previous section, the theoretical model developed was validated by monitoring caffeine mass transport across the hollow fiber membranes from an initial 40 μg/mL solution in the donor into the intraluminal buffer. As summarized in ***Table 2.1***, the AGS was operated at different flow rates and surface areas for absorption (i.e. numbers of hollow fibers). The resulting extra- and intraluminal concentration-time profiles predicted using Eqs. (2.8) and (2.6), respectively, are represented as solid lines corresponding to their respective experimental data sets (symbols), all plotted in ***Figure 2.5***. Under all conditions, donor caffeine concentration declines exponentially with time due to drug absorption (***Figure 2.5a,c***). The intraluminal drug concentration, on the other hand, initially increases from zero, but eventually tips over and decays exponentially (***Figure 2.5b,d***). This behavior can be attributed to a combination of delay in attaining quasi-steady state due to the residence time of buffer in the hollow fiber and an initial diffusional time lag across the hollow fiber membrane. Following attainment of quasi-steady state, drug concentration in the intraluminal fluid decreases as the driving force for permeation across the hollow fibers decreases with declining donor concentration. Experimental data of donor and intraluminal concentrations are in excellent agreement with predictions in all cases, except during the initial time points before attainment of quasi-steady state in the intraluminal fluid.

In ***Figure 2.5a,b*** **(constant *N* with varying *Q*)** it is shown that upon attainment of quasi-steady state, extra- and intraluminal drug concentrations decline more rapidly as the intraluminal fluid flow rate increases due to better sink conditions. At lower flow rates, the time lag to attain quasi-steady state is longer. Time lags can be expected to increase with decreasing fluid velocity within each hollow fiber due to the thickening of aqueous

boundary layers adjacent to the intraluminal membrane. [66] (This contradicts our assumption of rapid radial mixing in the hollow fiber.) While drug clearance from the donor increases considerably as we increase the intraluminal fluid flow rate from 40 to 80 µL/min, the increase in clearance is more modest upon further increase in flow rate, indicating that we are close to the permeation-limited absorption regime wherein $Q >> NPA_{\mathrm{IL}}$, and the magnitude of $k_{\mathrm{a,AGS}}$ is dependent only on $N, A_{\mathrm{IL}}, P\ and\ V$.

At constant intraluminal flow rate per hollow fiber (Q/N), as surface area for absorption increases with increasing number of hollow fibers in the absorption module, the rate of drug absorption from the donor also increases (***Figure 2.5c***). Since the intraluminal fluid flow rate through each hollow fiber is kept constant, the residence time in the hollow fiber lumen is the same irrespective of the number of fibers employed, which explains the observation of similar time-lags to attain quasi-steady state in all three cases (***Figure 2.5d***). After this, however, the rate of decline of intraluminal drug concentration is different, the rate being higher with larger surface area for absorption.

2.6.3 Simulating In Vivo Absorption of Caffeine using the AGS

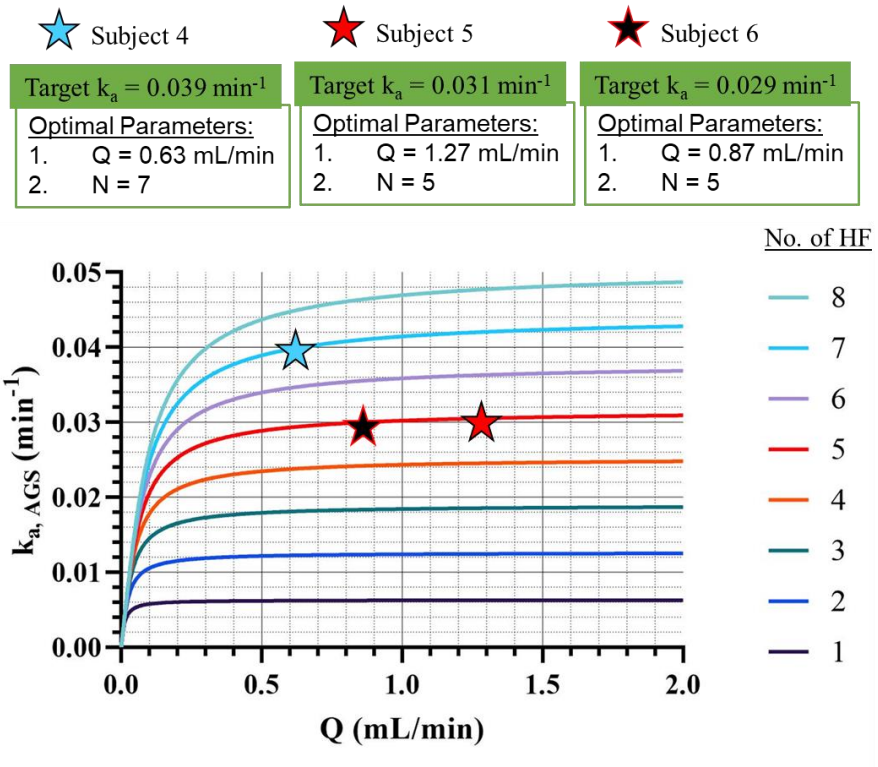

Figure 2.6. Family of plots of $k_{a,AGS}$ of caffeine as a function of hollow fiber surface area for absorption ($N * A_{IL}$, 1.35 – 10.80 cm^2) and receiver fluid flow rate (Q, 0 – 2 mL/min) obtained using Eq. (2.9). AGS operating parameters were optimized for each subject to obtain the respective target k_a. Volume of extraluminal fluid, V, was fixed at 2.95 mL. Hollow fiber (HF) membrane permeability, P, was fixed at 2.34 × 10^{-4} cm/sec.

To simulate each subject 4, 5 and 6 in the *in vivo* study[81], the AGS was tuned, using Eq. (2.9) and varying Q and N, to absorb caffeine according to that subject's physiologically observed rate constant, k_a (***Table 2.2***). ***Figure 2.6*** is a family of curves showing how $k_{a,AGS}$ increases with increasing Q and N, given the permeability of the HF membrane and the volume of the extraluminal fluid. Using these curves, one can select Q and N to produce the value of $k_{a,AGS}$ that matches the subject's k_a value.

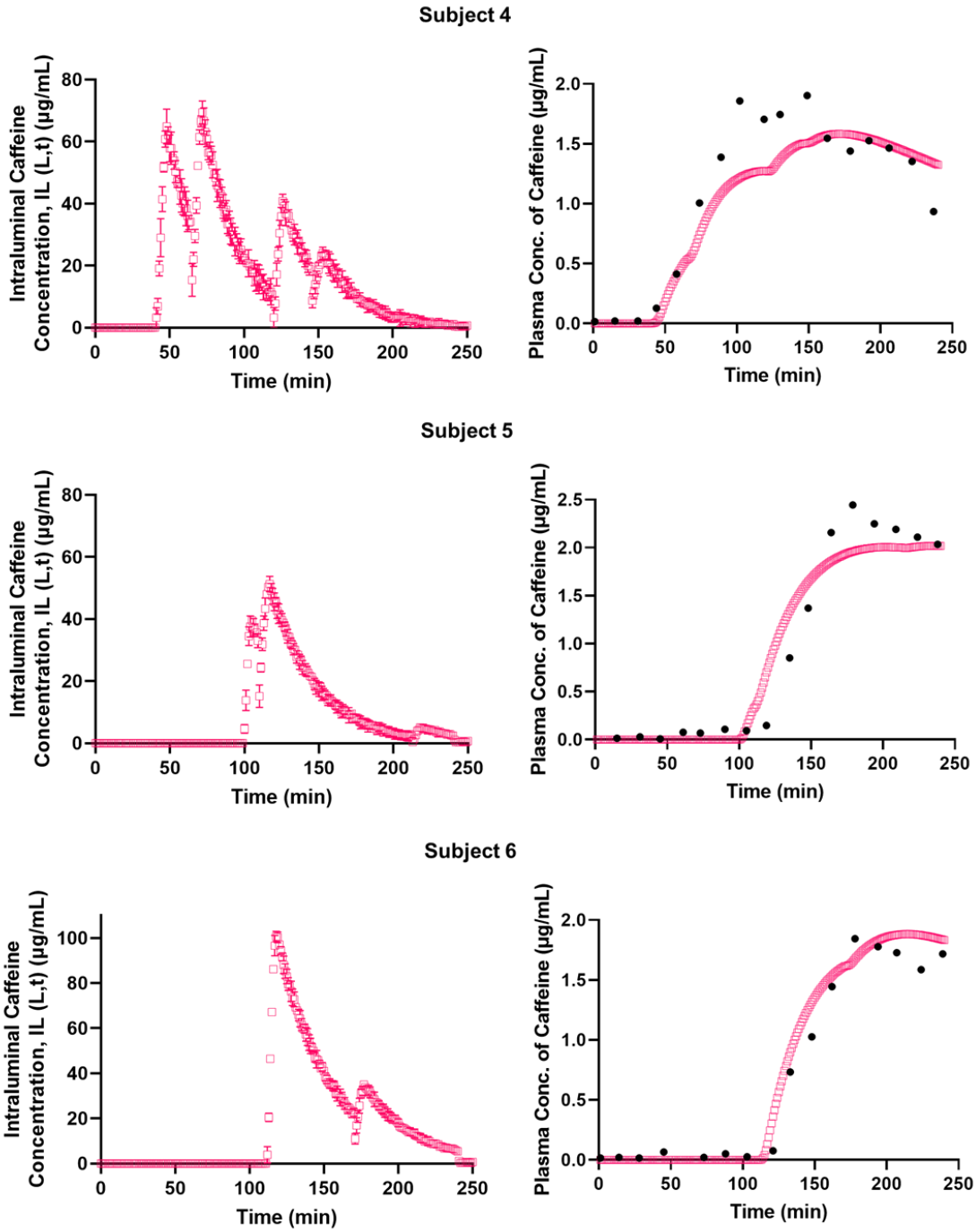

Figure 2.7. **(Left)** Intraluminal caffeine concentration-time profile as caffeine was absorbed from the donor medium. Peaks represent the points of addition of caffeine dose fraction to simulate gastric emptying (***Table 2.2)*** in subjects 4, 5 and 6. **(Right)** Overlaid *in vivo*[81] (filled black circles) and predicted (mean, open magenta squares) plasma concentration-time profiles predicted using the one-compartment PK model with AGS *in vitro* absorption data as input [Eqs. (2.10) and (2.11)].

Figure 2.7 (left) shows, for each of the simulated subjects, the intraluminal concentration-time profile as caffeine was absorbed from the donor medium, i.e. the cuvette. Varying fractions of the caffeine dose were added to the donor at varying times to correspond to the fraction of drug emptied *in vivo* from the stomach into the small intestine during the active phases of gastric motility in the three subjects (***Table 2.2***). Upon addition of caffeine, after a certain diffusional time lag, maximum drug concentration (C_{max}) and quasi-steady state were attained in the intraluminal media and this occurred each time a dose addition was made. With time, the concentration of drug decreased in the donor due to absorption and this is reflected in the declining drug concentration in the intraluminal fluid following each C_{max}. (The sudden decline in drug concentration at each point of addition of drug dose fraction is due to the removal of the AGS absorption module from the donor media resulting in absence of drug absorption, and dilution of intraluminal drug concentration, for about two minutes.)

The intraluminal concentrations were used to calculate $I(t)$ to be input into the one-compartment PK model, Eq. (2.10), and predict caffeine *in vivo* plasma concentration-time profiles for the three subjects, Eq. (2.11). From ***Figure 2.7 (right)***, it is apparent that predicted plasma concentration-time profiles match well with those observed *in vivo*.[81]

2.7 Discussion

Passive permeability across the intestinal epithelial bilayer membrane plays a crucial role in determining the bioavailability of orally administrated drugs. However, USP I and II dissolution testing apparati, most commonly used to evaluate drug product performance, lack an absorptive sink similar to that existing *in vivo*. In the absence of drug removal by absorption, the SSFs of BCS-II drugs, which by definition have good intestinal permeability, precipitate under the unphysiological non-sink conditions of these closed dissolution testing apparati.[76] High drug concentration above drug solubility serves as a driving force for precipitation and an unrealistic degree of supersaturation can ultimately lead to poor IVIVC. This is unlike the condition that exists in the small intestine where absorption decreases drug concentration in the intestinal lumen, which in turn decreases the driving force for crystallization.[77,84]

Le Chatelier's principle states that if a physicochemical system in dynamic equilibrium experiences a change in concentration of the reactants or products, the system will respond to oppose that change. This means that declining drug concentration in the intestinal lumen due to absorption will cause precipitate formed to redissolve to replenish the drug in solution lost to absorption.[25] By the same principle, even when drug dissolution from a formulation is the rate-limiting step in drug absorption, more drug can be expected to be released in a system with an absorptive sink in comparison to one without. Thus, an *in vitro* testing tool that can simulate the *in vivo* intestinal luminal conditions not just in terms of the luminal dissolution media but also absorption rate, is needed.

The AGS was engineered to provide a high surface area-to-dissolution volume using hollow fibers to simulate drug absorption at a physiological rate. Using a UV

spectrophotometer cuvette as a dissolution vessel allows in-line continuous measurements, preventing sampling errors. Moreover, the small volume of the cuvette enables testing to occur in a high throughput, sample sparing manner, which is convenient during early-stage drug development.

The present study presents and validates a theory of concentration gradient-driven mass transport of a drug solute from the dissolution media into the buffer in the lumen of the hollow fiber using a quasi-steady state model. The ultimate parameter of interest, $k_{a,AGS}$, can be 'dialed in' to match the target k_a and simulate drug absorption at a physiological rate by varying intraluminal fluid flow velocity, surface area of absorption, and dissolution volume. The parameter P was determined by fitting Eqs. (2.8) and then (2.9) to extraluminal concentration-time profiles obtained for various starting concentrations of caffeine (***Figure 2.4***). This allowed the estimation of $k_{a,AGS}$ of caffeine for a set of operating parameters of the AGS using Eq (2.9). Eqs. (2.8) and (2.6), respectively, predicted quasi-steady state exponential decline in drug concentration in the extra- and intraluminal media, thereby validating the model (***Figure 2.5***).

Typically, k_a is not known, especially for drugs in early stages of development. Mudie et al. have reviewed the importance of simulating k_a during *in vitro* dissolution and absorption testing and how it can be estimated for drugs for which k_a is unknown *a priori*.[36] Briefly, *in vivo* k_a is a function of the permeability coefficient of the drug across the intestinal epithelial membrane, P_{em}, and the geometric surface area of the intestine-to-luminal volume ratio, $\frac{SA}{V_{in\ vivo}}$.

$$k_a = P_{em} \times \frac{SA}{V_{in\ vivo}} \tag{2.12}$$

P_{em} can be estimated using models that use molecular descriptors as input parameters for passively absorbed drugs.[85] Alternatively, P_{em} can be estimated using Caco-2 cell monolayer or rat perfusion assays.[85] Mudie et al. divided the k_a values of passively absorbed drugs in humans by their respective P_{em} values estimated using molecular descriptors and estimated $\frac{SA}{V_{in\ vivo}}$ to be about 2 cm^{-1}.[36] Using this value for $\frac{SA}{V_{in\ vivo}}$ and estimates of P_{eff} obtained using *ex vivo* assays or molecular descriptors, k_a of a compound may be estimated. The AGS operating parameters can then be optimized using Eq. (2.9) to simulate drug absorption at the desired k_a.

As a case example drawn from Ref. [[81]], *in vivo* absorption of caffeine was simulated using the AGS optimized to absorb drug at three different absorption rates as determined for three different subjects. Typically, a single average absorption rate constant for a drug would be determined, which can be used to optimize the AGS. However, in this study, we sought to demonstrate the scope of the AGS in terms of its flexibility to modify the operating parameters to simulate the desired absorption rate constant. Hence, the AGS was optimized to simulate absorption at three different absorption rate constants (corresponding to three subjects) for the same drug, caffeine (***Figure 2.6***). The AGS donor medium simulates the intestinal luminal fluid in terms of its pH and drug concentration. Ideally, both the intestinal luminal and AGS donor volumes would be set to equal. However, as long as $D_{in\ vivo}$: $V_{in\ vivo}$ and $D_{in\ vitro}$: $V_{in\ vitro}$ are the same, that need not be the case. Since $V_{in\ vitro}$ of AGS was about 34 times lower than $V_{in\ vivo}$ (assumed to be 100 mL), $D_{in\ vitro}$ was also reduced by the same factor to ensure physiological relevance. Gastric emptying

was simulated by dosing the same fraction of drug as was emptied during the active phases of gastric mobility (***Table 2.2***). Concentration of drug absorbed was measured in the intraluminal fluid and was scaled up to generate an input function *I(t)* [Eq (2.10)]. Ultimately, *I(t)* was used to input the dose amount absorbed in the one-compartment caffeine disposition model [Eq (2.11)].

For BCS-I drugs, gastric emptying is an important rate-limiting step for absorption. Since gastric emptying may be discontinuous, it is not uncommon to observe multiple peaks in the plasma concentration-time course.[86] This was observed in subjects 4 and 6 and this discontinuous gastric emptying was similarly simulated *in vitro* using the AGS. In all the cases, the one-compartment PK model was able to predict the *in vivo* caffeine plasma concentration-time courses with good accuracy (***Figure 2.7***).[81]

In a more generalized case, it may be possible to simulate gastric emptying by introducing the drug pre-dissolved/suspended in simulated acidic gastric media into the simulated intestinal media (having the absorption module) at a first order rate constant (2.8 $hour^{-1}$) using a programmable syringe pump.[87] This is especially important for introducing SSFs of BCS-II compounds as the rate of gastric emptying, or in other words, the rate of drug introduction into the simulated intestinal media, influences the rate of supersaturation generation, which in turn influences the rate of drug crystallization.[88]

Below is a step-wise framework that be utilized for the establishment of IVIVC using the AGS.

1. Determine *P* of drug across the hollow fiber membrane.

2. Determine human k_a either directly from *in vivo* studies or indirectly using molecular descriptor model or *ex vivo* assays to determine P_{em} [Eq. (2.12)].
3. Use the theory developed in this study [Eq. (2.9)] to tune the AGS to simulate absorption at physiological k_a.
4. Determine $D_{in\ vivo}$:$V_{in\ vivo}$ and match it to $D_{in\ vitro}$:$V_{in\ vitro}$.
5. Conduct simultaneous dissolution/absorption testing by either introducing the drug as a single bolus or at a first-order rate to simulate gastric emptying.
6. Measure the intraluminal concentration-time profile and determine the cumulative fraction absorbed as a function of time.
7. Develop a PK model that can predict the *in vivo* plasma concentration-time profile of the drug. Then compare the PK model predictions of *in vivo* and *in vitro* percentage absorbed-time profiles obtained using the AGS to establish Level A IVIVC.
8. Alternatively, *in vitro* AGS intraluminal concentration absorbed-time profiles can be scaled-up [Eq. (2.10)] and input into the PK model to predict *in vivo* plasma concentration-time courses [Eq. (2.11)]. The predicted and actual *in vivo* plasma concentrations can then be compared to establish Level A IVIVC, as was done in this study.

2.8 Conclusion

This study introduces a novel, convenient and inexpensive *in vitro* dissolution and absorption testing tool. Compared to flat-sheet membranes used in diffusion cells, the surface area for absorption in the AGS was greatly increased by using hollow fibers. A theory of mass transport from the donor media into the continuously flowing hollow fiber luminal buffer was developed and validated using caffeine. The importance of simulating drug absorption at physiological k_a was highlighted and the AGS operating parameters were tuned to attain the same with caffeine. Caffeine plasma concentration-time courses predicted by the PK model using *in vitro* AGS absorption data as input were demonstrated to match *in vivo* profiles. The next step would be to understand how inclusion of such an absorption module may influence supersaturated formulation precipitation kinetics and whether there is an improvement in IVIVC in comparison to that obtained using a closed dissolution testing apparatus.

Chapter 3: Simultaneous Evaluation of Desupersaturation and Absorption from Ketoconazole Supersaturated Solutions using the Artificial Gut Simulator

3.1 Graphical Synopsis

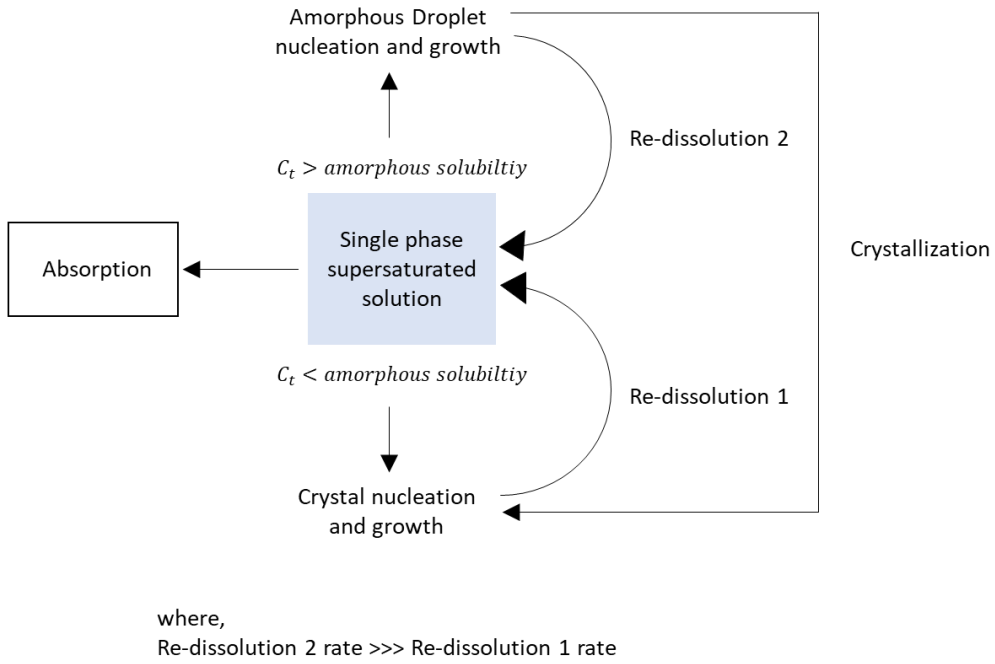

Figure 3.1 Schematic representation of simultaneous absorption, amorphous and crystalline precipitation from a single phase supersaturated solution of a BCS-II compound. Crystalline and amorphous phases can redissolve to replenish the free drug in solution lost to absorption, with the latter redissolving at a much faster rate due to higher free energy and larger surface area in contact with the aqueous media.

3.2 Introduction

Over the past three decades, high-throughput screening has resulted in a discovery pipeline consisting mostly of highly potent but lipophilic, relatively large molecular weight compounds exhibiting poor aqueous solubility and largely classified as Biopharmaceutics Classification System (BCS) Class II.[89,90] Since poor solubility limits absorption and bioavailability, there have been many efforts to enhance the apparent solubility of such molecules. Dosage forms that release drug in a super-soluble or supersaturated state, with

concentrations exceeding thermodynamic solubility, have received much attention. Supersaturating solid forms (SSFs) include high energy polymorphs, cocrystals, salts, and amorphous solid dispersions (ASDs).[18,73,74,91] When dissolved at supersaturating solution concentrations, higher thermodynamic activity of the drug solute (relative to that of a solute at equilibrium with the crystalline phase) translates to an increased driving force for transit from the intestinal lumen into and through enterocytes.[92–95] However, phenomena such as salt disproportionation or amorphous-to-crystalline and polymorphic phase transformation can also occur with SSFs during manufacturing, storage, or dissolution into the intestinal fluid, partially canceling the intended benefit.[71,96–99]

To mechanistically understand and discriminate between the performance of SSFs, *in vitro*, and ultimately predict their performance *in vivo*, there is a need to develop tools that closely simulate conditions existing in the gut. Traditionally, the most common tool has been the standard USP dissolution test, with periodic withdrawal and analysis of liquid aliquots. With respect to SSFs, drug precipitates are excluded during analysis, and a "spring-parachute" dissolution profile is often observed, with the "spring" corresponding to rapid dissolution of drug into the supersaturated state, followed by the "parachute," during which some of the drug crystallizes.[88,100]

A highly supersaturated drug solution can also undergo glass-liquid or liquid-liquid phase separation (LLPS), that is, amorphous precipitation prior to drug crystallization to form drug rich disordered colloidal aggregates.[101,102] Such behavior is observed when drug concentration exceeds its amorphous solubility in the aqueous medium. These aggregates, unlike the crystalline phase, are thought to be in dynamic equilibrium with drug in solution, rapidly re-dissolving to replenish drug in solution that is lost to absorption.[56] However, this

metastable supersaturated solution can eventually overcome the kinetic barrier to crystal nucleation, decreasing the drug solution concentration.

The standard USP dissolution test is neither optimal nor satisfactory in predicting the performance of SSFs. The system is 'closed' with respect to released drug, and any effects of drug absorption, which will tend to lower drug concentration in the intestinal fluid and subsequently reduce the driving force for crystallization, are suppressed.[76,84,103,104] In this sense, the standard dissolution test may be more stringent than necessary, *underestimating* efficacy, especially for BCS-II drugs which, by definition, have good intestinal permeability properties. Prediction of drug precipitation effects, amorphous and/or crystalline, on drug release and bioavailability can be made by combining *in vitro* data with computational modeling of drug absorption[103,104] or by using *in vitro* tools that allow continuous drug removal from the dissolution media at physiologically relevant absorption rates.[105] The latter would likely be more insightful into the solution phase behavior of the drug.

An inexpensive, rapid and material-sparing screening tool called the 'Artificial Gut Simulator (AGS),' which simulates drug absorption using a hollow fiber-based absorption module with a large surface area was developed in Chapter 2. The absorption module is suspended in a UV spectrophotometer cuvette containing the donor medium. Drug in the donor medium diffuses across the hollow fiber membrane into the intraluminal receiver fluid, which is replaced continuously by fresh buffer, thereby maintaining an absorptive sink. Operating parameters of the AGS such as the surface area of hollow fibers, intraluminal fluid flow rate and volume of donor medium, are directly controlled by the designer/operator. These parameters can be chosen to match the known *in vivo* absorption

rate constant of a drug under study when that drug is present at or below saturation. Under these conditions, drug concentration in the AGS is expected to decline exponentially, according to the "dialed in" rate constant. When drug is introduced into the AGS at supersaturated concentrations, processes such as crystallization and LLPS may be signaled by deviations from exponential decline in free drug concentration in the AGS.

In the present study, the AGS is tuned to simulate absorption of the model drug ketoconazole (KTZ). KTZ is a low solubility, high permeability BCS Class II drug. Upon oral administration as an SSF, ionization and aqueous solubility of weakly basic KTZ decreases as it is emptied from the acidic stomach into the relatively alkaline intestinal environment, resulting in a supersaturated solution.[77] KTZ is classified as a slow crystallizer, a highly supersaturated solution of which can experience LLPS.[106] The pH-shift method was therefore used here to generate supersaturated solutions of KTZ in the donor compartment of the AGS at concentrations above and below its amorphous solubility. Drug precipitation was studied as absorption occurred simultaneously. To demonstrate the need for simulating drug removal at its physiological rate, absorption of drug from supersaturated KTZ solution was conducted using optimized and sub-optimal AGS operating parameters. The key expectation was that the extent of crystallization from KTZ supersaturated solution is relatively low when drug is absorbed from the donor at the biorelevant rate. In systems with lower absorption rates or no absorption at all, the driving force for KTZ crystallization increases, decreasing the flux across the hollow fiber membrane, thereby underestimating the absorption efficacy of a supersaturated KTZ solution.

3.3 Material and Methods

3.3.1 Materials

KTZ was donated by Laborate Pharmaceuticals (Haryana, India) and was used as received. 50 mM sodium phosphate buffer, pH 6.5, was prepared using monobasic sodium phosphate monohydrate and dibasic sodium phosphate heptahydrate, both purchased from Sigma-Aldrich Inc., MO and used as the aqueous medium in the donor and receiver. Hydrochloric acid (36.5 – 38.0%) was purchased from Sigma-Aldrich Inc., MO and used as received.

AGS absorption module was constructed per a method described earlier (Chapter 2). Briefly, modified polyethersulfone (mPES) hollow fibers were cut from a filtration module purchased from Spectrum Laboratories Inc. (C06-E005-10-N, Rancho Dominguez, CA), placed in a laser-cut plexiglass supporting framework and potted into the inlet and outlet tubes emerging from the cuvette cap (Azzota Scientific, DE) using a UV cure silicone glue (Henkel Corporation, OH). The hollow fibers used here had L=5 cm, d=1 mm and molecular weight cut-off (MWCO) of 5 kDa.

3.3.2 Crystalline and Amorphous Solubility of KTZ

The crystalline solubility of KTZ in 50 mM sodium phosphate buffer at pH 6.5 was determined by equilibrating excess solid drug in aqueous medium for 48 hours at 37℃. Undissolved solids were separated by centrifugation in a Marathon 26KMR microcentrifuge (Thermo Fisher Scientific Inc., MA) at 14,800 rpm for 60 min. KTZ concentration in the supernatant was measured by UV spectroscopy (Cary 100 Bio, Agilent Technologies, Inc., CA, path length 10 mm) at λ_{max} = 225 nm.

Amorphous solubility was determined using a method described previously.[102] Solubilized KTZ (6 mg/mL) in pH 1.5 HCl was titrated into pH 6.5 phosphate buffer at a rate of 10 µL/min. Titration was performed in a 3 mL quartz cuvette at 37°C under constant stirring. Light scattering by phase separated KTZ was monitored by UV spectroscopy at a non-absorbing wavelength of 312 nm. The onset of UV-extinction at 312 nm indicated the appearance of LLPS and the corresponding concentration was taken to be the amorphous solubility of KTZ. pH of the solution after titration was 6.43. KTZ standard solutions (1 - 140 µg/mL) were prepared in pH 6.5 phosphate buffer with pre-dissolved 3 mg/mL (2-hydroxypropyl)-β-cyclodextrin (Sigma Aldrich, MO). Standards and samples were analyzed in triplicate.

3.3.3 Polarized Light Microscopy

To characterize the dispersed phase, 66 µL of solubilized KTZ in pH 1.5 HCl solution, at concentrations of 0.75 mg/mL and 3.79 mg/mL, was added to 3 mL pH 6.5 phosphate buffer to generate solutions with concentrations below (20 µg/mL) and above (100 µg/mL) the LLPS onset concentration, respectively. A small aliquot of the solution (containing the dispersed phase) was placed between a glass slide and a coverslip and was observed using a polarized light microscope at 40x magnification (Eclipse E200, Nikon Co., Tokyo, Japan).

3.3.4 KTZ Permeability Coefficient across PES Hollow Fiber Membrane

Mass transport of KTZ across PES hollow fiber membranes from solutions at different sub-solubility concentrations was evaluated using the AGS. 50 mM pH 6.5 phosphate buffer was pumped at 160 µL/min flow rate into the intraluminal space of 5 hollow fibers in the absorption module using a syringe pump. Three concentrations of KTZ, 2.5, 4.0 and

5.5 µg/mL were prepared separately in 50 mM pH 6.5 phosphate buffer. Then, 2.5 mL of each solution was added to the donor cuvette and runs were conducted in triplicate for 120 minutes at 37℃. Drug concentration in the extraluminal fluid was continuously monitored by taking UV spectrophotometric measurements at 225 nm. The permeability coefficient, *P*, of KTZ across the PES membrane was estimated by fitting the experimental donor concentration (C_{EL})-time (t) profiles to Eq. (3.1) and then using Eq. (3.2) (based on the theory developed in Chapter 2).

$$C_{\mathrm{EL}}(t) = C_{\mathrm{EL}}(0)e^{-k_{\mathrm{a,AGS}}t} \tag{3.1}$$

where $C_{\mathrm{EL}}(0)$ is the initial extraluminal KTZ concentration (2.5, 4.0 or 5.5 µg/mL). and

$$k_{\mathrm{a,AGS}} = \left(\frac{Q}{V}\right)\left(1 - e^{-\frac{NPA_{\mathrm{IL}}}{Q}}\right) \tag{3.2}$$

is the apparent "absorption rate constant" of the AGS, which depends on the number of hollow fibers (*N)*, receiver fluid flow rate (*Q)*, and volume of the extraluminal fluid (*V)*. The term A_{IL} represents the intraluminal surface area of a single hollow fiber, which is determined by its length and inner diameter. For the experiments determining *P*, the following parameter values were operative: *N*=5, *Q*=160 µL/min, *V*=2.5 mL, and A_{IL}=1.57 cm^2. (A full description of the absorption module can be found in Chapter 2).

3.3.5 AGS Tuning and Validation

With the value of *P* in hand, the AGS was tuned to absorb KTZ with a physiologically relevant rate constant, k_a=0.013 min^{-1}.[107] To do so, Eq. (3.2) was used to select the intraluminal fluid flow rate (*Q*) and hollow fiber number (*N*) to obtain a $k_{\mathrm{a,AGS}}$ corresponding to physiological k_a. (The parameters *V* and A_{IL} were the same as before.)

Then, a mass transport study from an initially saturated solution of KTZ in pH 6.5 phosphate buffer donor was conducted at 37℃ into the same drug-free buffer that was pumped into the tuned AGS. A validating estimate of $k_{a,AGS}$ was obtained by fitting the extraluminal concentration-time profile to Eq. (3.1) and comparing it to the "target" value, k_a.

3.3.6 Study of Simultaneous Desupersaturation and Absorption from KTZ Supersaturated Solutions using the Tuned AGS

KTZ mass transport studies from supersaturated solutions in the donor were conducted using the tuned AGS to simulate absorption at a biorelevant rate. The pH-shift method was used to generate supersaturated solutions of three concentrations, 20, 100 and 140 µg/mL, the former being below and the latter two being above the amorphous solubility concentration of KTZ. Briefly, KTZ was dissolved in pH 1.5 HCl at concentrations 0.75, 3.79 and 5.25 mg/mL. Then, 66 µL of each of the acidic stock solutions was added to 2.434 mL of pH 6.5 phosphate buffer in a 3 mL UV-Vis spectrophotometer cuvette, which we call the donor cuvette. Intraluminal fluid flow was initiated, and the absorption module was inserted into the donor cuvette immediately upon generation of the supersaturated solution. KTZ concentrations in the donor and flow-through cell were monitored at 37℃ for 60 minutes. Wavelength scans from 340 nm to 200 nm at the rate of 465 nm/minute were started within a minute of supersaturation generation and were conducted every 30 seconds, alternating between the drug donor and flow-through cells. Intraluminal drug concentrations were determined from the UV absorbance profiles at 225 nm and donor diffusible drug concentrations were determined by second derivative spectroscopy (to mitigate particle scattering effects[108,109]), also at 225 nm. To gain more insight into the

evolution of the dispersed phase, extinction-time profiles of KTZ solution in the donor at a non-absorbing wavelength of 312 nm were also recorded for all runs.

To demonstrate the changes in KTZ donor solution phase behavior when the drug is removed at rates lower than the biorelevant (i.e. physiological) rate, the intraluminal fluid was run at two sub-biorelevant flow rates, while otherwise maintaining the same experimental conditions as those used above in the studies with the optimized, biorelevant AGS. Additionally, 'closed no-absorption' experiments were conducted by suspending hollow fibers devoid of intraluminal buffer in the drug donor. All measurements were carried out in duplicate.

Using the quasi-steady state model for absorption in the AGS (developed in Chapter 2), the intraluminal drug concentration exiting the hollow fiber module, $C_{IL}(L,t)$, is given by

$$C_{IL}(L,t) = C_{EL}(t)\left[1 - exp\left(-\frac{NPA_{IL}}{Q}\right)\right] \tag{3.3}$$

The cumulative amount, $AMT(t)$, of KTZ absorbed by the intraluminal fluid at time *t=60 min* was calculated by multiplying the area under the intraluminal concentration-time curve, $AUC_{\mathrm{IL},0-\mathrm{t}}$, by the corresponding flow rate, i.e.

$$AMT(t) = AUC_{\mathrm{IL},0-\mathrm{t}} \times Q \tag{3.4}$$

3.4 Results

3.4.1 KTZ solubility measurements

The crystalline solubility of KTZ in pH 6.5 phosphate buffer at 37℃ was found to be 5.5 ± 0.3 µg/mL. To determine the critical concentration at which LLPS occurred, UV extinction at a non-absorbing wavelength of 312 nm was monitored as a function of KTZ concentration added to the cuvette. It is clear from the UV extinction data in ***Figure 3.2*** (black circles) that turbidity (indicating the presence of a dispersed phase) was negligible at low drug concentrations, slightly increased at 70 µg/mL before rising abruptly at 80 µg/mL, the LLPS onset or amorphous solubility concentration of KTZ. The slight increase at 70 µg/mL may be attributed to crystalline precipitation which can also cause an increase in extinction. Induction of crystalline precipitation occurs at lower concentration of around 45 µg/mL (grey squares *in* ***Figure 3.2***) when the rate of addition of KTZ concentrated stock solution to pH 6.5 phosphate buffer was reduced from 10 to 3 µL/min due to supersaturation existence for longer time duration. KTZ added to the supersaturated solution above amorphous solubility was immediately added to the amorphous drug-rich phase resulting in further increase in extinction.

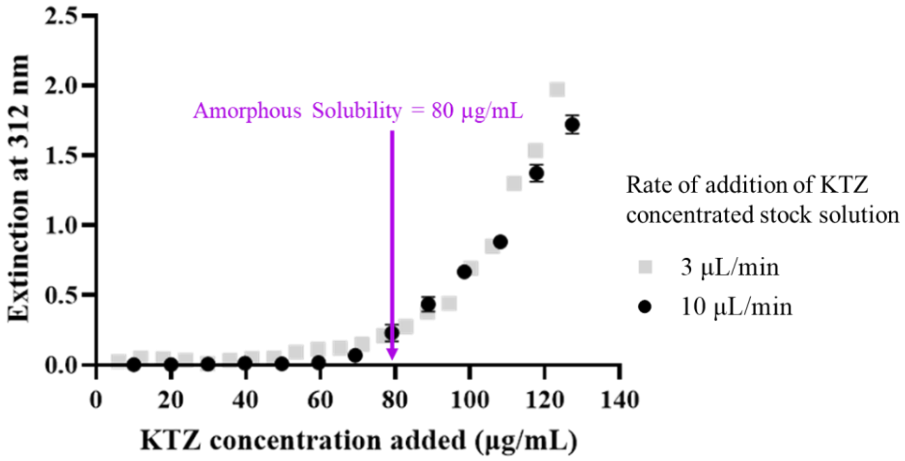

Figure 3.2. Determination of KTZ LLPS onset concentration in pH 6.5 phosphate buffer at 37℃ using UV spectroscopy. Concentration of drug added corresponding to the point of abrupt increase in UV-extinction is 80 µg/mL, the amorphous solubility concentration of KTZ.

3.4.2 Characterization of the KTZ Dispersed Phase

KTZ is regarded as a slow crystallizer.[106] At a concentration of 100 µg/mL, the solution is visually cloudy. Examination of this system under cross polarized light revealed the growth of small, non-birefringent, spherical droplets dispersed in the aqueous continuous phase (***Figure 3.3a***, at 5 and 18 minutes), suggesting that LLPS had occurred above the 'miscibility' concentration of KTZ resulting in the formation of an amorphous, drug-rich phase.[102] When observed for about an hour, this metastable solution, in the next stage starting at around 11 min, is characterized by crystal nucleation and growth with the disappearance of surrounding droplets (***Figure 3.3a*** at 18 and 45 minutes). The zone of depletion grows with time, indicating solution mediated phase transfer from the amorphous liquid phase into the solid crystalline phase.[110] On the other hand, observation of a 20 µg/mL solution under cross polarized light after 45 minutes of supersaturation generation

indicated the presence of only birefringent crystals (***Figure 3.3b***). At 20 µg/mL, KTZ solution is below the LLPS onset concentration, but it is still supersaturated with respect to the crystalline drug. As a result, this metastable solution undergoes precipitation, but only as crystallization.

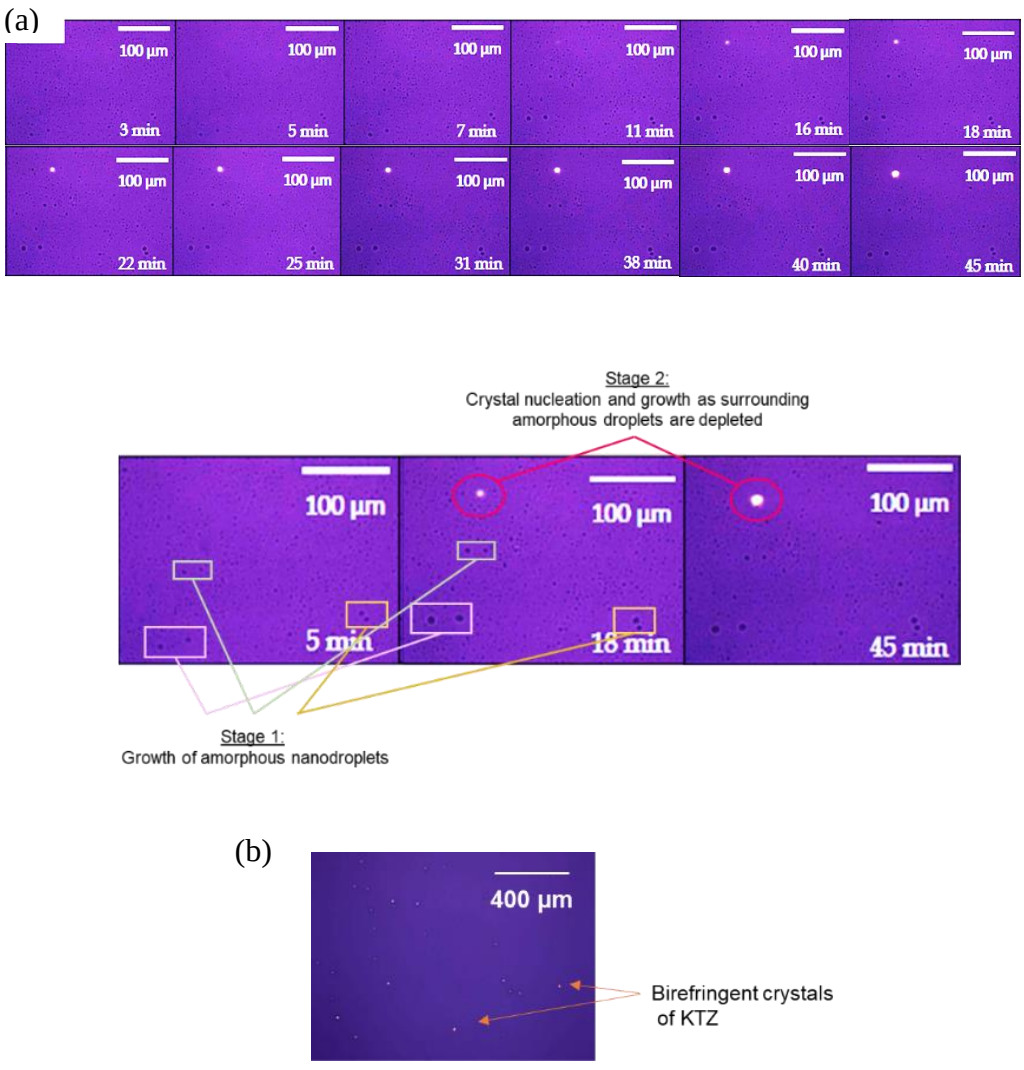

Figure 3.3. Polarized light micrographs showing **(a)** evolution of a 100 µg/mL (above amorphous solubility) KTZ supersaturated solution over 45 minutes as it first undergoes LLPS to form non-birefringent amorphous droplets dispersed in a continuous pH 6.5 phosphate buffer medium. The growth of droplets is then followed by birefringent crystal formation and simultaneous depletion of surrounding droplets. **(b)** Formation of only birefringent KTZ crystals at the end of 45 minutes in a 20 µg/mL (below amorphous solubility) supersaturated solution.

3.4.3 Estimation of KTZ Permeability Coefficient across PES Hollow Fiber Membrane

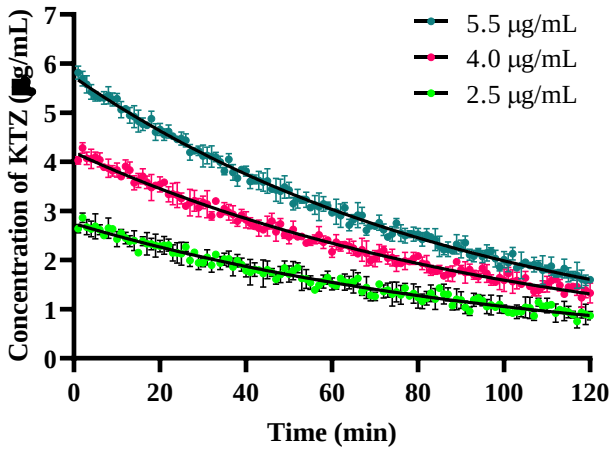

Figure 3.4. Donor drug concentration-time plots at three different starting drug concentrations of KTZ. The experimental data sets were fit to Eqs. (3.1) and (3.2) (black lines) to obtain $P = (\ 6.74\ \pm 0.35\ ) \times\ 10^{-5}$ cm/sec.

KTZ mass transfer experiments across the hollow fiber membrane were conducted using concentrations at sub-solubility levels in pH 6.5 phosphate buffer at 37 ℃. The AGS was operated at an intraluminal fluid flow rate Q=160 μL/min, total hollow fiber area for absorption NA_{IL}=7.85 cm^2 and donor volume of V=2.5 mL. ***Figure 3.4*** shows the donor (extraluminal) concentration-time profiles of KTZ obtained from continuous UV spectrophotometric measurements. The decline in donor drug concentration due to absorption across the hollow fibers was exponential and after 120 minutes, about 70% of the drug was cleared from the KTZ donor solution. The permeability coefficient, P, was estimated by fitting the respective donor concentration-time series obtained to Eq. (3.1) and then using Eq. (3.2). From these curves, P of KTZ across the mPES hollow fiber membrane was estimated to be $(6.74\ \pm 0.35)\ \times\ 10^{-5}$ cm/s.

3.4.4 Tuning of AGS to Mimic Physiologically Relevant Rate of KTZ Absorption

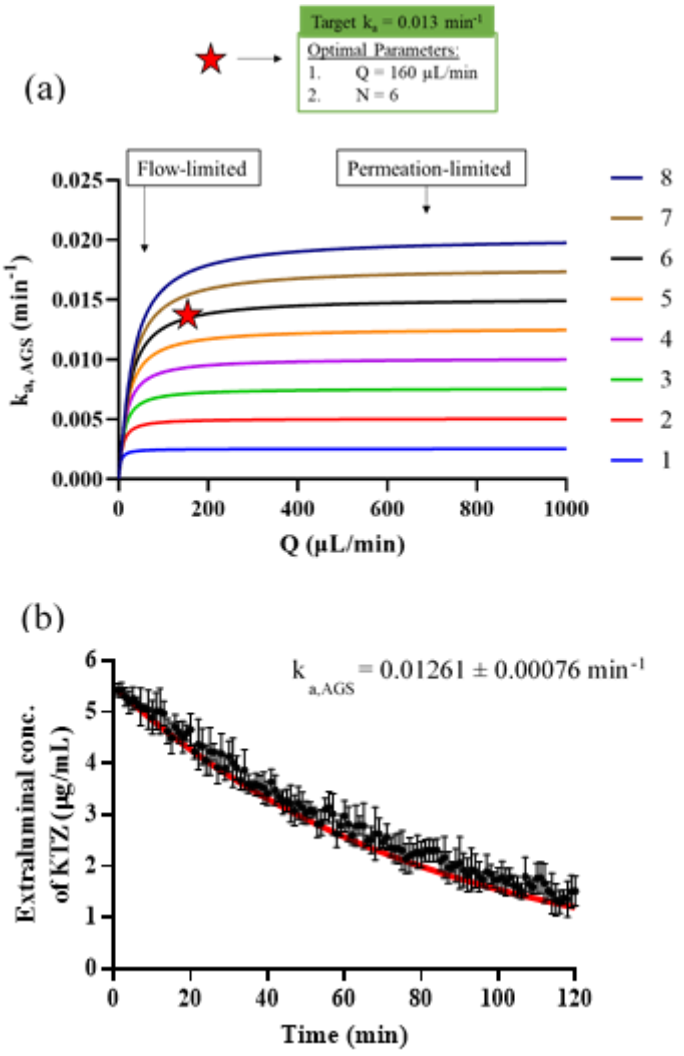

Figure 3.5. **(a)** Family of plots of $k_{a,AGS}$ of KTZ as a function of hollow fiber surface area for absorption (NA_{IL}, 1.57 - 12.56 cm^2) and receiver fluid flow rate (Q, 0 – 2 mL/min) obtained using Eq. (3.2). AGS operating parameters were optimized to obtain a target $k_{a,AGS}$ of 0.013 min^{-1}. Volume of extraluminal fluid, V, was maintained at 2.5 mL. **(b)** Donor concentration-time plot of KTZ at a starting concentration of 5.5 µg/mL obtained using the optimized AGS. Red line represents the fit of Eq. (3.1) to the experimental data to estimate $k_{a,AGS}$ to be 0.01261 ± 0.00076 min^{-1}.

The physiological absorption rate constant of KTZ is k_a= 0.013 min^{-1}.[107] Upon setting the intraluminal fluid flow rate at Q=160 µL/min and the number of hollow fibers at N=6, this rate constant ($k_{a,AGS}$) is attained (red star in ***Figure 3.5a***). ***Figure 3.5b*** displays a run of the AGS with these parameters, starting with a saturated solution of KTZ in the donor. The parameter $k_{a,AGS}$ was estimated by fitting the experimental concentration-time profile to Eq. (3.1) (red line in ***Figure 3.5b***) and was found to be 0.01261 ± 0.00076 min^{-1} which is close to the physiological k_a for KTZ.

3.4.5 Simultaneous Desupersaturation and Absorption from KTZ Supersaturated Solutions using the Tuned AGS

3.4.5.1 'Closed' versus 'Open' SSF Testing Systems

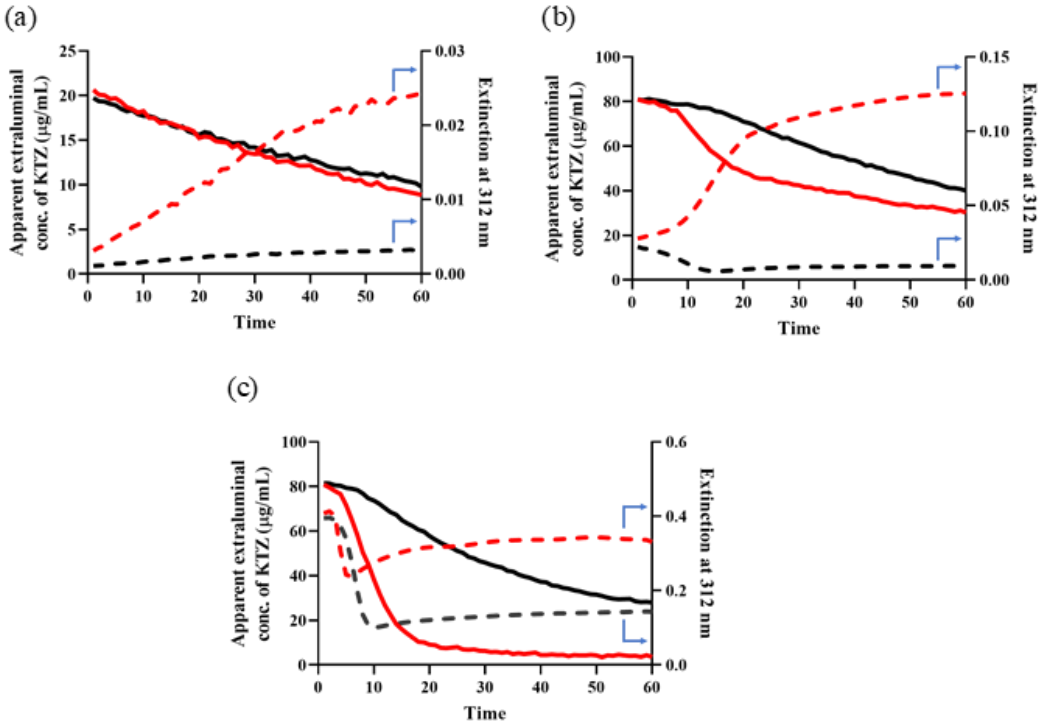

Figure 3.6. Apparent KTZ concentration (solid line)- and extinction (dashed line)-time profiles obtained with 'Control' (no absorption module, red line) and 'Test' (tuned AGS, black line) at three different supersaturating concentrations of **(a)** 20 µg/mL, **(b)** 100 µg/mL and, **(c)** 140 µg/mL.

The time evolution of phases in KTZ supersaturated solutions generated by the pH-shift method in the donor cuvette below (20 µg/mL) and above (100 and 140 µg/mL) the LLPS onset concentration (80 µg/mL) was monitored with and without the "physiologically" tuned absorption module. Henceforth, systems with the tuned AGS will be referred to as 'test' while 'control' refers to those that are 'closed' (no flow in the absorption module) with respect to the drug in solution. Phase evolution was studied by continuously monitoring light scattering (UV extinction) and diffusible drug concentration (second derivative UV absorbance) in pH 6.5 phosphate buffer donor media for 60 minutes at 37℃ (***Figure 3.6***).

Since KTZ supersaturated solution is metastable with respect to the stable crystalline form, precipitation by crystallization can occur (***Figure 3.3b***). ***Figure 3.6a*** shows the mean extinction- and concentration-time profiles from one hour 'control' and 'test' runs starting at 20 µg/mL KTZ extraluminal concentration. In the 'control', where no absorption occurs, reduction in drug concentration is solely due to crystallization (solid red line). The decline in drug concentration in the 'control' was also accompanied by a nonlinear increase in extinction (dashed red line) due to light scattering as nucleation and growth of a stable crystalline form proceed in the cuvette. Relative to the control, the rate and extent of increase in light scattering in the 'test' solution is much less (dashed black line), as absorption into the lumen reduces drug concentration in the donor, which in turn decreases the driving force for crystallization. Tuning of the AGS to attain an absorption rate constant of 0.013 min^{-1} translates to a $t_{1/2}$ of 55 minutes. Thus, in the 'test' runs, the decline in drug concentration (solid black line) to about 50% of the starting concentration after 1 hr can be attributed largely to absorption. It should be noted that second derivative UV-spectroscopy

measurements made here, while eliminating the contribution due to light scattering by drug precipitate particles (amorphous and crystalline), does not necessarily eliminate their contribution to UV absorption, thereby somewhat overestimating extraluminal solution concentration.[43,111,112] This allows only for qualitative and not quantitative analysis of the KTZ concentration evolution in donor. The wavelength where extinction was recorded, 312 nm, can be considered non-absorbing in relation to both the molecularly dissolved drug as well as drug precipitate particles since we did not see a concentration-dependent change in second derivative intensity at that wavelength. The increase in intensity or extinction at 312 nm can then be solely attributed to light scattering by the growing drug precipitate in the extraluminal solution.

Figure 3.6b shows the apparent concentration- and extinction-time profiles of 'control' and 'test' samples at 100 µg/mL starting drug concentration in the donor. Although 100 µg/mL KTZ was added, only about 80 µg/mL KTZ was measured in 'test' and 'control' solutions at the start of the run. This is the limit of miscibility or amorphous solubility of KTZ, and the additional 20 µg/mL forms the dispersed phase. Concentration remains relatively constant for the first 7 and 15 minutes in the 'control' and 'test' runs, respectively, and then declines. The subsequent decline of drug concentration in the 'control' can be attributed to drug crystallization. Moreover, the extinction of the 'control' samples increases slowly at first, accelerates, and slows down again, presumably due to the appearance and growth of amorphous droplets followed by crystal nucleation and growth with simultaneous dissolution of the amorphous phase. This solution phase behavior was also observed when 100 µg/mL supersaturated solution was observed under cross-polarized light (***Figure 3.3a***). The time until which extinction increases slowly corresponds

closely with the duration of constant drug concentration in solution, indicating a relatively stable amorphous precipitate. In the 'test', the decline in drug concentration is due to both absorption and crystallization. Extinction on the other hand remains constant at first, indicating the formation of an amorphous dispersed phase, and then decreases within 15 minutes, which corresponds to the duration of constant drug concentration. This is probably due to rapid dissolution of amorphous droplets to replenish the drug in solution lost to absorption, which serves to maintain a constant solution concentration but depletes the dispersed phase of KTZ, resulting in declining extinction. This is followed by crystallization indicated by a steady increase in extinction, although the rate and extent are significantly lower compared to the 'control'.

As the concentration of drug added to solution increases, crystallization becomes highly favorable as the frequency of molecular collisions and stable nuclei formation increases. This is seen in the concentration- and extinction-time profiles of both 'control' and 'test' in ***Figure 3.6c*** when 140 µg/mL KTZ was added to pH 6.5 phosphate buffer, compared to the 100 µg/mL case. In the 'control,' following an initial high extinction due to larger and/or greater number of KTZ amorphous liquid droplets dispersed in the aqueous continuous phase, extinction decreases sharply as a result of rapid amorphous droplet dissolution to undergo solution-mediated phase transfer to the solid crystalline phase, which in turn causes a slight increase in light scattering and extinction. The concentration of KTZ, on the other hand, remains relatively constant in the first few minutes at 80 µg/mL and then rapidly decreases to its equilibrium solubility concentration due to crystallization. The 'test' extinction- and concentration-time profiles follow a similar trend but with longer crystallization induction time, slower drug concentration decline and lower rate and extent

of increase in extinction, indicating a lower degree of crystallization in the presence of the absorptive sink.

3.4.5.2 Significance of Simulating Absorption at a Biorelevant Rate

There is often a discrepancy between the *in vitro* prediction of the nature and extent of intestinal precipitation of a BCS-II weak base and the real outcome *in vivo*.[76,84,98,103,104] This discrepancy arises because many *in vitro* methods do not consider the effect of drug removal from the intestinal lumen by absorption at a biorelevant rate, especially for a high permeability drug. Plasma concentration-time profiles from a clinical trial of KTZ oral solution showed a fast absorption phase with a $t_{1/2}$ of about an hour.[113] Such rapid absorption can potentially reduce the driving force for crystallization. So, to test the hypothesis that precipitation may be overestimated when a sub-optimal gut simulator is used, lower-than-biorelevant absorption rates were also simulated by the AGS.

Of the various parameters that are available to the designer/operator of the AGS, the easiest to vary is the intraluminal fluid flow rate. In the following studies, 20, 100 and 140 µg/mL supersaturated solutions were generated by the pH-shift method in the donor, and the absorption module was operated at two sub-biorelevant intraluminal fluid flow rates, 40 and 80 µL/min.

Mean extraluminal and intraluminal concentration-time profiles obtained using the sub-biorelevant AGS are compared with those obtained using the biorelevantly tuned AGS (Q=160 µL/min) in ***Figure 3.7***. If there were no precipitation, these profiles would be predicted using Eqs. (3.1), (3.2), and (3.3). The predictions so obtained are represented by bands (calculated using mean ± SD of P) of the same color as the corresponding

experimental data sets (lines). Negative deviation from the predictions of intraluminal drug concentration absorbed determined experimentally should be indicative of relative non-availability of drug in the donor for absorption due to formation of drug aggregates and crystals (compared to free drug species), the hydrodynamic radii of which are larger than the pore size of the hollow fiber membrane (~ 2 nm, from manufacturer data sheet).

We first consider results for 20 µg/mL starting concentration of KTZ (***Figure 3.7a,b***). Notably, ***Figure 3.7a*** displays no obvious relation between intraluminal flow rate (if any) and the decay in extraluminal concentration. With increasing flow rate, absorption is faster, and the crystallization rate decreases, since the concentration of drug, and hence the driving force for crystal nucleation and growth, is lessened. The combination of these two trends makes it difficult to decouple them by looking at donor concentration alone. With increasing flow rate, as the residence time of the buffer in the hollow fiber lumen decreases, concentration of drug absorbed per unit volume of the intraluminal fluid decreases (***Figure 3.7b***). However, the cumulative dose fraction of free drug diffused into the intraluminal buffer medium from the donor after 60 min [*AMT*(60 min) as calculated using Eq. (3.4) normalized by dose], increases with increasing flow rate (***Figure 3.8***). The initial slow absorption can be attributed to the diffusional time-lag of KTZ across the hollow fiber membrane and the residence time of the buffer in the hollow fiber lumen, which increase with decreasing flow rate. The quasi-steady state model (developed in Chapter 2) did not take into account this delay, which explains the initial deviation of the predictions from the experimental data in all cases. Nevertheless, the predictions show larger deviations from the 40 and 80 µL/min experimental data points throughout the 60-minute run compared to

the 160 µL/min case. These observations indicate increasing extent of crystallization with slower absorption.

When 100 µg/mL KTZ supersaturated solution was prepared, the maximum concentration in the donor attained in all the systems was 80 µg/mL, the amorphous solubility of KTZ (***Figure 3.7c***). In the absence of crystallization, per earlier investigations, as the degree of supersaturation increases, the chemical potential and flux of drug across a membrane also increases, attaining a maximum at its amorphous solubility concentration.[55] Beyond the maximum miscibility concentration, the chemical potential and flux are constant. The predictions made here assumed maximum flux at 80 µg/mL, which remained constant even at higher dose concentrations. In the absence of crystallization, the predicted donor concentration-time profile indicates that the amorphous drug rich nanodroplets in dynamic equilibrium with the drug in solution immediately replenish the drug in solution lost to absorption, thereby maintaining the initial constant drug concentration (as determined by second derivative UV spectroscopy) in the donor. Once the amorphous phase is exhausted, the drug concentration decreases as does flux across the membrane. The 160 µL/min experimental dataset is in good agreement with the theoretical model, indicating the occurrence of drug-rich phase redissolution followed by a decline in drug concentration, both due to absorption and some crystallization (***Figure 6c,d***). At lower rates of absorption, however, decline in drug concentration begins earlier than predicted, indicating significant crystallization. Crystallization in the donor reduces the drug available for absorption, resulting in lower than predicted KTZ concentration absorbed by the intraluminal buffer at lower flow rates. Moreover, as the dose concentration increased from 20 to 100 µg/mL, the cumulative dose fraction of drug absorbed by the optimal and sub-

optimal AGS also increased due to higher KTZ free drug concentration and activity in solution, which increased its driving force for absorption (***Figure 3.8***). Similar to the 20 µg/mL case, highest KTZ dose fraction was absorbed after 60 minutes with the physiologically tuned AGS and decreased when sub-optimal intraluminal fluid flow rates were used.

At 140 µg/mL dose concentration in the donor, significant crystallization, subsequent decline in donor drug concentration, and deviation from the model prediction occur in all cases (***Figure 3.7e***). The rate of decline is the lowest in the 160 µL/min case, followed by 80 µL/min, then 40 µL/min and the 'control' cases. From ***Figure 3.7f*** it is clear that the predicted intraluminal concentration-time profiles show significant deviation from the experimental data in all the cases. At 140 µg/mL dose concentration, irrespective of the flow rate, a lower fraction of drug is absorbed relative to a lower dose concentration of 100 µg/mL due to extensive crystallization (***Figure 3.8***).

It is interesting to note that at all dose concentrations, the fraction of KTZ absorbed is lower than 0.5, approximately the fraction of drug absorbed from a saturated solution in 60 minutes using optimized AGS (***Figure 3.5b***). This is due to crystallization in the donor containing KTZ supersaturated solution that reduces the free drug fraction available for absorption.

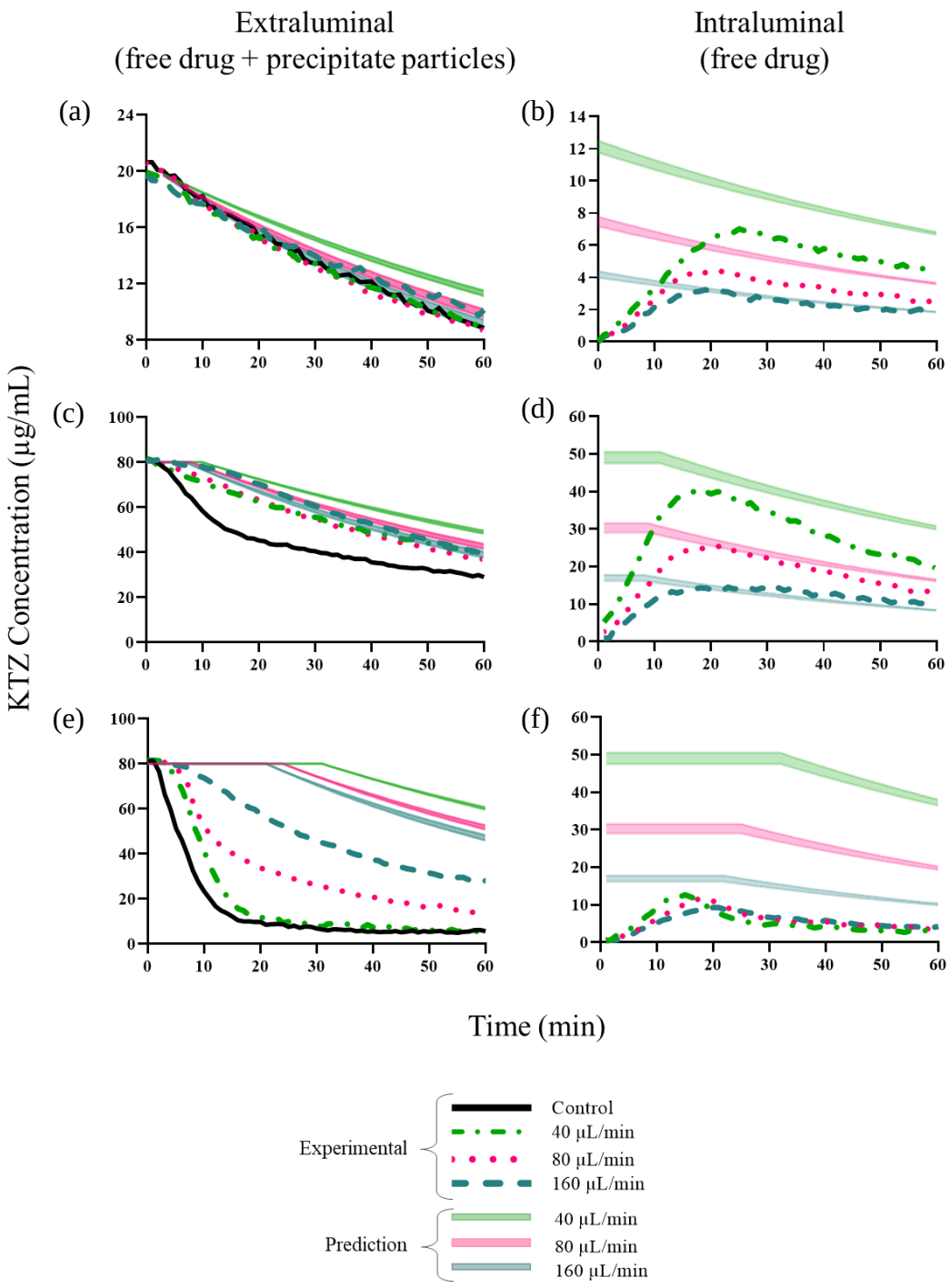

Figure 3.7. KTZ extraluminal concentration-time **(a), (c) and (e)** and intraluminal concentration absorbed with time **(b), (d) and (f)** profiles obtained with three different intraluminal buffer flow rates, 40, 80 and 160 (optimal) µL/min and 'Control' at three different initial concentrations of 20, 100 and 140 µg/mL, respectively. The predictions obtained using Eqs. (3.1), (3.2), and (3.3) if there were to be no crystallization are represented as bands of the same color as the experimental data set that they are predicting.

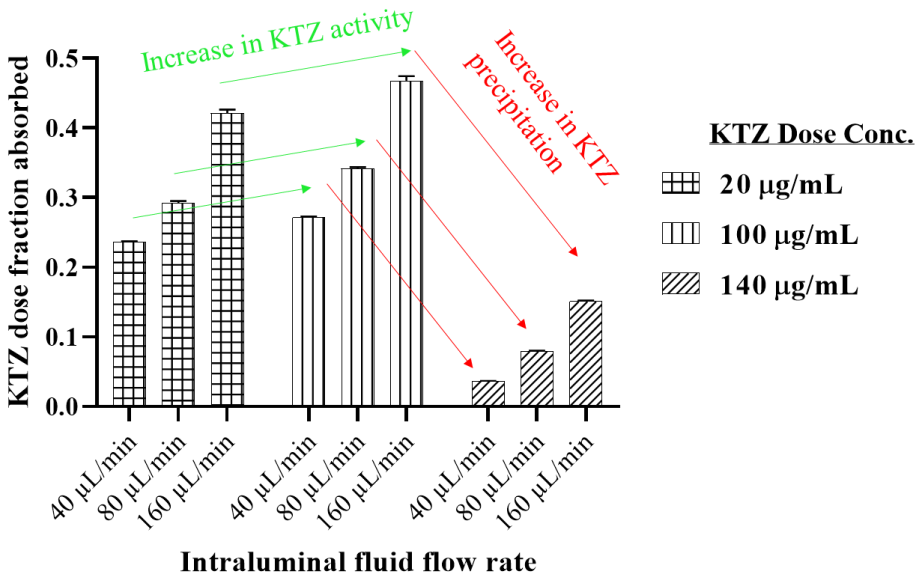

Figure 3.8. KTZ dose fraction absorbed [dose-normalized *AMT*(60min) determined using Eq. (3.4)] in 'tests' with sub-optimal and optimal AGS at three supersaturating concentrations, 20 (below amorphous solubility), 100 and 140 µg/mL (above amorphous solubility).

3.5 Discussion

There is a well-documented need in the literature, especially in reference to KTZ, to not only include an absorptive sink during *in vitro* dissolution testing, but also be able to characterize precipitation behavior upon supersaturation generation.[98,103,104] If KTZ supersaturated solution precipitates to its metastable amorphous phase, the solution will still be supersaturated with respect to the stable crystalline form, thereby retaining the advantage of enhanced solute activity, and hence flux.[55] Moreover, the amorphous form, in contrast to the crystalline form, can readily redissolve to replenish drug in solution lost to absorption. *In vivo* KTZ precipitate is described to be amorphous.[77] However, predominantly crystalline KTZ precipitate was obtained during *in vitro* dissolution studies

reported in the literature, due either to utilization of non-sink dissolution testing or application of non-biorelevant flow rates of dissolution media in a flow through system.[98,103,104] This drawback can be sufficiently addressed by a dissolution testing system that allows a biorelevant rate of drug clearance from the simulated intestinal lumen for a highly permeable BCS-II compound.

KTZ is a BCS-II compound, supersaturated solutions of which can undergo LLPS above the amorphous solubility concentration of 80 µg/mL (***Figure 3.2***) followed by crystallization (***Figure 3.3a***). Below 80 µg/mL, crystallization is the only mechanism of concentration reduction of the diffusible drug species (***Figure 3.3b***). The hollow fiber based AGS introduced in Chapter 2 was tuned to absorb KTZ at a physiological rate (***Figure 3.5a***). Upon generation of supersaturated solutions of KTZ in the extraluminal fluid, crystallization was signaled by an increase in extinction (***Figure 3.6***). Although an increase in extinction was observed in both the 'control' solution as well as the 'test' with the tuned AGS, the rate and extent of light scattering was higher in the 'control,' indicating higher drug crystallization. This suggests that a traditional, closed USP dissolution testing tool would overpredict precipitation that occurs in the intestinal lumen, thereby underpredicting the performance of supersaturating formulations.

Moreover, absorption from KTZ supersaturated solutions using the physiologically tuned AGS was compared with that obtained using the sub-biorelevant setup (***Figure 3.7***). Eqs. (3.1), (3.2) and (3.3) were used to predict the extra- and intraluminal concentration profiles sans crystallization. In the extraluminal fluid, at the lowest absorption rate, non-exponential decline and largest deviation from the predicted profiles was observed, indicating crystallization. Moreover, in the 100 and 140 µg/mL dose concentration cases,

crystallization induction was significantly slower with the physiologically tuned AGS relative to the sub-biorelevant AGS and 'control'. In the intraluminal fluid, on the other hand, lower-than-predicted concentration-time profiles were observed at all dose concentrations at lower flow rates.

To quantify and compare the influence of crystallization on flux in all the cases, the excess in the predicted amount of KTZ absorbed relative to experimental, $\Delta_{predicted\text{-}experimental}$ [experimental amount absorbed determined using Eq. (3.4), predicted amount absorbed determined using Eq. (3.3) and (3.4)] is plotted in ***Figure 3.9***. Greater the difference, higher is the flux reduction due to crystallization. Overall, as the dose concentration increases, unsurprisingly, $\Delta_{predicted\text{-}experimental}$ also increases. However, for all dose concentrations, as we increase the flow rate, $\Delta_{predicted\text{-}experimental}$ decreases indicating lower crystallization in the donor, which allows higher flux of the diffusible drug species across the hollow fiber membrane.

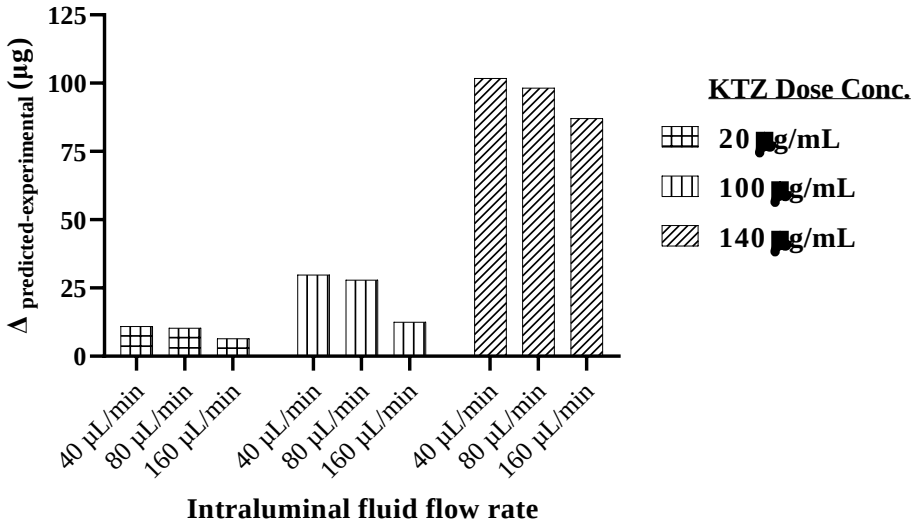

Figure 3.9. Excess in the predicted amount of KTZ absorbed relative to experimental, $\Delta_{predicted\text{-}experimental}$ plotted as a function of extraluminal dose concentrations and intraluminal fluid flow rate.

The simplicity of the AGS system and the need to use only a small volume and mass of the dissolution media and drug formulation, respectively, allows its applicability to screen SSFs such as amorphous solid dispersions in a high-throughput manner, and study how additives such as polymers, surfactants or bile salts, added in either formulation or dissolution media, may influence the drug solute's thermodynamic activity and ultimately its absorption. In fact, the importance of considering activity- rather than concentration-based supersaturation in correctly predicting membrane transport rate has been demonstrated recently.[14,114] Moreover, to further distinguish non-bioavailable ionized from bioavailable unionized species, the hollow fiber membranes, for example, may be coated with phospholipids, as the uncoated hollow fibers will indiscriminately absorb both, and can overestimate formulation efficacy, especially for drugs formulated as salts.[115] A logical next step would also be to reduce the diffusional time-delay in absorption of drug into the intraluminal buffer by utilizing a much thinner HF membrane compared to that which has been used in this study (~125 μm).

3.6 Conclusion

A simple and efficient *in vitro* dissolution/absorption testing tool, the AGS, was tuned to simulate absorption of a model BCS-II drug, KTZ, at its physiologically observed rate. The supersaturating solutions were evaluated at, below and above KTZ's amorphous solubility concentration in the presence and absence of an absorptive sink. Direct evidence of crystallization was obtained by measuring extinction of donor solutions, the rate and extent of increase of which was found to be higher in the 'closed' system relative to the physiologically tuned AGS. Indirect evidence of crystallization was obtained by evaluating the cumulative amount absorbed by the intraluminal fluid as only free drug species will be available for absorption. Rate of absorption was found to be key in determining the degree of precipitation; $\Delta_{\text{predicted-experimental}}$ increased as the absorption rate decreased indicating greater deviation from an exponential, first order decline of KTZ extraluminal concentration-time profile due to increasing precipitation which in turn decreases the absorptive flux across the hollow fiber membrane. This study illustrates the key role of including an absorption module during the dissolution testing of potential SSFs of high permeability drug molecules and simulating absorption with a physiologically observed rate constant.

Chapter 4: Understanding the Impact of Absorption on *In Vitro* Dissolution, Speciation and Precipitation of Amorphous Solid Dispersions

4.1 Graphical Synopsis

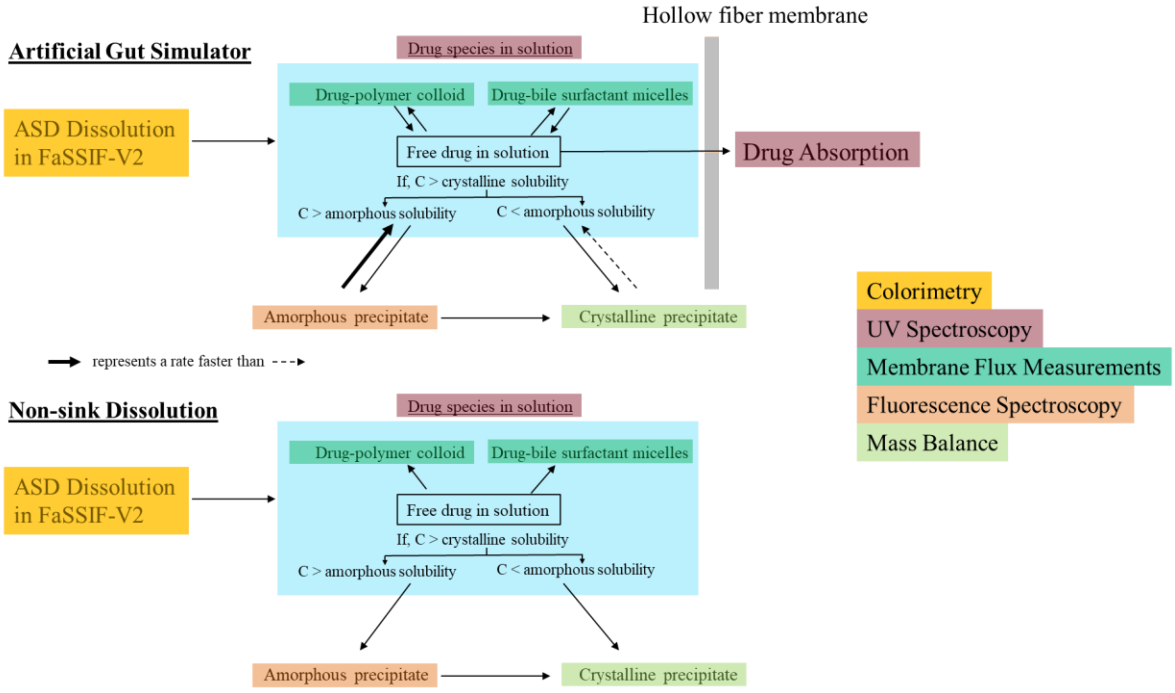

Figure 4.1. Schematic representation of analytical techniques used to understand the exchange processes that occur *in vitro* upon amorphous solid dispersion (ASD) dissolution in the presence and absence of an absorptive sink.

4.2 Introduction

Amorphous solid dispersions (ASDs) are becoming increasingly relevant as oral drug formulations as more brick dust molecules enter the development pipeline.[89,90] These are molecules whose solubility and dissolution rate in an aqueous medium are restricted by their high crystal lattice energy, low degree of molecular flexibility and high hydrophobicity.[116] In an ASD, the amorphous form of the drug is molecularly dispersed in a relatively hydrophilic polymer matrix. The disordered nature of the amorphous form and

reduced hydrophobicity afforded by the polymer are responsible for solubility and dissolution rate enhancement of the drug.[117]

Complex gastrointestinal exchange processes exist after ASD dissolution as the drug is distributed across free and various bound species (***Figure 4.1***).[118] However, only free, molecularly dissolved drug is bioavailable.[14,114,119] ASDs can release drug at concentrations above its crystalline solubility in a super-soluble or supersaturated state with higher thermodynamic activity which translates to increased drive for absorption.[55] The enhanced solubility of the amorphous form over the crystalline solubility represents the drug's miscibility limit in the media, also known as amorphous solubility.[102] When the dose concentration of the drug exceeds its amorphous solubility, glass-liquid or liquid-liquid (depending on the resultant species' T_g) phase separation (LLPS) results in formation of a molecularly disordered colloidal amorphous precipitate dispersed in the dissolution media.[90] The large surface area of the precipitate allows rapid redissolution of the drug to replenish the drug in solution lost to absorption.[90] The drug in solution and/or amorphous precipitate can also revert to a low energy crystalline polymorph, the induction probability and crystallization rate of which increases with increasing drug concentration (as demonstrated with KTZ in Chapter 3). Polymer released from the ASD can stabilize this metastable, supersaturated solution against crystallization.[120]

Apart from amorphous and crystalline precipitate, earlier reports have also indicated the formation of drug species bound to bile micelles and lipid nanoparticles of the dissolution media as well as polymer and surfactant excipients released from the drug formulation.[14,119,121] Drug from these species can also disassociate to replenish free drug in solution as absorption proceeds. *In vivo,* these bound drug species along with the free drug

constitute a gastric milieu that is very dynamic in nature due to continuous drug removal by absorption. In vitro assessment of ASD performance, on the other hand, is commonly performed under closed, non-sink conditions afforded by the standard United States Pharmacopeia (USP) dissolution testing apparatus which allows only static equilibria between various drug species. It has also been shown in an earlier study that a closed dissolution testing apparatus increases the crystallization propensity of supersaturated solutions (Chapter 3). This would prevent the assessment of full potential of ASDs or worse, may *underestimate* their efficacy.

To simulate dynamic gastrointestinal equilibria, *in vitro* tools have been developed that allow continuous drug removal. The USP Apparatus 4 or the flow-through cell and the biphasic dissolution testing system, although employing different principles of operation, when optimized can mimic *in vivo* rates of drug removal from the intestinal lumen.[105,122] While the USP Apparatus 4 establishes sink conditions by maintaining a continuous flow of fresh dissolution medium to replace the drug-laden medium when operated in open-loop mode, the volumes employed are usually unphysiologically large.[42] The biphasic dissolution testing system, on the other hand, lacks a membrane between the aqueous dissolution medium and the organic absorptive sink.[123] Free drug species as well as drug nanoaggregates and complexes with media components and/or excipients can indiscriminately partition into the organic phase. Moreover, *in vivo* absorption is a kinetic process whereas partition coefficient of a drug is an equilibrium parameter that may not accurately represent physiological rate of drug removal from the intestinal lumen. Manual sampling (e.g. using microfilters) and analytical techniques (e.g. UV spectroscopy, HPLC) used commonly in conjunction with the above dissolution testing tools do not sufficiently

filter and detect only free drug species.[43] These caveats in drug solution filtration and measurement may significantly *overestimate* the ability of an SSF to provide drug in a supersaturated, highly bioavailable form.

Employment of membrane-based assay systems such as Parallel Artificial Membrane Permeability Assays (PAMPAs), the ultrathin, large-area membrane (UTLAM), side-by-side, or MicroFLUX™ (μFLUX) and MacroFLUX™ diffusion cells, wherein the apical/donor and basal/receiver compartments are separated by a size-exclusion membrane barrier, has provided insights into how passive permeation of drug molecules may influence drug release, dissolution, precipitation and speciation.[24,54–56,120,124–126] However, aside from the UTLAM system, these systems might be quite inflexible to scale-up to obtain physiologically relevant absorption rates. The major limitation of these systems is the small surface area for absorption relative to the volume for dissolution, resulting in lengthy, non-physiological experimental time scales (e.g. 16 hours with a side-by-side diffusion cell compared to 2-4 hours of gut transit time).[58,59]

Using cell lines such as Caco-2 and MDCK instead of artificial membranes allows one to screen active and passive permeation mechanisms as well as efflux, if any.[45,127,128] However, these assays often suffer from high inter- and intra-lab variability, time consuming and expensive preparation steps, relative incompatibility with certain pharmaceutical excipients, and lower absorption surface area compared with the intestinal membrane.[129,130] Moreover, considering that 80-95% of commercial compounds are absorbed primarily by passive diffusion, there is a great interest in rapid and inexpensive simultaneous dissolution-permeation assays.[52]

An inexpensive and rapid screening tool called the 'Artificial Gut Simulator (AGS)' introduced in Chapter 1 consisting of hollow fibers in the absorption module can be used to screen ASDs. The hollow fiber module is suspended in a UV spectrophotometric 'donor' cuvette while a 'receiver fluid' buffer is pumped continuously through a flow-through cell following the hollow fiber lumen to allow continuous, in-line measurement of donor and receiver (intraluminal) drug concentrations. The low membrane molecular weight cutoff (MWCO) of the hollow fiber membrane allows permeation of mostly free drug species into the receiver media, while the non-bioavailable species in aggregates and precipitate remain unabsorbed. Operating parameters of the AGS such as the surface area of hollow fibers, receiver fluid flow rate and volume of donor medium are directly controlled by the designer/operator and can be tuned to mimic the known *in vivo* absorption rate constant of a drug under study, when that drug is present at or below saturation in the gut.

In this study, ASDs of ketoconazole (KTZ) are formulated with hypromellose acetate succinate (HPMCAS) polymer, which is known to interact favorably with KTZ.[131] The goal of the present study is to introduce an analytical paradigm to systematically elucidate the impact of various drug species formed during ASD dissolution on absorption across the AGS hollow fiber membrane. A concurrent study with a non-sink dissolution-only 'control' is also conducted to understand the impact of absorption on drug dissolution and amorphous and crystalline precipitation.

4.3 Materials and Methods

4.3.1 Materials

KTZ drug (Laborate Pharmaceuticals, Haryana, India) and HPMCAS polymer (HF grade, Ashland Global Specialty Chemicals Inc., DE) were pre-dried overnight at 80℃ to remove residual moisture before use. Hydrochloric acid (36.5-38.0%), methanol, concentrated sulfuric acid, benzene and phenol were purchased from Sigma-Aldrich Co., MO and were used as received.

Fasted-state simulated intestinal fluid is typically prepared by dissolving FaSSIF-V2 powder (Biorelevant.com Ltd., London, UK) containing bile salts and lecithin at a quantity prescribed by the manufacturer into pH 6.5 maleate buffer. However, maleic acid in biorelevant media can result in difficulties during low wavelength UV quantification of drug substances such as KTZ whose wavelength of maximum absorbance is 225 nm.[38,132] This is not a problem with phosphate buffer due to lack of observable UV absorbance of phosphate ion around the wavelength of interest. [38,132] Therefore, in this study, 31.8 mM phosphate buffer of matching pH, osmolality and buffer capacity as maleate buffer was prepared using monobasic sodium phosphate monohydrate, dibasic sodium phosphate heptahydrate and sodium chloride purchased from Sigma-Aldrich Co. (***Table 4.1***).[38,132,133] The measured crystalline and amorphous solubilities of KTZ were the same in both the media. The modified FaSSIF-V2 media was used as a drug 'donor' media in this study. pH 6.5 phosphate buffer, without the bile salts and lecithin used for modified FaSSIF-V2 preparation, was used as a 'receiver' media pumped continuously through the intraluminal space of the hollow fibers.

Table 4.1. Composition of original and modified FaSSIF-V2 media.

Component	Conc. in FaSSIF-V2 (mM)	Conc. in FaSSIF-V2 (modified) (mM)	Purpose
Sodium Taurocholate	3	3	Natural Bile Salt
Lecithin	0.2	0.2	Natural Surfactant
Sodium Chloride	68.6	68.6	Adjusts osmolarity
Sodium Dihydrogen Phosphate	-	31.8	Buffer
Maleic Acid	19.1	-	Buffer
Sodium Hydroxide	34.8	-	Adjusts pH

Property	FaSSIF-V2	FaSSIF-V2 (modified)
pH	6.5	6.5
Osmolarity (mOsm/L)/a_w	180/0.996	180/0.996
Buffer Capacity (mM/pH)	10	10

The AGS was constructed as outlined in Chapters 2 and 3 with slight modification. Briefly, hollow fibers supported on a laser-cut plexiglass support framework were potted into inlet and outlet tubes for intraluminal/receiver media emerging from cuvette cap (Azzota Scientific, DE) using a silicone UV-cure glue (Henkel Corporation, OH). In this study, however, modified polyether sulfone (mPES) hollow fibers were replaced with 13 kDa MWCO regenerated cellulose-based hollow fibers (Spectra/Por® *In Vivo* Microdialysis Hollow Fibers, Repligen Corporation, CA) of d=200 µm and L=5 cm. The cellulose hollow fibers had more neutral surface preventing drug adsorption to the membrane and much thinner walls (40 µm, compared to 125 µm of mPES hollow fiber) allowing for significantly faster steady-state attainment of luminal drug concentration.

4.3.2 Crystalline and Amorphous Solubility Determination of KTZ in FaSSIF-V2 media

Crystalline and amorphous solubilities of KTZ were determined in pH 6.5 FaSSIF-V2 media without and with pre-dissolved HPMCAS polymer at concentrations ranging from 0.5 to 4.0 mg/mL at 37℃. Solubility determinations were made using the method described earlier.[102] Briefly, for amorphous solubility measurement, concentrated KTZ stock solution (6 mg/mL) in pH 1.5 HCl was titrated into 3 mL FaSSIF-V2 media contained in a quartz cuvette at a rate of 10 µL/min under constant stirring. Light scattering or extinction was measured by UV spectroscopy (Cary 100 Bio, Agilent Technologies, Inc., CA, path length 10 mm) at a non-absorbing wavelength of 340 nm. An abrupt increase in extinction indicated the appearance of LLPS and the corresponding concentration was taken to be the amorphous solubility concentration. Crystalline solubility was determined by equilibrating excess solid KTZ in FaSSIF-V2 media for 48 hours followed by separation of undissolved solids by centrifugation (Marathon 26KMR microcentrifuge, Thermo Fisher Scientific Inc., MA) and determination of drug concentration in the supernatant.

Additionally, the effect of increasing HPMCAS concentration in FaSSIF-V2 media on concentration, size and zeta potential of amorphous nanodroplets was evaluated using nanoparticle tracking analysis (NTA, NanoSight LM-10, Malvern Instruments, MA) and a zeta potential analyzer (Stabino, Particle Metrix GmbH, Inning am Ammersee, Germany), respectively. Briefly, KTZ at a concentration of 290 µg/mL (above its amorphous solubility) was introduced in media containing 0 – 1.5 mg/mL pre-dissolved HPMCAS. A 400 nm laser light source was directed towards KTZ nanodroplets dispersed in the media which filled an NTA sample cell mounted on the stage of a microscope. These particles undergoing Brownian motion, with the smaller particles moving more quickly than the

larger ones, scattered a small amount of light out through an optical window where it was collected by a 20x magnification microscope objective. NanoSight software determined the diffusion coefficient of the particles based on the recorded particle Brownian motion, and then the hydrodynamic diameter using the Stokes-Einstein relation.

4.3.3 Preparation of ASDs by Rotary Evaporation

KTZ and HPMCAS polymer ASDs were prepared at 1:9, 2:8 and 3:7 weight ratios. An appropriate quantity of drug and polymer powders was dissolved in methanol by heating at 50℃ for 20 minutes in a water bath. Solvent was removed using a rotary evaporator (IKA-HB10 digital system rotary evaporator, Werke. GmbH and Co., Staufen, Germany) at 50℃ under reduced pressure (25 mm of Hg). The solid dispersions were further dried at room temperature for 24 hours in a vacuum desiccator. The dried ASDs were cryomilled (Model 6750 Freeze Mill, Spex SamplePrep, NJ) in a cylindrical polycarbonate vial (SPEX SamplePrep #6751 vials) equipped with a stainless-steel impactor and submerged in liquid nitrogen throughout the milling process. Not more than 1 g of the sample was loaded at a time, pre-cooled in liquid nitrogen for 10 minutes following which the samples were milled for 30 seconds at a constant milling rate of "10" (i.e. 20 impacts/second) per cycle and five such cycles were performed. Samples were then equilibrated to room temperature in a desiccator and then stored at -20℃ until further use.

Differential Scanning Calorimetry (DSC) was performed to confirm the amorphous nature of the prepared dispersions. Briefly, a differential scanning calorimeter (TA instruments Q2000, Delaware, USA) equipped with a refrigerated cooling unit was used. The instrument was calibrated with indium. To make measurements, 1-4 mg of sample was hermetically sealed in an aluminum pan. All measurements were carried out under dry

nitrogen purge (50 mL/min). The melting point and glass transition temperature were determined by heating the sample at a rate of 10℃/min to 100℃, rapidly cooling to 0℃ followed by reheating at a rate of 10℃/min to 200℃. DSC data was analyzed using Universal Analysis software.

4.3.4 Simultaneous Dissolution and Absorption Testing Study with AGS

The AGS, consisting of a cellulose hollow fiber-based absorption module suspended in a 'donor' UV spectrophotometric quartz cuvette, was used to assess the performance of ASDs. First, the operating parameters were tuned to absorb KTZ at a physiological rate constant, k_{a} = 0.013 min^{-1}.[134] The simulated absorption rate constant $k_{\mathrm{a,AGS}}$

$$k_{\mathrm{a,AGS}} = \left(\frac{Q}{V}\right)\left(1 - e^{-\frac{NPA_{\mathrm{IL}}}{Q}}\right) \tag{4.1}$$

was matched to the target k_{a} by selecting *N*, number of hollow fibers and *Q*, the hollow fiber intraluminal fluid flow rate (Chapters 2 and 3). Donor volume, *V* and lateral surface area of each hollow fiber, A_{IL} were set at 1.8 mL and 0.32 cm^2, respectively. The permeability coefficient of KTZ, *P*, across the cellulose hollow fiber membrane was determined to be (1.05 ± 0.07) x 10^{-4} cm/s using a method described earlier (Chapters 2 and 3). To verify that the AGS was tuned to absorb at $k_{\mathrm{a,AGS}}$, a mass transport study was conducted at 37℃ from an initially saturated solution of KTZ in FaSSIF-V2 media into intraluminal phosphate buffer pumped at the selected flow rate using a syringe pump. An estimate of $k_{\mathrm{a,AGS}}$ was obtained by fitting the extraluminal concentration-time profile $C_{\mathrm{EL}}(t)$ to Eq. (4.2) (Chapters 2 and 3).

$$C_{\mathrm{EL}}(t) = C_{\mathrm{EL}}(0)e^{-k_{\mathrm{a,AGS}}t} \tag{4.2}$$

The tuned AGS was then used to conduct mass transport studies from supersaturated solution of KTZ generated in the donor upon ASD dissolution at 37℃. The three ASDs – 1:9, 2:8 and 3:7 KTZ:HPMCAS – were weighed into a home-made dissolution sample holder (with an attached magnetic stir bar that also functioned as a sinker) to dose KTZ at 90, 120, 180, 240, 300 and 400 µg per mL of FaSSIF-V2 media in the donor. Hollow fiber intraluminal fluid flow was initiated, and the absorption module was inserted into the donor cuvette immediately upon the introduction of sample holder containing the ASD powder. Multi-cell UV spectrophotometer equipped with magnetic stirring was used to conduct wavelength scans from 340 to 200 nm every minute for 120 min at the rate of 465 nm/min, alternating between drug donor cuvette and a flow through cell to measure KTZ concentration in the intraluminal fluid exiting the absorption module. The intraluminally absorbed KTZ concentration was determined from UV absorbance profiles at 225 nm and donor concentrations were determined by second derivative spectroscopy, also at 225 nm. Additionally, a non-sink dissolution study was conducted as a 'control' by suspending hollow fibers devoid of any intraluminal fluid into the drug donor cuvette. All measurements were carried out in duplicate.

4.3.5 Effect of KTZ solution-state activity on absorption

The amount of KTZ absorbed is directly related to its activity in solution or, in other words, the concentration of 'free' drug available for diffusion across the hollow fiber membrane.[22] To evaluate the effect of polymer on KTZ solution-state activity, KTZ absorption from saturated drug solutions prepared in FaSSIF-V2 media containing 0-4 mg/mL pre-dissolved HPMCAS polymer was determined. Initially saturated solutions were added to the donor (cuvette) and the tuned AGS absorption module was placed in the

donor. The concentration of drug absorbed by the intraluminal fluid was below the limit of quantification and could not be reliably measured. The donor drug concentration was measured by UV spectroscopy every minute for 60 min and the amount depleted from the donor was taken to be the amount absorbed. To evaluate reduction in the fraction of free drug with increasing concentration of polymer dissolved, KTZ fraction depleted in the donor with pre-dissolved polymer was normalized by the fraction depleted in the absence of polymer.

4.3.6 Effect of absorption on drug and polymer release kinetics

The effect of absorption on KTZ and HPMCAS release kinetics was evaluated by measuring their concentration released into both the non-sink 'control' and AGS donor media from 1:9, 2:8 and 3:7 KTZ:HPMCAS ASDs. Only one dose concentration of KTZ, 90 µg/mL, was evaluated since minimal precipitation can be expected in this case. Briefly, non-sink 'control' and mass transportation runs with the tuned AGS were conducted for 5, 15, 30, 45 and 60 minutes. At the end of each time point, the non-sink 'control' and AGS donor media in entirety was subjected to centrifugation at 14,800 rpm (Marathon 26KMR microcentrifuge, Thermo Fischer Scientific Inc., MA) for 10 minutes followed by filtration of the resultant supernatant through a pre-saturated 0.2 micron nylon filter (VWR Technology, PA) to get rid of undissolved drug and precipitate, if any. The concentration of KTZ in the filtered supernatant were measured by UV spectroscopy at 225 nm. The concentration of HPMCAS was determined using a colorimetric method by DuBois et al.[136] 10 µL of the filtered supernatant was diluted to 1 mL with distilled water and was treated with 25 µL of 80% w/w phenol solution and 2.5 mL concentrated sulfuric acid. The solution was vortexed and stored for 12 hours. The solution developed an orange-colored

conjugated complex and the polymer concentration was determined by visible spectroscopy at 490 nm. The calibration curve for polymer concentration was prepared with reference solutions containing 0.01 to 4 mg/mL HPMCAS polymer.

In case of the mass transport study with AGS, the concentration of drug absorbed by the receiver fluid was also simultaneously measured every minute, also by UV spectroscopy at 225 nm. All measurements were made in duplicate and expressed as percentage of drug or polymer released calculated as per Eqs. (4.3) – (4.6).

$$\%\ \text{polymer released} = \frac{\text{Conc. of polymer measured in the dissolution media} \times V_{EL} \times 100}{\text{Total polymer amount in ASD}} \tag{4.3}$$

$$\%\ \text{drug released in 'control'} = \frac{\text{Conc. of drug measured in the dissolution media} \times V_{EL} \times 100}{\text{Total drug amount in ASD}} \tag{4.4}$$

where

$$\%\ \text{drug released in AGS donor} = \frac{[(\text{Conc. of drug measured in the dissolution media} \times V_{EL}) + \text{Cumulative KTZ amount absorbed}] \times 100}{\text{Total drug amount in ASD}} \tag{4.5}$$

$$\text{Cumulative KTZ amount absorbed(t)} = \text{AUC}_{IL,0-t} \times Q \tag{4.6}$$

and $\text{AUC}_{IL,0-t}$ is the area under the receiver concentration-time curve and in this experiment, t = 60 min.

4.3.7 Effect of absorption on crystalline and amorphous precipitation

Mass balance was used to quantitate precipitation in both the non-sink 'control' and the AGS donor at the end of 120 minutes of dissolution and mass transport runs conducted above (*Section 4.3.4*).

Non-sink 'control':

$$\text{Total precipitate (fraction of dose)} = \frac{\text{Dose concentration} - \text{Concentration of drug remaining in dissolution media}}{\text{Dose concentration}} \tag{4.7}$$

AGS Donor:

$$\text{Total precipitate (fraction of dose)} = \frac{\text{Dose concentration} - \text{Concentration of drug remaining in dissolution media} - \frac{\text{KTZ amount absorbed}}{V_{EL}}}{\text{Dose concentration}} \quad (4.8)$$

Amount of drug absorbed at the end of 120 minutes from the AGS donor can be determined from the AUC of receiver concentration-time profiles using Eq (4.6) at t=120 min.

Concentration of drug remaining in the donor at 120 minutes may not be reliably determined by direct UV absorbance measurement since the precipitate particles may also absorb UV radiation, thereby overestimating drug concentration.[43] KTZ 'control' and AGS donor solutions were collected at the end of 120 min and subjected to ultracentrifugation at 35,000 rpm for 15 minutes in an Optima L-100 XP ultracentrifuge with swinging-bucket rotor SW 41 Ti (Beckman Coulter Inc., CA). KTZ concentration in the supernatant devoid of precipitate was determined by UV spectroscopy at 225 nm. Using these estimates of drug concentration remaining in the dissolution media, total precipitate fractions were calculated using Eqs. (4.7) and (4.8).

Total precipitate consists of both amorphous and crystalline drug species. Fluorescent probes have been utilized elsewhere to detect LLPS and quantify amorphous precipitate in supersaturated drug solutions as they exhibit a large hypsochromic shift and increase in peak intensity with decreasing environmental polarity upon LLPS.[22,42] In the present case, KTZ is auto-fluorescent and was used in lieu of an additional probe.

Fourteen reference solutions of KTZ (concentration ranging from 25 to 616 µg/mL) were prepared in FaSSIF-V2 media by the pH-shift method (described in detail in Chapter 3). Fluorescence emission spectra from 341 to 450 nm were recorded using a Cary Eclipse fluorescence spectrometer (Agilent, CA) at an excitation wavelength of 340 nm, with a sampling interval of 1 nm, scan rate of 600 nm/min and excitation and emission slit width of 5 nm. Below the amorphous solubility concentration, KTZ showed emission maxima at 380 nm which reduced to 353 nm upon LLPS above amorphous solubility (**Appendix, *Figure A4a,b***). This is similar to hypsochromic shift seen in KTZ emission spectra as the media in which KTZ is dissolved is changed from relatively polar ethanol to non-polar benzene (**Appendix, *Figure A4c,d***). LLPS is also marked by an abrupt increase in intensity at the amorphous solubility concentration (**Appendix, *Figure A4b***). To develop a calibration curve for the determination of KTZ amorphous precipitate amount in dissolution media at the end of 120 minutes of dissolution and mass transport runs, fluorescence emission intensity at 353 nm of reference solutions above amorphous solubility concentration was plotted as a function of amount of amorphous precipitate present in solution calculated by mass balance Eq. (4.9).

$$\text{Amount of amorphous precipitate per mL} = \text{Total KTZ concentration} - \text{Amorphous solubility} \quad (4.9)$$

Validity of the mass balance method to determine the amount of KTZ amorphous precipitate formed was verified by ultracentrifugation.[22] KTZ supersaturated solutions of concentration ranging from 350 to 620 µg/mL were generated in ultracentrifugation tubes by the pH-shift method and immediately subjected to ultracentrifugation. KTZ precipitate pellet collected at the bottom of the tube was amorphous as confirmed by the observation of a single T_g in a DSC thermogram at 7℃ (here, the T_g of amorphous KTZ with about 4%

w/w of absorbed moisture, determined by Karl Fischer titration, was lower than anhydrous amorphous KTZ T_g of 44℃ [138]). The supernatant was discarded, and the precipitate was dried for 2 days at 30 mmHg in a vacuum oven at room temperature. The mass of the dried precipitate was determined using a microbalance.

The calibration curve was utilized to determine the mass of amorphous precipitate present in dissolution media from its fluorescence intensity at 353 nm before it was ultracentrifuged. If an emission maximum at 353 nm was absent, the amount of amorphous precipitate in the dissolution media was considered nil. Crystalline precipitate was determined by mass balance as,

$$\text{Crystalline precipitate (fraction of dose)} = \text{Total precipiate (fraction of dose)} - \frac{\text{Amorphous precipitate (µg per mL)}}{\text{Dose concentration}} \quad (4.10)$$

All experiments were performed in duplicate.

4.3.8 Effect of absorption and polymer concentration on KTZ amorphous precipitate nanodroplets

NTA was used to track the number density and diameter of KTZ amorphous precipitate nanodroplets as a function of time and in the presence of varying concentrations of pre-dissolved HPMCAS polymer. The pH shift method was used to generate 300 µg/mL of KTZ supersaturated solution in FaSSIF-V2 media containing 0, 0.5, 1 and 1.5 mg/mL pre-dissolved HPMCAS solution in non-sink 'control' and tuned AGS donor. Each run was conducted separately for 0, 5, 10 and 15 minutes. At the end of each time point, dissolution

media was introduced into the optical window of the NTA microscope where size and number density measurements of amorphous nanodroplets were made. Here, pH-shift method of supersaturation generation was utilized instead of ASD dissolution due to non-discrimination between small ASD particles from amorphous precipitate nanodroplets under the microscope even after the dissolution media was filtered through a 1 µm glass filter.

4.4 Results

4.4.1 Crystalline and Amorphous Solubility Determination

The crystalline and amorphous solubilities (determined by UV extinction method, **Appendix, *Figure A1***) of KTZ at 37℃ without and with increasing dissolved concentrations of HPMCAS polymer are tabulated in ***Table 4.2***.

Table 4.2. Crystalline and amorphous solubility of KTZ in FaSSIF-V2 media containing increasing dissolved HPMCAS polymer concentration.

Media	Crystalline Solubility (µg/mL)	Amorphous Solubility (µg/mL)
FaSSIF-V2	21.1 ± 1.4	234.5 ± 3.5
FaSSIF-V2 w/ 0.5 mg/mL HPMCAS	22.2 ± 0.3	243.7 ± 4.6
FaSSIF-V2 w/ 1 mg/mL HPMCAS	23.9 ± 0.5	258.3 ± 3.4
FaSSIF-V2 w/ 1.5 mg/mL HPMCAS	26.2 ± 0.8	277.7 ± 3.4
FaSSIF-V2 w/ 2 mg/mL HPMCAS	27.8 ± 0.2	293.0 ± 2.8
FaSSIF-V2 w/ 3 mg/mL HPMCAS	28.3 ± 0.4	305.5 ± 6.4
FaSSIF-V2 w/ 4 mg/mL HPMCAS	32.1 ± 1.1	317.8 ± 3.4

A significant increase in the concentration of KTZ solubilized by bile micelles in FaSSIF-V2 media relative to phosphate buffer alone is observed (Chapter 3). Moreover, increasing HPMCAS concentration leads to both crystalline and amorphous solubility enhancement of KTZ. Amorphous solubility represents the concentration that marks the formation of drug-rich colloidal nanodroplets dispersed in the bulk aqueous phase that can scatter light and increase the UV extinction measured at a non-absorbing wavelength. With increasing concentration of pre-dissolved HPMCAS, a greater concentration of KTZ had to be added to FaSSIF-V2 before an abrupt increase in extinction was observed (**Appendix, *Figure A1***). Moreover, increasing concentration of the polymer led to a decline in the extent to which the extinction increased after LLPS onset. This is in line with the NTA observations (***Figure 4.2***) wherein the number density of smaller amorphous nanodroplets increased with simultaneous increase in negative zeta potential as polymer concentration increased, indicating greater surface stabilization of the nanodroplets against coalescence with increasing HPMCAS concentration.

HPMCAS is an amphiphilic polymer with the carbonyl functional group of the polymer interacting with the drug's imidazole group in aqueous phase via dipole-induced dipole and hydrogen bonding interactions whereas the hydrophobic acetyl group is distributed into the drug-rich amorphous phase.[139–141] However, it was previously shown that pre-dissolved HPMCAS polymer decreased the amorphous solubility of KTZ even though it increased its crystalline solubility.[139] Increase in crystalline solubility is indicative of significant interactions between the drug and polymer in the aqueous phase. The discrepancy in amorphous solubility trends between the previous and current study may have arisen due to the differences in pH at which the solubility measurements were made

as pH is known to greatly influence the ionization characteristics of both the drug and polymer and subsequently their interactions.[141–143] The current study was conducted at pH 6.5 while the earlier study was conducted at pH 8.0. Decline in amorphous solubility with increasing additive concentration suggests substantial distribution of the additive into the drug-rich phase at LLPS onset resulting in lower drug concentration dissolved in the bulk water phase.[144] In this study, however, an increase in drug amorphous solubility with increasing HPMCAS concentration indicates an increasing proportion of the polymer in bulk aqueous phase undergoing hydrophilic interactions with the drug at pH 6.5 where more KTZ imidazole groups (pKa 6.5[145]) are ionized compared to pH 8.0. A higher degree of drug-polymer interactions in the aqueous phase may reduce the partitioning of the polymer into the drug-rich amorphous phase at pH 6.5 relative to pH 8.0. This solubilizing effect of the polymer additive is indicative of a reduction in the thermodynamic activity of the dissolved drug.[146]

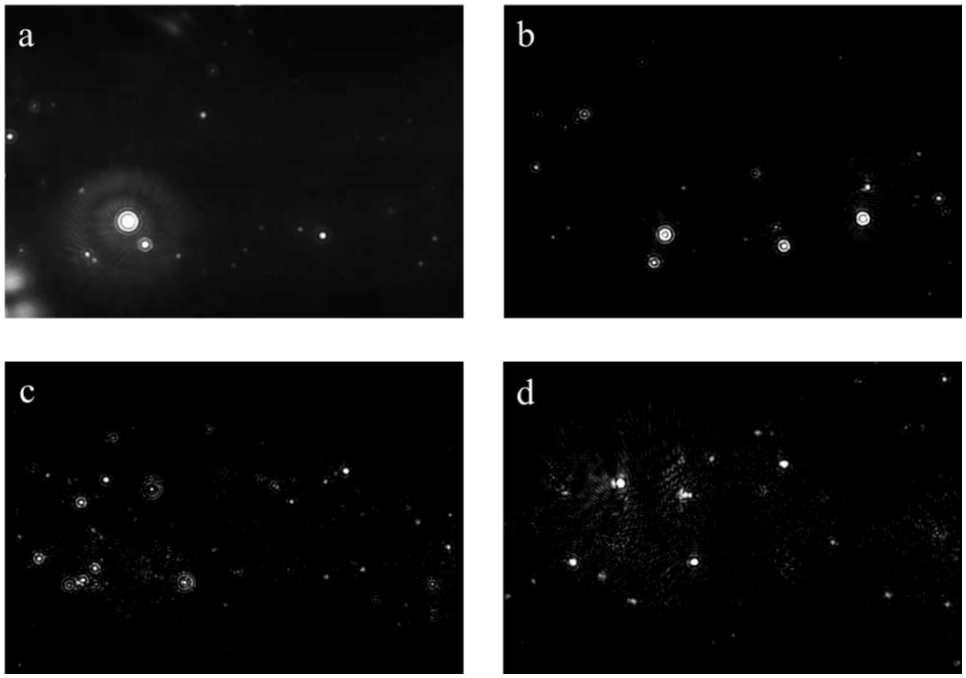

(e)

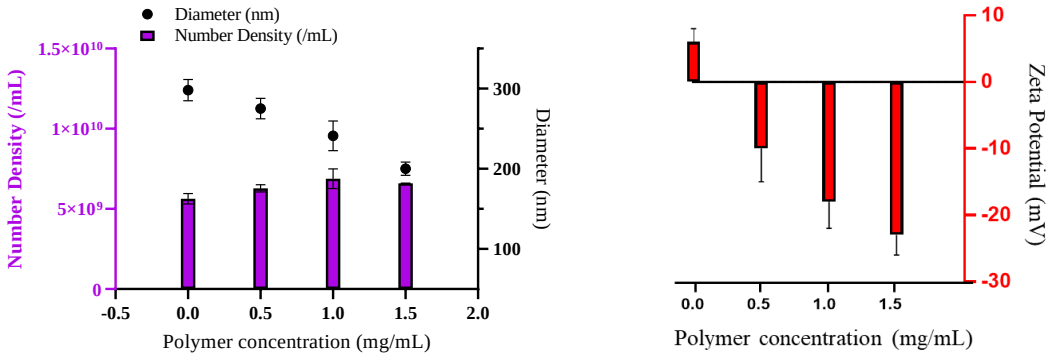

Figure 4.2. NTA micrographs of 290 µg/mL KTZ in FaSSIF-V2 media containing **(a)** 0, **(b)** 0.5, **(c)** 1, and **(d)** 1.5 mg/mL dissolved HPMCAS. **(e)** Change in number density, diameter and zeta potential of KTZ amorphous nanodroplets as a function of increasing polymer concentration.

4.4.2 Preparation of ASDs by Rotary Evaporation

ASD fine powder samples were prepared with a single glass transition temperature (T_g) occurring between that of pure KTZ (44℃ [138]) and pure HPMCAS (139℃) (**Appendix, *Figure A2***). The T_g of the ASDs increased with increasing polymer loading indicating better stabilization by the polymer.

4.4.3 Simultaneous Dissolution and Absorption Testing Study with AGS

Eq. (4.1) was used to map $k_{\mathrm{a,AGS}}$ as a function of hollow fiber surface area for absorption ($N \times A_{IL}$) and receiver fluid flow rate Q (**Appendix, *Figure A3a***). The value of $k_{\mathrm{a,AGS}}$ of KTZ increases with $N \times A_{\mathrm{IL}}$ and Q. At high values of Q, however, absorption becomes permeation limited (Chapter 2).

The physiological absorption rate constant of KTZ is k_{a}= 0.013 min^{-1}.[134] Upon setting the intraluminal fluid flow rate at Q = 500 µL/min and the number of hollow fibers at N=12, this rate constant ($k_{\mathrm{a,AGS}}$) is attained (red star in **Appendix, *Figure A3a***). ***Figure A3b*** in the **Appendix** displays a run of the AGS with these parameters, starting with a saturated solution of KTZ in the donor. The parameter $k_{\mathrm{a,AGS}}$ was estimated by fitting the experimental fraction absorbed-time profile to Eq. (4.2) (black line in **Appendix, *Figure S3b***) and was found to be 0.0130 ± 0.0001 min^{-1} which is the same as the physiological k_{a} for KTZ.[134]

Figure 4.3 shows KTZ receiver and donor concentration-time profiles measured during the simultaneous ASD dissolution and absorption study as well as 'control' non-sink dissolution-time profiles, for dose concentrations added below (90, 120, 180 µg/mL), at (240 µg/mL) and above (300 and 400 µg/mL) the amorphous solubility concentration of

KTZ in FaSSIF-V2 media. Drug concentrations measured by in-line UV spectroscopy in the AGS donor and non-sink 'controls' are not quantitative since it has been demonstrated earlier that precipitated nanoparticles can both absorb and scatter light.[43] Hence, concentrations may be over-predicted especially at later time points as precipitation increases.

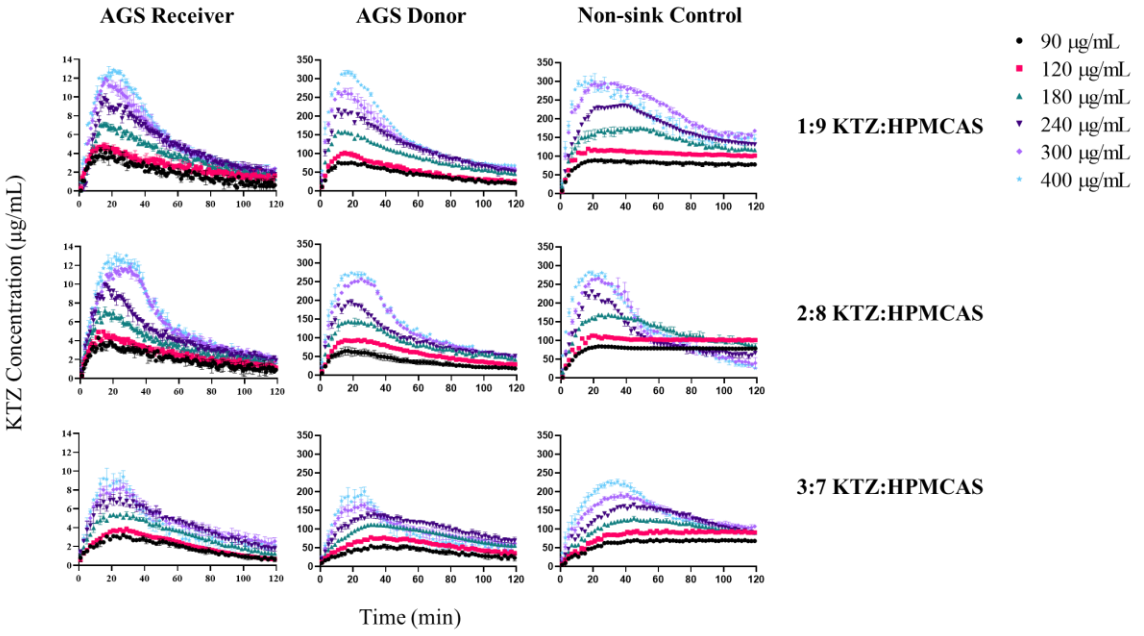

Figure 4.3. KTZ concentration-time profiles in non-sink 'controls' and AGS receiver and donor obtained upon dissolution of 1:9, 2:8 and 3:7 KTZ:HPMCAS ASDs at 90 to 400 µg/mL dose concentrations.

In all the cases, the receiver concentration initially increases before attaining a maximum concentration (C_{max}). The thin cellulose hollow fiber membrane used in this study allows rapid attainment of steady state in the intraluminal fluid. Immediate generation of 120 µg/mL dose concentration in the donor containing 0.48 mg/mL HPMCAS dissolved in FaSSIF-V2 media by addition of appropriate volume of concentrated acidic stock solution of KTZ (pH-shift method) resulted in a lag time of 4

minutes to attain C_{max} in the intraluminal fluid which is significantly lesser than a lag time of 15 minutes seen upon 2:8 KTZ:HPMCAS ASD dissolution in the donor to generate the same dose concentration (***Figure 4.4a***). Thus, the delay in attaining C_{max} here represents ASD dissolution time lag in the donor rather than hollow fiber membrane diffusion time lag as seen with mPES hollow fiber membrane in an earlier study with KTZ (Chapter 3). Lag times to attain C_{max} in the donor and receiver profiles of the AGS as well as in non-sink dissolution 'controls' are similar for a particular ASD which also demonstrates that the delay can be attributed to ASD dissolution.

After C_{max}, drug concentration in non-sink dissolution 'controls' plateaus and then decreases due to precipitation, the rate of decline increasing with increasing dose concentration. For 1:9 and 2:8 KTZ:HPMCAS ASDs at sub-amorphous solubility dose concentrations, the plateau occurs at the dose concentration itself. For dose concentrations exceeding the amorphous solubility, plateau occurs at the amorphous solubility concentration which represents the miscibility limit of KTZ in FaSSIF-V2 in the presence of HPMCAS. Since, at higher dose concentrations, HPMCAS concentration released into the media increases, the amorphous solubility and subsequently, the plateau concentration also increases. Also, due to higher HPMCAS loading in 1:9 KTZ:HPMCAS ASD and its subsequent release into the media, the rate of decline in drug concentration due to crystallization is lower at all dose concentrations relative to 2:8 KTZ:HPMCAS ASD. Dissolution rate (slope of the initial linear portions of dissolution-time profiles) increases with increasing dose concentration but decreases as drug loading in the ASD increases due to increasing hydrophobicity (***Figure 4.4b***). This was also observed in an earlier study[117] and will be discussed in more detail in subsequent sections. For 3:7 KTZ:HPMCAS ASD,

the concentration of KTZ upon release plateaus at a concentration significantly lower than the dose concentration and amorphous solubility in all the cases before it starts declining due to precipitation.

In the AGS donor, concentration increases initially as the ASD dissolves, attains C_{max} and then decreases due to both absorption and precipitation. This is reflected in the receiver as well. In the AGS donor and receiver, C_{max} increases with increasing dose concentration. However, compared to the non-sink 'control', a lower C_{max} is attained at sub-amorphous solubility dose concentrations in the AGS donor due to simultaneous drug absorption (***Figure 4.4c***). Moreover, similar to the non-sink 'control', we observe a lower C_{max} in the AGS donor as polymer loading in the ASD decreases. Due to slow dissolution and simultaneous absorption, C_{max} in both the donor and receiver is significantly lower at all dose concentrations with 3:7 KTZ:HPMCAS ASD compared to the ASDs with higher HPMCAS loading. C_{max} was also found to be significantly higher at higher dose concentrations of 1:9 KTZ:HPMCAS ASD compared to 2:8 KTZ:HPMCAS ASD due to amorphous solubility limitation on dissolution in case of the latter. However, unlike in the donor, similar C_{max} was observed at all dose concentrations in the receiver with the two ASDs. This may be due to a relative reduction in free KTZ fraction available for absorption in the presence of higher concentration of dissolved polymer. This hypothesis is evaluated in the next section.

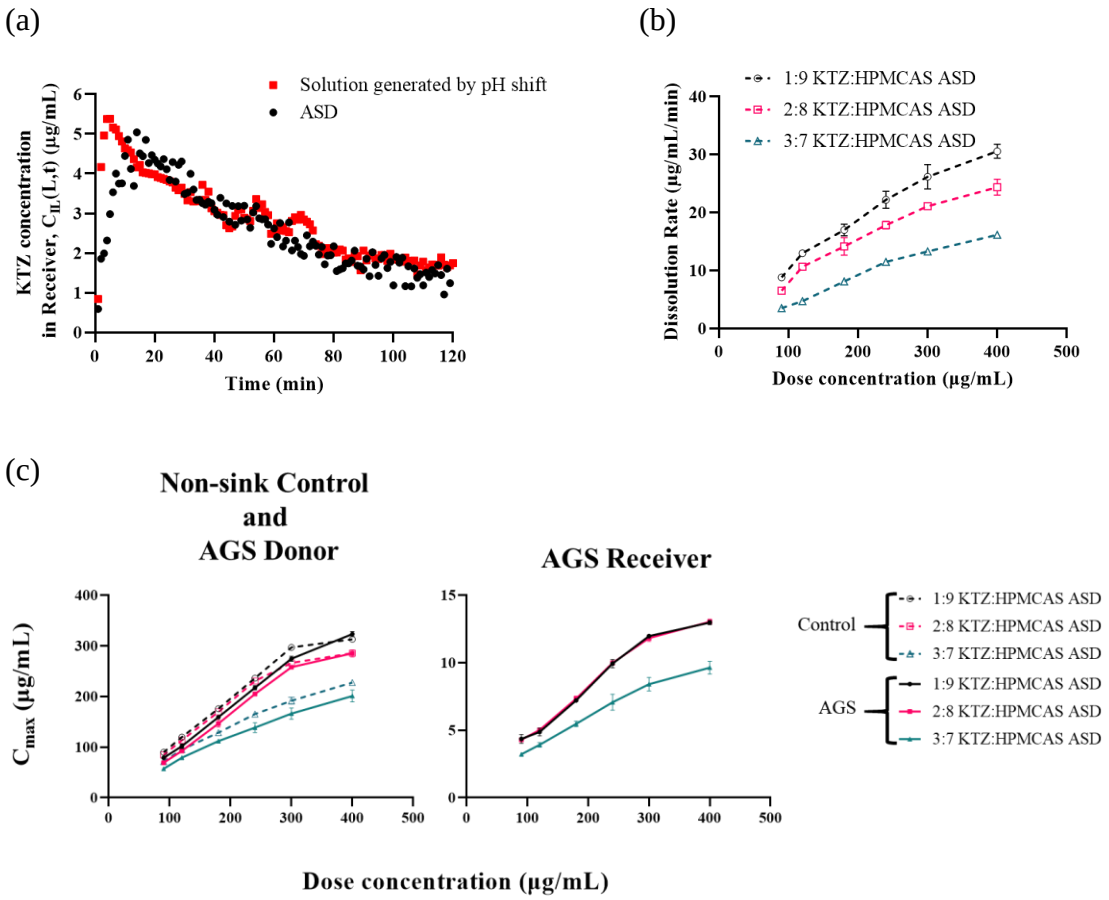

Figure 4.4. (a) Comparison of receiver concentration-time profiles obtained when 120 µg/mL dose concentration was generated in the AGS donor by pH-shift method and ASD dissolution. **(b)** Dissolution rates of 1:9, 2:8 and 3:7 KTZ:HPMCAS ASDs in non-sink 'control' as a function of dose concentrations. **(c)** C_{max} as a function of dose concentration obtained in non-sink 'control' as well as AGS donor and receiver upon dissolution of 1:9, 2:8 and 3:7 KTZ:HPMCAS ASDs.

4.4.4 Effect of KTZ solution-state activity on absorption

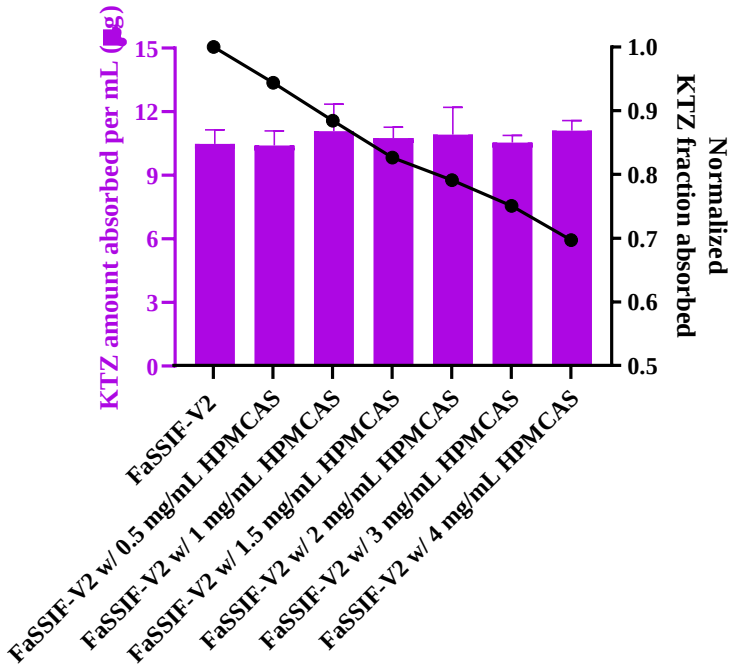

Figure 4.5. KTZ amount (left Y-axis) and fraction absorbed normalized by the fraction absorbed from FaSSIF-V2 without any polymer (right Y-axis) plotted as a function of increasing polymer concentration. Initial KTZ concentration in the donor was at crystalline solubility.

To explain the discrepancy between the donor and receiver C_{max} trends, we sought to decouple the effect of polymer-bound drug species on absorption from the other co-occurring phenomenon of precipitation by using donor solutions containing KTZ at its initial crystalline solubility concentration. Solution-state activity of KTZ in the presence of increasing concentration of pre-dissolved HPMCAS polymer was evaluated indirectly by measuring the amount of drug depleted from the donor. From ***Table 4.2*** it is clear that as HPMCAS concentration increases, the crystalline solubility of KTZ also increases. However, at the end of 60 minutes, the amount of KTZ absorbed, i.e. KTZ solution-state activity is the same, regardless of the increasing initial donor drug concentration with

increasing polymer concentration (***left Y-axis of Figure 4.5***). This is similar to what was observed in the AGS study with ASDs above, wherein a higher C_{max} in the AGS donor upon dissolution of an ASD of higher polymer loading did not result in a proportionately higher C_{max} in the receiver. The fraction of KTZ absorbed in the presence of polymer was normalized by that absorbed from FaSSIF-V2 media alone and was plotted as a function of polymer concentration (***right Y-axis of Figure 4.5***). The normalized fraction absorbed decreases with increasing polymer concentration indicating declining absorption efficacy, i.e. the addition of solubilizing agents to a formulation to increase apparent dissolved concentration of KTZ will not necessarily guarantee a proportional increase in its flux across a membrane. This has been demonstrated several times in *ex vivo* and *in vivo* membrane permeation/absorption assays of drugs in the presence of solubilizing agents. For instance, a decrease in permeability of another poorly soluble compound, piperine in the presence of HPMCAS polymer, was shown via rat intestinal perfusion assay inspite of an increase in the drug's solubility and was attributed to a reduction in drug's free fraction available for absorption.[119] This reduction in free fraction of the drug and absorption rate across rat intestinal membrane was also observed with KTZ in the presence of solubilizing bile micelles.[8] It has also been demonstrated earlier how an increase in free fraction of drug fenofibrate in solution with changing ASD compositions translates directly to a higher fraction of drug absorbed *in vivo* in beagle dogs.[118] Negative Flory-Huggins interaction parameter, i.e. favorable interactions between KTZ and HPMCAS[140] in this case possibly reduces the free drug fraction available for absorption.

4.4.5 Effect of absorption on drug and polymer release kinetics

Figure 4.6 shows the cumulative percentage of drug and polymer released into the dissolution media of non-sink 'control' and AGS Donor [Eqs. (4.3)-(4.6)]. As discussed earlier, it is clear that as the hydrophobic drug KTZ loading in ASD increases, the rate of dissolution decreases. By 15 minutes, the drug released in the AGS donor was about 7-10% higher than that released in the non-sink 'control', which can be attributed to depletion of drug by absorption that draws more drug out from the ASD formulation. In the case of 1:9 and 2:8 KTZ:HPMCAS ASDs, drug and polymer release in both the 'control' and AGS donor is congruent throughout and nearly complete in 30 minutes. In case of 3:7 KTZ:HPMCAS ASD, drug and polymer release is congruent until 15 minutes in the 'control' and 30 minutes in the AGS Donor. This switch from rapid, congruent to slower, incongruent release of drug and polymer at specific drug loading in ASD was also observed in an earlier study and attributed to competitive kinetics between phase separation in the ASD and release of drug and polymer.[147] Although incongruent, the percent drug released in AGS donor is greater than that observed in the 'control. It may be hypothesized that a higher percentage of drug release from the ASD due to a larger concentration gradient created by absorption results in a reduced concentration of drug remaining in the ASD which in turn reduces the driving force for phase separation in the ASD. Observation of incongruence in drug and polymer release at a later time point and higher percentage of drug released in the AGS donor are indicative of longer induction time for phase separation in the ASD and possibly at a slower rate relative to the 'control'.

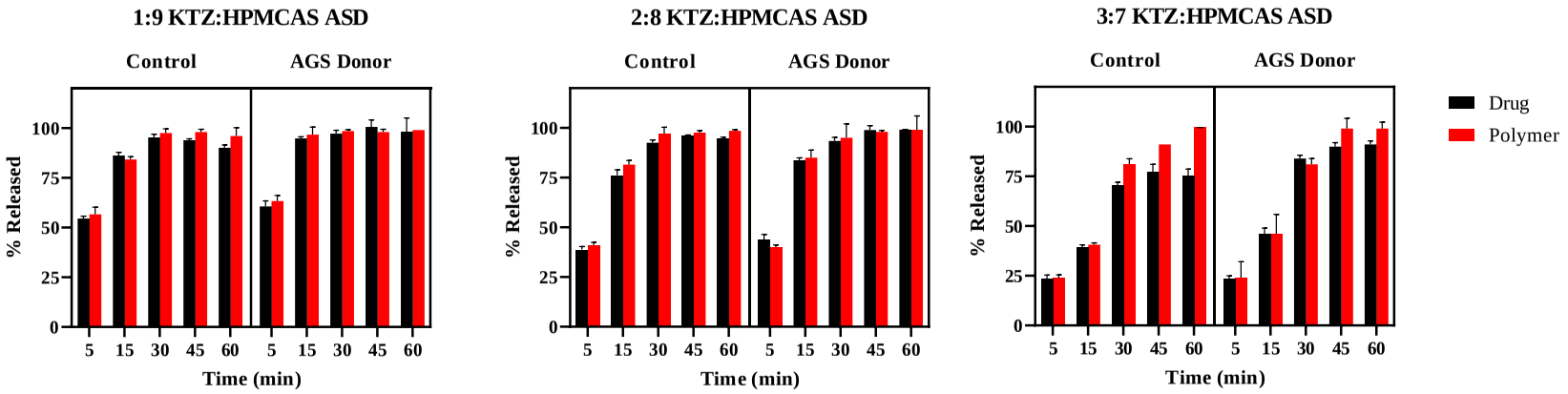

Figure 4.6. Cumulative percentage of 90 µg/mL dose concentration of KTZ and HPMCAS polymer released from 1:9, 2:8 and 3:7 KTZ:HPMCAS ASDs in non-sink 'control' and AGS donor over 60 minutes estimated using Eqs. (4.3)-(4.6).

4.4.6 Effect of absorption on crystalline and amorphous precipitation

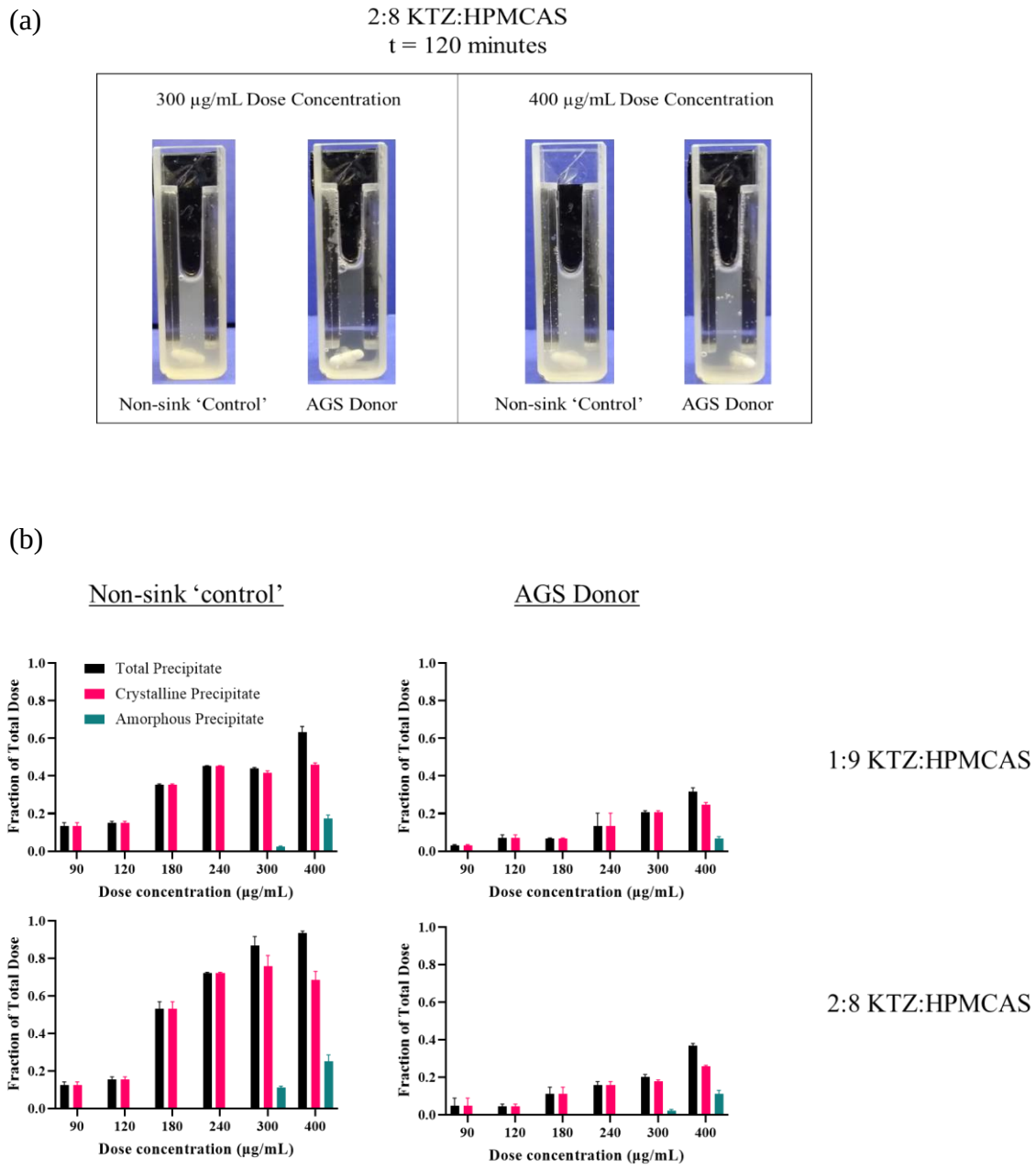

Figure 4.7. (a) Appearance of turbidity in non-sink 'control' and AGS donor upon dissolution of 2:8 KTZ:HPMCAS ASD at 300 and 400 µg/mL dose concentrations. **(b)** Estimates of total, amorphous and crystalline precipitate fraction (of total dose) using fluorescence spectroscopy and mass balance Eqs. (4.7)-(4.10).

Figure 4.7a shows the turbid appearance of dissolution media due to precipitation in non-sink 'control' and AGS donor following 120 min of dissolution of 2:8 KTZ:HPMCAS ASD at 300 and 400 µg/mL dose concentrations. The AGS donor at each dose concentration appears significantly less turbid than its non-sink 'control' counterpart, indicating lower precipitation in the dissolution media in the presence of absorption. This precipitate formed may be crystalline and/or amorphous and were quantified separately using mass balance Eqs. (4.7)-(4.10) along with fluorescence spectroscopy. The 3:7 KTZ:HPMCAS ASD is not considered since dissolution was demonstrated to be incomplete (***Figure 4.6***) and mass balance will not be applicable.

KTZ is an auto-fluorescent molecule that undergoes hypsochromic shift in response to decreasing environmental polarity due to LLPS with the fluorescence intensity increasing as amorphous precipitate concentration in the dissolution media increases (**Appendix**, ***Figure A4***). ***Figure A5*** in the **Appendix** demonstrates a good correlation between KTZ emission intensity, and the amount of amorphous precipitate calculated using mass balance. Determination of actual mass of amorphous precipitate in supersaturated solutions validates the mass balance calculations (blue circles in **Appendix,** ***Figure A5***). Linear regression of the calibration curve in ***Figure S5*** was used to determine the amount of amorphous precipitate in dissolution media of non-sink 'controls' and AGS donor at the end of 120 minutes.

Figure 4.7b shows total as well as amorphous and crystalline precipitate fractions of KTZ. It is observed that the precipitated fractions increased as dose concentration was increased with amorphous precipitate appearing only at 300 and 400 µg/mL dose concentrations. We observe a lower fraction of amorphous precipitate with 1:9 relative to

2:8 KTZ:HPMCAS ASD due to higher amorphous solubility as more polymer is released into the media in the former case. Crystalline precipitation is higher with 2:8 KTZ:HPMCAS ASD due to lower polymer concentration released into the media upon dissolution resulting in lesser stabilization of the metastable supersaturated solutions against crystallization. In AGS donor, at all dose concentrations and any drug loading, crystalline precipitate fraction is lower than the non-sink control due to lowering of concentration in the dissolution media as absorption proceeds and subsequent reduction in driving force for crystallization. The amorphous precipitate fraction is also lower in AGS donor due to precipitate redissolution as absorption proceeds as will be discussed in more detail in the next section. In case of 1:9 KTZ:HPMCAS ASD at 300 µg/mL dose concentration, due to continuous absorption, the C_{max} attained in the AGS donor possibly never attains the amorphous solubility concentration (***Figure 4.4c***), unlike the non-sink 'control' resulting in no amorphous precipitation.

This experiment demonstrates how the effect of absorption on amorphous and crystalline precipitation may be separately determined. While formation of crystalline precipitate is undesirable due to the drug reverting to its low solubility form, amorphous precipitate can form a reservoir of drug to rapidly redissolve and replenish KTZ in solution lost to absorption and maintain a constant drug concentration at amorphous solubility.[90] By this measure, formation of amorphous precipitate is not completely undesirable. Infact, it has been demonstrated that KTZ upon administration orally forms supersaturated solution and amorphous precipitate in duodenal luminal media in humans but that does not necessarily decrease its bioavailability the way crystalline precipitation does.[77,103]

4.4.7 Effect of absorption and polymer concentration on KTZ amorphous precipitate nanodroplets

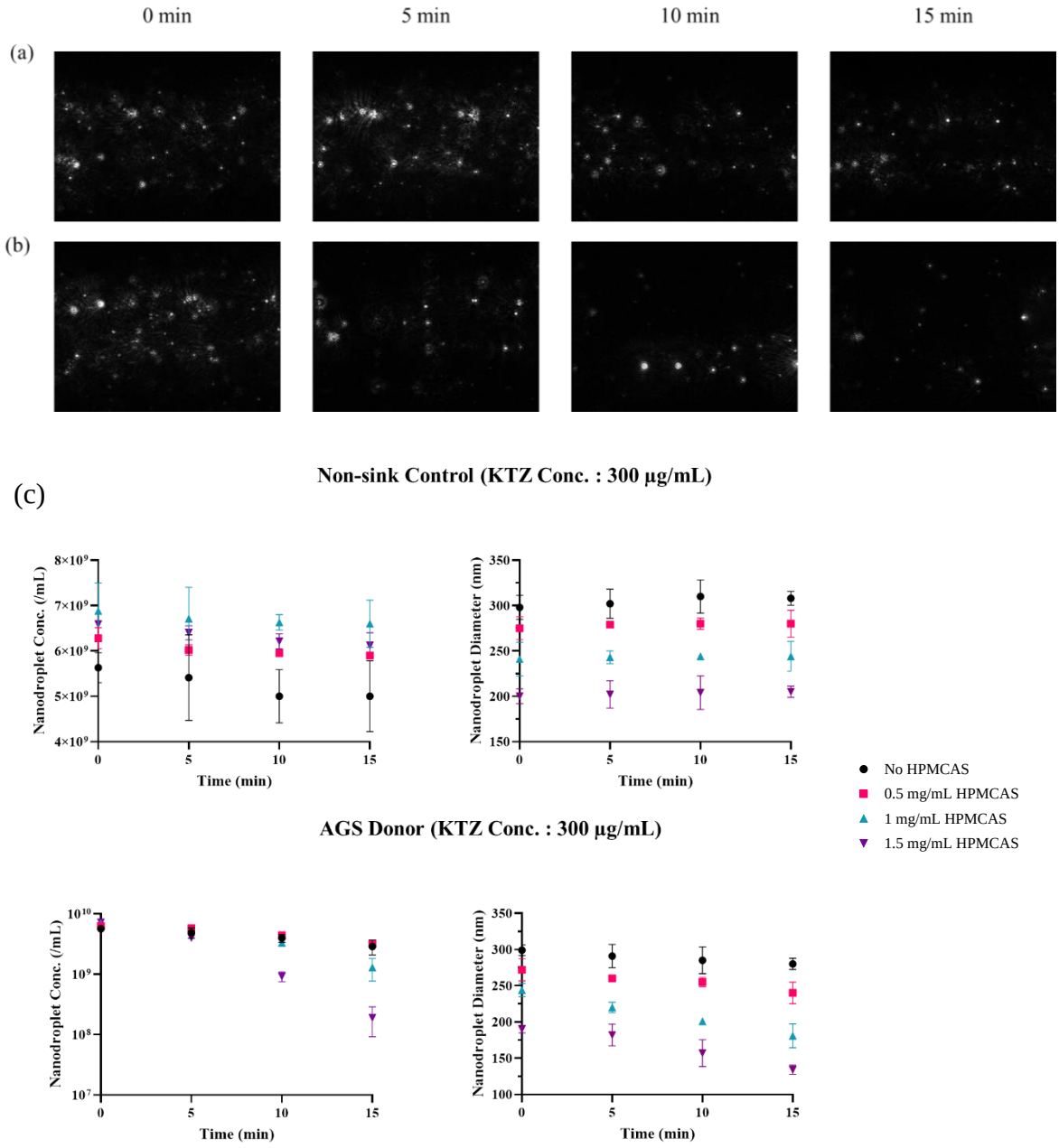

Figure 4.8. Snapshots from NTA videos of KTZ solution at 0, 5, 10 and 15 minutes after generation of 300 µg/mL supersaturated solution showing amorphous nanodroplets in **(a)** non-sink 'control' and **(b)** AGS donor. **(c)** Change in amorphous nanodroplet concentration and diameter from 0 to 15 minutes in non-sink 'control' and AGS donor as a function of dissolved HPMCAS concentration.

KTZ supersaturated solution (300 µg/mL) was generated using the pH-shift method in FaSSIF-V2 media containing 0 to 1.5 mg/mL pre-dissolved HPMCAS polymer in 'control' and AGS donor. The supersaturated solution was analyzed by NTA for size and concentration of amorphous nanodroplets for 15 minutes before significant crystallization commenced. ***Figures 4.8a,b*** show representative snapshots taken from NTA videos of supersaturated solutions containing 1.5 mg/mL pre-dissolved HPMCAS in 'control' and AGS donor acquired at 0, 5, 10 and 15 minutes. We observe a consistently high density of nanodroplets in the non-sink 'control' over 15 minutes (***Figure 4.8a***) as opposed to declining density observed in AGS donor as absorption proceeds (***Figure 4.8b***). ***Figure 4.8c*** quantitatively shows the change in concentration and diameter of these amorphous nanodroplets. In the 'control', both the diameter and concentration of amorphous nanodroplets remain constant for 15 minutes at all concentrations of pre-dissolved polymer. In the AGS donor, on the other hand, both the concentration and diameter of the nanodroplets decrease with time. Concentration decline may be attributed to redissolution of amorphous precipitate to replenish the drug in solution lost to absorption. The decline is fastest in the presence of 1.5 mg/mL pre-dissolved polymer presumably due to the smallest diameter and largest surface area of the droplets resulting in faster redissolution. The concentration depletion rate decreases as polymer concentration decreases and the resultant droplet diameter increases. Moreover, as absorption of KTZ proceeds and the proportion of polymer relative to drug increases, greater surface stabilization of KTZ nanodroplets by HPMCAS polymer results in reduction in diameter with time in all the cases.

4.5 Discussion

ASD dissolution is a very complex process marked by speciation and phase transformations, which may reduce the free drug concentration in the dissolution media that is available for absorption. While it is relatively straightforward to separate crystallized drug in the media from free drug by filtration and/or microcentrifugation, removal of colloidal submicron or nanometer-sized species by traditional dissolution sample preparation methodologies and separately measuring the free drug concentration in solution can be quite challenging.[43] Instrument-intensive methodologies such as nuclear magnetic resonance spectroscopy have been used to assess the colloidal species formed and to mechanistically elucidate the complex dissolution profiles of ASDs.[148] However, it is more practical to use simpler analytical techniques. Dialysis methods, for example, have been successfully applied to measure free concentration during ASD dissolution; these techniques, while effective, can be labor-intensive and time-consuming.[149]

The hollow fiber-based absorption module with a large surface area and low MWCO can be tuned to allow absorption of free drug species at a physiological rate. Mass transport of only free drug helps determine the thermodynamic activity of the resulting drug solution and how the presence of dissolution media additives and formulation excipients affect that activity. This in conjunction with other analytical techniques introduced earlier such as colorimetry and UV spectroscopy to assess HPMCAS polymer and drug release kinetics and fluorescence spectroscopy to measure drug concentration in the amorphous precipitate help evaluate the effect of dissolution and precipitation processes on drug absorption and vice versa.

Typically, during non-sink dissolution testing, AUCs of dissolution-time profiles are used to assess the "quality" or "efficacy" of different ASD formulations.[150] To rank order 1:9, 2:8 and 3:7 KTZ:HPMCAS ASDs, likewise, AUCs of non-sink 'control' drug concentration-time profiles were determined and are plotted in ***Figure 4.9a*** as a function of dose concentration. Having assessed the role of various drug species, the following explanations can be given to mechanistically account for the trend in AUCs:

1. At low dose concentrations, the performance of ASDs may be ranked as –

   1:9 ASD ≡ 2:8 ASD > 3:7 ASD

   At high dose concentrations, on the other hand,

   1:9 ASD > 2:8 ASD ≡ 3:7 ASD
2. At low drug concentrations, 2:8 KTZ:HPMCAS ASD performs similarly to its 1:9 counterpart with comparable dissolution rates (***Figure 4.4b***). At high dose concentrations, in the absence of absorption, crystallization (***Figure 4.7b***) limits the efficacy of 2:8 KTZ:HPMCAS ASD and is comparable to that of 3:7 KTZ:HPMCAS ASD. Moreover, at high dose concentrations of 2:8 KTZ:HPMCAS ASD, we observe solubility-limited dissolution that occurs at a dose concentration of only 400 µg/mL in case of 1:9 KTZ:HPMCAS ASD (***Table 4.2, Figure 4.3***).
3. 3:7 KTZ:HPMCAS ASD exhibits low dissolution rate at all dose concentrations (***Figure 4.4b***). While this results in the lowest efficacy at low dose concentrations (***Figure 4.6***), at higher dose concentration, slow dissolution can translate to slower supersaturation generation and crystallization rate[88,151,152], such that its efficacy is comparable to the fast dissolving and crystallizing 2:8 KTZ:HPMCAS ASD.

4. At high dose concentrations, efficacy of 1:9 KTZ:HPMCAS ASD may be overestimated due to non-discrimination between free and bound drug species (***Figure 4.4c***); concentration of the latter may be expected to be very high due high polymer loading in this ASD (***Figure 4.5***).

To compare the ASDs' efficacy using the AGS, the cumulative amount of drug absorbed at the end of 120 minutes was calculated using Eq. (6) and plotted in ***Figure 4.9b*** as function of dose concentration. The following inferences can be drawn in this case:

1. At low dose concentrations, the performance of ASDs may be ranked as –

   1:9 ASD ≡ 2:8 ASD ≡ 3:7 ASD

   At high dose concentrations, on the other hand,

   1:9 ASD ≡ 2:8 ASD > 3:7 ASD

   These trends in ASD performance based on the amount absorbed by the AGS are significantly different from the trends determined using the non-sink 'control'.
2. Even though slow dissolution rate limits the concentration of drug released from 3:7 KTZ:HPMCAS ASD (***Figure 4.6***), drug absorption from the donor media ensures a constant concentration gradient for dissolution of more drug from the ASD. Ultimately, at the end of 120 min, the amount of drug absorbed in case of 3:7 KTZ:HPMCAS ASD is equivalent to 1:9 and 2:8 KTZ:HPMCAS ASDs, except at high dose concentrations of the 3:7 KTZ:HPMCAS ASD where lower polymer concentration in the media results in extensive crystallization.
3. Due to absorption, in the 2:8 KTZ:HPMCAS ASD case, crystallization is much lower than in the non-sink 'control' (***Figure 4.7b***) and as a result, the amount of

KTZ absorbed is high, comparable to 1:9 KTZ:HPMCAS ASD and significantly higher than 3:7 KTZ:HPMCAS ASD at high dose concentrations.

4. The low MWCO of hollow fiber membrane would exclude most bile acid micelles- and polymer-bound drug species. A higher proportion of polymer-bound drug species may be expected to be formed in the case of 1:9 KTZ:HPMCAS ASD relative to 2:8 and 3:7 KTZ:HPMCAS ASDs, which releases the highest concentration of polymer into the media (***Figure 4.5***) at all dose concentrations. Inspite of high apparent donor concentration (***Table 4.2***), amount of drug absorbed in case of 1:9 KTZ:HPMCAS is not proportionally high due to lower thermodynamic activity or free drug fraction of KTZ relative to 2:8 KTZ HPMCAS ASD (***Figure 4.5***). In fact, the cumulative amount absorbed with lower thermodynamic activity 1:9 KTZ:HPMCAS ASD is on par with the more rapidly crystallizing 2:8 KTZ:HPMCAS ASD, and both are comparable to the slower dissolving 3:7 KTZ:HPMCAS ASD at low dose concentrations.

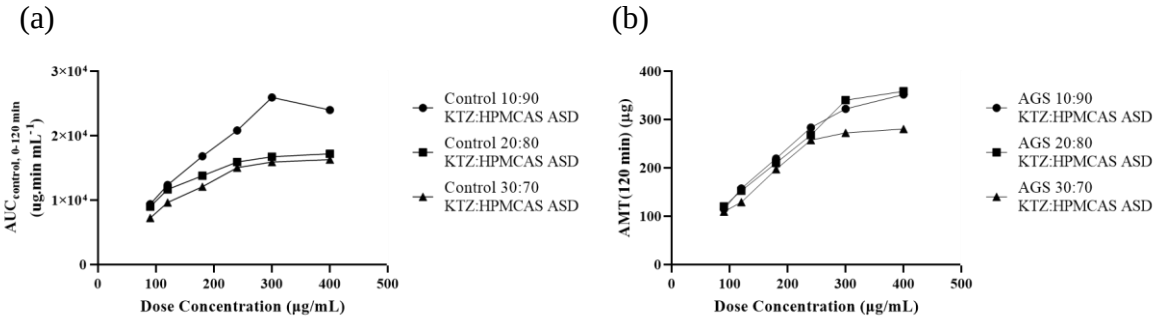

Figure 4.9. (a) AUC of non-sink 'control' dissolution-time profiles and **(b)** total amount of KTZ absorbed from AGS donor at the end of 120 minutes plotted as a function of dose concentration and drug loading in the ASD.

4.6 Conclusion

This study provides a scheme to disentangle the various dynamic equilibria occurring upon ASD drug and polymer release into the dissolution media. The equilibria are maintained in their dynamic state due to continuous drug removal by absorption at a physiological rate using the tuned AGS. The simultaneous dissolution and absorption study was conducted in conjunction with simple analytical techniques to mechanistically elucidate the influence of absorption on various bound drug species and vice versa. For the specific ASDs considered in this study, it was demonstrated that

1. how the efficacy of 3:7 KTZ:HPMCAS ASD is underestimated due to incomplete drug release in the non-sink dissolution 'control' but progresses towards completion at the end of 120 minutes in the AGS donor as drug absorption drives ASD dissolution,
2. how the efficacy of 2:8 KTZ:HPMCAS ASD is underestimated in non-sink dissolution 'control' due to extensive precipitation which is significantly reduced in the AGS donor due to absorption, and
3. how the efficacy of 1:9 KTZ:HPMCAS ASD is overestimated due to inclusion of both free and bound drug species in estimation of drug in solution available for absorption in the non-sink 'control' whereas the bound drug species were mostly excluded from the AGS absorption module.

Chapter 5: A Scheme to Establish *In Vitro/In Vivo* Correlation with a Weakly Basic BCS-II Drug, Dipyridamole

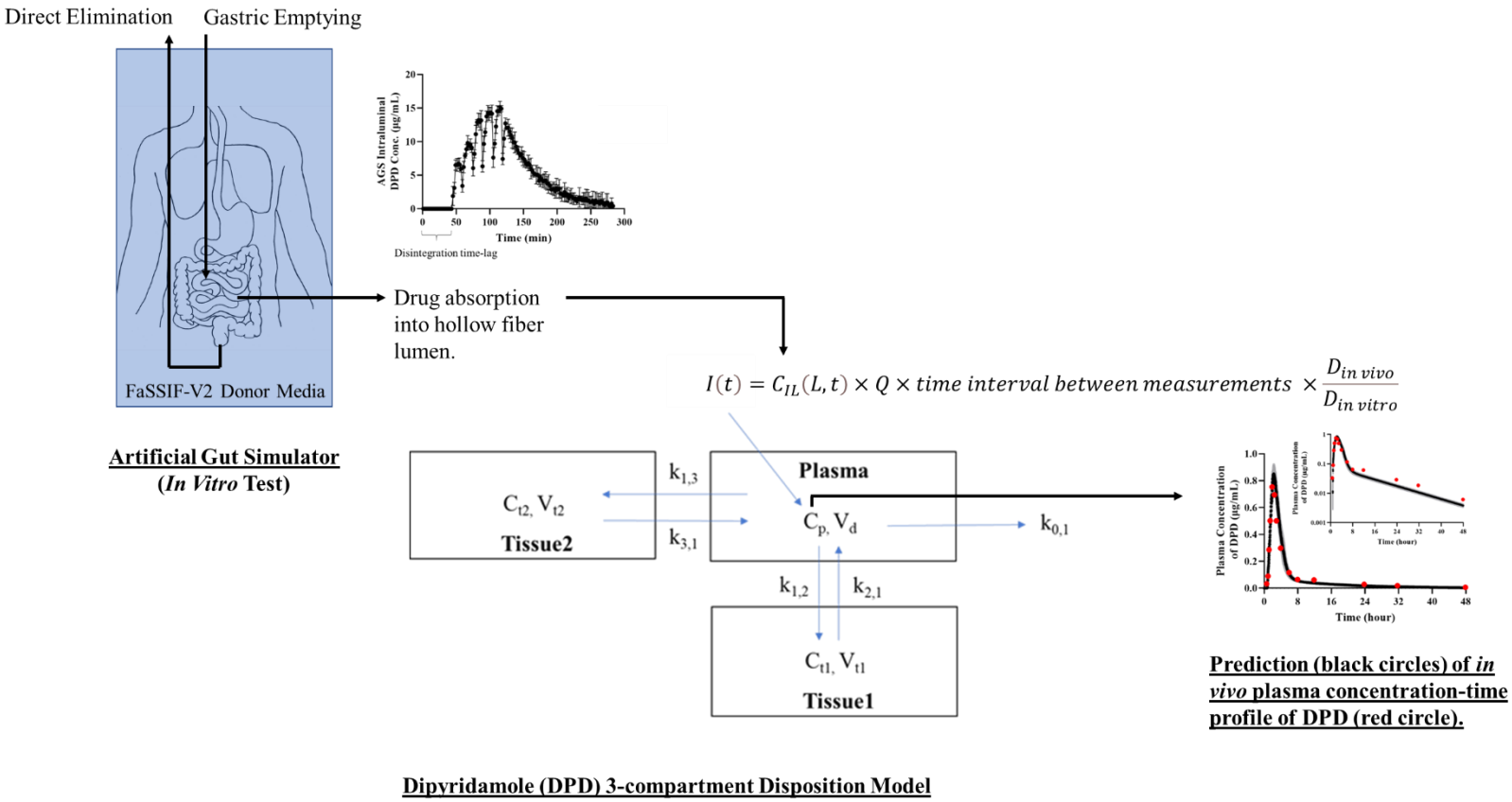

Figure 5.1. Scheme to establish *In Vitro/In Vivo* Correlation (IVIVC) for a BCS-II compound, Dipyridamole (DPD) using the Artificial Gut Simulator (AGS).

5.2 Introduction

An *in vitro/in vivo* correlation (IVIVC) represents a quantitative relationship between some easily measurable *in vitro* characteristics of a dosage form and its *in vivo* performance, which is considerably more time- and labor-expensive to obtain.[153] There are four levels of IVIVC that may be established. Level A correlation is the point-to-point correlation between *in vitro* (e.g. dissolution-time) and *in vivo* (e.g. plasma concentration-time) profiles.[82] Level B correlates an *in vitro* summary parameter (e.g. mean dissolution time) with an *in vivo* summary parameter (e.g. mean absorption time).[82] Level C compares a single time point from *in vitro* dissolution and *in vivo* profiles (e.g. C_{max}, AUC) whereas multiple Level C correlates several parameters at multiple time points.[82] Unsurprisingly, about 87% of submissions to the U.S. Food and Drug Administration (FDA) have used level A correlation, as the other levels do not reveal much information about the overall plasma concentration-time profile.[82] IVIVC activities in the pharmaceutical industry have generally been focused on applying for biowaivers to avoid *in vivo* bioavailability and bioequivalence studies whenever there are formulation, manufacturing site and process changes.[154]

It has been more than two decades since the FDA first published a guidance for IVIVC development. However, the number of IVIVC containing submissions has not increased substantially since 2008 owing to the low success rate (42%) of IVIVC acceptance by the agency.[82] One of the key challenges identified for developing IVIVC is the lack of a suitable *in vitro* dissolution testing method in predicting *in vivo* exposure. US pharmacopeial (USP) I (basket) and II (paddle) apparati most commonly used for

dissolution testing had been primarily developed for routine quality control and batch release with little consideration to biorelevance.[82,155]

In the past decade, media simulating the gastric and intestinal luminal conditions of pH, bile concentration, buffer capacity and osmolarity have been developed.[38,133] These biorelevant conditions implemented in USP dissolution testing apparati are often sufficient to predict the *in vivo* dissolution of Biopharmaceutics Classification System (BCS) – I drug molecules.[156] However, an absorptive compartment is quite critical while evaluating supersaturating formulations of low solubility, BCS-II molecules, which by definition have high permeability. Non-sink dissolution testing of such formulations can overestimate drug precipitation and underpredict drug exposure, especially of weakly basic drugs that can completely solubilize in acidic gastric media but can generate metastable supersaturated solutions as they transit through the more neutral intestinal lumen.[157] Rapid absorption from the intestinal lumen reduces the dissolved drug concentration and in turn reduces the driving force for precipitation, which is not possible in a closed, dissolution testing apparatus. For instance, Carlert et al. observed significant precipitation of a weakly basic drug during *in vitro* dissolution testing, but a dose proportional increase in plasma exposure of the drug did not suggest significant precipitation *in vivo.*[84] In that study, the authors recommended developing *in vitro* methods where there is continuous removal of drug from the dissolution media for future studies with formulations of BCS-II drug molecules. Psachoulias et al. developed a three-compartment *in vitro* set-up consisting of a duodenal, gastric and reservoir compartment.[98] Drug solution was emptied from the gastric compartment at a first order rate, as drug free media from the reservoir simultaneously diluted the drug in the duodenal compartment to simulate gastric emptying and absorption.

The sum of incoming flow rates of gastric and reservoir media into the duodenal compartment was made equal to the outgoing flow rate of the duodenal media. This *in vitro* system accurately predicted the intestinal concentration of dissolved and precipitated weakly basic model compounds due to the simulation of drug removal by dilution. However, the operating parameters of this system were selected arbitrarily and cannot be rationally determined based on the absorption rate constant of a drug.

The artificial gut simulator (AGS) equipped with an absorption module, can be used to conduct biorelevant dissolution testing (Chapter 2). The absorption module consists of hollow fibers that provide a large surface area for absorption. During dissolution testing, the absorption module is suspended in the drug donor compartment wherein the concentration gradient across the hollow fiber membrane drives the drug molecules to diffuse into the intraluminal fluid. Drug-free receiver media is continuously pumped through the hollow fibers, thereby maintaining an absorptive sink. Using the theory developed earlier, the AGS operating can be tuned to absorb the drug at a biorelevant rate (Chapter 2). In the present study, a scheme introduced before with caffeine to establish Level A IVIVC with AGS (Chapter 2), is implemented using a BCS-II model compound, dipyridamole (DPD). DPD is a weakly basic drug with poor aqueous solubility but high intestinal permeability (log P 2.74, pK_a 6.24).[77] Gastric emptying and oral absorption of 30, 50 and 90 mg doses of DPD were simulated using the AGS, which was tuned to absorb the drug at a physiological rate.[77,158]

For IVIVC establishment, a two-stage method is most commonly implemented.[82] The method involves deconvolution of *in vivo* plasma concentration-time profiles to obtain *in vivo* absorption profiles followed by establishment of the correlation between fraction

absorbed *in vivo* and that dissolved *in vitro.*[82] However, when considering mean plasma concentrations of multiple subjects, considerable variation in drug disposition between individuals can lead to erroneous results of drug absorption.[82] Alternatively, a one-stage compartment based approach has also been used, which directly relates the time profiles of *in vitro* dissolution and *in vivo* plasma concentration by using one or multi-compartment pharmacokinetic models.[159] This approach overcomes the limitation of indirect deconvolution methods for modeling complex absorption phenomena like pre-systemic metabolism and non-linear absorption as well as incorporating disintegration and dissolution mechanisms and changing solubility profile of the drug as it encounters different pH and bile acid content along the GI tract, thereby providing IVIVC a more mechanistic relevance.[82]

In the present study, the one-stage compartment-based approach was used to establish IVIVC with DPD. A compartmental model describing DPD disposition pharmacokinetics (PK) *in vivo* was developed by fitting the PK model to plasma concentration-time profile obtained upon intravenous (IV) bolus dose administration of 20 mg DPD.[158] Next, the amount of drug absorbed by the AGS was directly input into the central compartment of the PK model. The performance of the proposed approach was evaluated by comparing the predicted plasma concentration-time profile using the AGS and PK model with the *in vivo* profile.[158] Additionally, the dissolved concentration and fraction of DPD precipitate in AGS donor were compared with the measurements made in human duodenum.[77]

5.3 Materials and Methods

5.3.1 Materials

DPD was purchased from Sigma-Aldrich Co., MO and was used as received. Fasted-state simulated intestinal fluid was prepared by dissolving FaSSIF-V2 powder (Biorelevant.com, DE) in 0.032 M pH 6.5 sodium phosphate buffer prepared using monobasic sodium phosphate monohydrate, dibasic sodium phosphate heptahydrate and sodium chloride, all purchased from Sigma-Aldrich Co.[132,160] FaSSIF-V2 media was used as the drug donor media in the AGS. Bile acid and lecithin-free 0.032 M pH 6.5 phosphate buffer was used as the receiver media. Hydrochloric acid (HCl, 36.5 – 38.0%) was purchased from Sigma-Aldrich Co., and was diluted appropriately with deionized water to prepare a pH 2.7 solution.

The AGS was constructed and set-up as described earlier (Chapter 4). Briefly, to construct the absorption module, the ends of regenerated cellulose based hollow fibers (Molecular weight cut off=13kDa, d=200µm, L=4.8cm, Spectra/Por® In Vivo Microdialysis Hollow Fibers, Repligen Corporation, CA) were potted into the inlet and outlet tubes of receiver/intraluminal media emerging from a cuvette cap (Azzota Scientific, DE) using a silicone UV-cure glue (Henkel Corporation, OH). The corresponding cuvette, containing the simulated intestinal fluid, served as the donor phase.

5.3.2 Tuning the AGS to absorb DPD at a physiological rate

The operating parameters of the AGS, namely, the number of hollow fibers (*N*) and intraluminal fluid flow rate (*Q*) were selected to absorb DPD at a physiological rate constant, k_a, determined from the permeability coefficient of DPD across human intestinal epithelial membrane, P_{human}, and geometric surface area of the intestine-to-luminal volume ratio ($SA/V_{in\ vivo}$). [105]

$$k_a = P_{human} \times \frac{SA}{V_{in\ vivo}} \tag{5.1}$$

Sugano estimated $SA/V_{in\ vivo}$ to be 2.3 cm^{-1} using an equation relating human jejunal permeation rate of drug molecules to their fraction absorbed.[161] P_{human} was estimated from the permeability coefficient measurement of DPD made across Caco-2 cell monolayer ($P_{Caco-2} = 1.24 \times 10^{-6}$ cm/s[162]) using a correlation established at pH 6.5 by Sun et al.[163]

$$log\ P_{human} = [0.6532 \times log\ P_{Caco-2}] - 0.3036 \tag{5.2}$$

P_{human} for DPD was calculated to be 2.91×10^{-4} cm/s, which is approximately the same as estimates obtained in earlier studies using other methods.[164–166] Finally, k_a of DPD was estimated to be 0.0402 min^{-1}.

The simulated absorption rate constant, $k_{a,AGS}$

$$k_{\mathrm{a,AGS}} = \left(\frac{Q}{V_{in\ vitro}}\right)\left(1 - e^{-\frac{NP_{HF}A_{\mathrm{IL}}}{Q}}\right) \tag{5.3}$$

was matched to the target k_a for DPD by selecting *N* and *Q* (Chapter 2). Donor volume, $V_{in\ vitro}$, and lateral surface area of each hollow fiber, A_{IL}, were set at 1.2 mL and 0.3 cm^2,

respectively. The permeability coefficient of DPD across the cellulose hollow fiber membrane was determined to be (1.20 ± 0.04) x 10^{-4} cm/s using a method described previously (Chapter 2). Then, a mass transport study from an initially saturated solution of DPD in FaSSIF-V2 donor media [$C_{\mathrm{EL}}(0)$] was conducted at 37℃ into drug-free phosphate buffer that was pumped through the tuned absorption module. A validating estimate of $k_{\mathrm{a,AGS}}$ was obtained by fitting the extraluminal concentration [$C_{\mathrm{EL}}(t)$]-time (t) profile to Eq. (5.4) and comparing it to the "target" value, k_a.

$$C_{\mathrm{EL}}(t) = C_{\mathrm{EL}}(0)e^{-k_{\mathrm{a,AGS}}t} \tag{5.4}$$

The optimized AGS was then used to conduct mass transport studies from supersaturated solution of DPD.

5.3.3 Prediction of in vivo DPD intestinal concentration-time profile

The AGS was used to simulate a previously published case study of oral absorption of DPD in which drug supersaturation and precipitation in the intestinal contents were evaluated in 12 healthy adults.[77] 30 and 90 mg doses of DPD pre-dissolved in 240 mL of pH 2.7 HCl solution were administered to the stomachs of intubated volunteers after which samples of intestinal contents were aspirated at several time points between 5 and 70 minutes. In each sample, the dissolved concentration of DPD and precipitated fraction was determined. The raw data presented as Box-Whisker plots showing the median values, the 10^{th}, 25^{th}, 75^{th} and 90^{th} percentiles were extracted using a WebPlot Digitizer.[167]

The average intestinal volume *in vivo* is about 100 mL in humans, which remains quite constant after administration of 240 mL of a liquid even as gastric volume decreases from 240 mL to its resting volume within 60 minutes at a first-order gastric emptying rate

constant of 2.8 hour^{-1}.[168] The *in vivo* dose-to-intestinal volume ratios ($D_{in\ vivo}$:$V_{in\ vivo}$) for 30 and 90 mg doses are 0.3 and 0.9 mg/mL, respectively.

The volume of FaSSIF-V2 media in the AGS donor is 1.2 mL. To match *in vitro* dose-to-AGS donor volume ratio ($D_{in\ vitro}$:$V_{in\ vitro}$) to $D_{in\ vivo}$:$V_{in\ vivo}$ for 30 and 90 mg DPD doses, 0.36 and 1.08 mg of DPD, respectively, were dissolved in 2.88 mL of pH 2.7 HCl solution (total volume of 240 mL of pH 2.7 DPD oral solution administered in the *in vivo* study was also scaled down by the same factor as $D_{in\ vitro}$ and $V_{in\ vitro}$ for the AGS study). FaSSIF-V2 powder was dissolved in the HCl solution at a concentration of 3 mM bile acids and 0.2 mM lecithin to prevent dilution of bile acids and lecithin in the donor media as HCl solution was added to it.[77] Fractions of the stock solution were spiked into the extraluminal media every 15 min for 75 minutes at an overall first-order rate to simulate *in vivo* gastric emptying (***Table 5.1***). After each addition, the same volume of donor media as the stock solution added was pipetted out to maintain a constant 1.2 mL volume of donor media (***Table 5.1***). Absorption module was reinserted into the UV spectrophotometer donor cuvette after each dose fraction addition and the mass transport study was conducted for 120 minutes at 37℃ with the tuned AGS. After each addition of the acidic stock solution, pH of the donor media decreased (***Table 5.1***). The final pH of the donor media at the end of 120 min was found to be 5.9 which is similar to the pH measured in human duodenum after administration of 300 mL of a pH 2.5 solution.[169] Crystalline solubility of the weak base DPD (measured in the supernatant obtained by equilibrating excess solid drug in FaSSIF-V2 media followed by centrifugation) increased as the pH declined (***Table 5.1***). Separate experiments were conducted for 0, 15, 30, 45, 60, 75 and 120 minutes. At the end of each time point, the entire donor media was centrifuged at 14,800 rpm (Marathon

26KMR microcentrifuge, Thermo Fischer Scientific Inc., MA) for 10 minutes to remove precipitate particles if any and the dissolved drug concentration, $C_{EL}(t)$, in the supernatant was determined by UV spectroscopy at 287 nm. When the experiment was conducted for 120 minutes, the intraluminal fluid exiting the hollow fiber module was directed into a flow-through cell in which DPD concentration measurement was made by UV spectroscopy at 287 nm every two minutes. All experiments were conducted in duplicate.

Fraction of DPD precipitated (f_{ppt}) was determined by mass balance [Eqs. (5.5)-(5.7)].

$$T(t) = Dose_{in\ vitro}(t) - A_{DirEl}(t) - A_{IL}(t) \tag{5.5}$$

Here $T(t)$ is the total amount of drug (dissolved+precipitated) present in the donor at the end of each time point t = 0, 5, 15, 30, 45, 60, 75 and 120 min, $Dose_{in\ vitro}(t)$ is the cumulative amount of drug added to the donor till t, $A_{DirEl}(t)$ is the cumulative amount of drug directly eliminated till t as the donor media was pipetted out after each addition of DPD stock solution, and $A_{IL}(t)$ is the cumulative amount of drug absorbed by the intraluminal fluid determined till t, determined using Eq. (5.6).

$$A_{IL}(t) = \mathrm{AUC}_{IL,0-t} \times Q \tag{5.6}$$

where $\mathrm{AUC}_{IL,0-t}$ is the area under the receiver concentration-time profile.

$$f_{ppt} = \frac{T(t) - [C_{EL}(t) \times V_{in\ vitro}]}{T(t)} \tag{5.7}$$

Dissolved concentration as well as precipitated fraction of DPD in the extraluminal fluid of the AGS were compared with that measured in the duodenum *in vivo*.[77]

Additionally, a no-sink 'control' experiment (no flow in the absorption module) was conducted in the same manner as outlined above with 90 mg equivalent dose and the fraction precipitated was determined by Eq. (5.7). In this case, since there is no absorption, $T(t)$ was determined by subtracting $A_{DirEl}(t)$ from $Dose_{in\ vitro}(t)$.

Table 5.1. Summary of *in vitro* dosing schedule for the three doses of DPD, 0.36, 0.60 and 1.08 mg (which are dose equivalents of 30, 50 and 90 mg DPD doses, respectively, in clinical studies), for simultaneous precipitation and absorption testing using the AGS. After each addition of the acidic stock solution, solubility of DPD increased as pH of FaSSIF-V2 media decreased.

Time (min)	Volume of stock solution added to 1.2 mL FaSSIF-V2 media (mL)	Dose added (mg)			Volume of donor solution pipetted out after each addition (mL)	Final volume of donor solution (mL)	pH	Mean DPD crystalline solubility as a function of pH (µg/mL)
		$D_{in\ vitro}$:$V_{in\ vitro}$ = 0.3 mg/mL	$D_{in\ vitro}$:$V_{in\ vitro}$ = 0.5 mg/mL	$D_{in\ vitro}$:$V_{in\ vitro}$ = 0.9 mg/mL				
0	1.44	0.18	0.30	0.54	1.44	1.2	6.37	56
15	0.72	0.09	0.15	0.27	0.72	1.2	6.17	71
30	0.36	0.045	0.075	0.135	0.36	1.2	5.99	78
45	0.18	0.0225	0.0375	0.0675	0.18	1.2	5.95	81
60	0.09	0.01125	0.01875	0.03375	0.09	1.2	5.93	84
75	0.09	0.01125	0.01875	0.03375	0.09	1.2	5.91	89
	Total: 2.88 mL	**Total: 0.36 mg**	**Total: 0.60 mg**	**Total: 1.08 mg**				

5.3.4 Prediction of in vivo DPD plasma concentration-time profile

A semi-log plot of DPD plasma concentration-time profile following a 20 mg IV bolus dose reveals that DPD declines in a triexponential manner (pink filled circles in the inset of ***Figure 5.2a***).[158] Thus, a three-compartment PK model describing DPD disposition was implemented in the Simbiology® toolbox (Matlab R2018a, MathWorks, MA) as shown in ***Figure 5.2b***. The estimates of volume of distribution (V_d), distribution rate constants (k_{12}, k_{21}, k_{13}, k_{31}) and elimination rate constant (k_{10}) were obtained using the *Fit* program of Simbiology® to fit the PK model to *in vivo* plasma concentration-time profile using a non-linear least-squares (lsqnonlin) with combined (constant plus proportional) error model.

The fitting result is shown in ***Figure 5.2a*** (black line) and the parameter estimates are given in ***Table 5.2***. PK parameter estimates for DPD were also obtained in an earlier study but did not provide a good fit to the *in vivo* data and were not used in this study.[165]

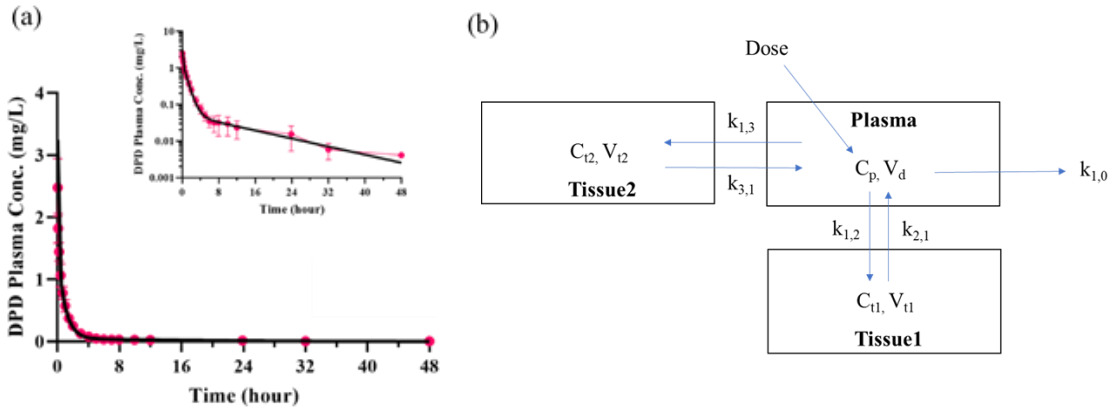

Figure 5.2. (a) Human DPD plasma concentration-time profile and (inset) semi-log plot (pink circles) obtained after a 20 mg IV bolus dose.[158] Black line represents fit of **(b)** a 3-compartment PK model describing DPD disposition to the plasma concentration-time profile.

Table 5.2. Systemic PK parameters for DPD estimated from Mahony et al.[158]

Pharmacokinetic Parameter	Value
V_d (mL)	6200
k_{10} (min^{-1})	0.0227
k_{12} (min^{-1})	0.0800
k_{21} (min^{-1})	0.1019
k_{13} (min^{-1})	0.0106
k_{31} (min^{-1})	0.0016

Human plasma concentration-time profile following oral administration of 50 mg DPD tablet was take from the literature.[158] The mean gastric pH after administration of 200 mL water was found to be 2.7 in humans.[170] Assuming that the DPD tablet was also administered with a glass of water (200 – 300 mL), one can expect the gastric pH in this case also to slightly increase to 2.7 from its resting pH of 1.5.[171] Since DPD is a weakly basic drug, it can be expected to fully dissolve in acidic gastric media.

To simulate DPD gastric emptying and absorption using the AGS, similar to the last experiment, a scaled-down dose of 0.6 mg was dissolved in 2.88 mL of pH 2.7 HCl solution with 3 mM bile acids and 0.2 mM lecithin. Fractions of this acidic stock solution were then added to the extraluminal FaSSIF-V2 media at 0, 15, 30, 45, 60 and 75 min as per the dose schedule shown in ***Table 5.1***. The run was conducted for 240 minutes. DPD concentration in the intraluminal fluid [$C_{IL}(L,t)$] was measured by UV spectroscopy at 287 nm every two minutes.

$C_{IL}(L,t)$ was used to generate an input function $I(t)$ that describes the *in vivo* amount of drug absorbed with time.

$$I(t) = C_{IL}(L,t) \times Q \times time\ interval\ between\ measurements\ \times \frac{D_{in\ vivo}}{D_{in\ vitro}} \qquad (5.8)$$

$I(t)$ was ultimately input into the plasma compartment of the PK model [Eq. (5.9), ***Figure 5.2b***] to predict the *in vivo* plasma concentration time profile of DPD and establish Level A IVIVC.

$$\frac{dC_p}{dt} = \frac{I(t)}{V_d} - C_p(k_{10} + k_{12} + k_{13}) + \frac{C_{t1} \times V_{t1}}{V_d}(k_{21}) + \frac{C_{t2} \times V_{t2}}{V_d}(k_{31}) \qquad (5.9)$$

$$\frac{dC_{t1}}{dt} = \frac{C_p \times V_d}{V_{t1}}(k_{12}) - C_{t1}(k_{21}) \tag{5.10}$$

$$\frac{dC_{t2}}{dt} = \frac{C_p \times V_d}{V_{t2}}(k_{13}) - C_{t2}(k_{31}) \tag{5.11}$$

5.4 Results

5.4.1 Tuning the AGS to absorb DPD at a physiological rate

The absorption rate constant, $k_{\mathrm{a,AGS}}$ of DPD, mapped as function of *N* and *Q* in ***Figure 5.3a*** using Eq. (5.3), increases with increasing surface area for absorption and better sink conditions. The physiological k_{a} of DPD is obtained when *Q* and *N* are set to 225 µL/min and 25, respectively. DPD fraction remaining in the donor declined to 0.1 at the end of an hour of mass transport from an initially saturated drug solution (solid red circles in ***Figure 5.3b)***. The parameter $k_{\mathrm{a,AGS}}$ was estimated by fitting the experimental fraction absorbed-time profile to Eq. (5.4) (black line in ***Figure 5.3b***) and was found to be 0.0402 ± 0.0005 min^{-1} which is the same as the physiological k_{a} for DPD determined using Eqs. (5.1) and (5.2).

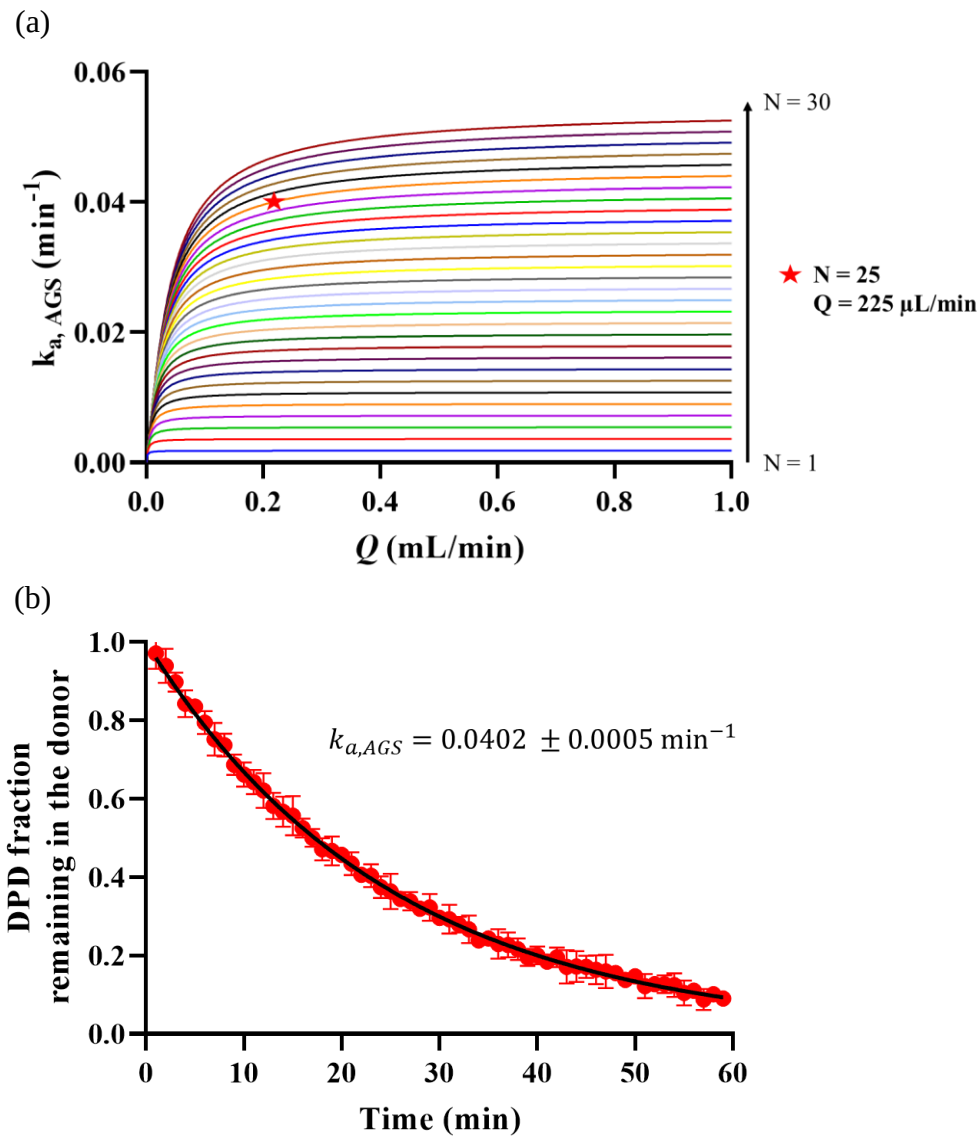

Figure 5.3. (a) Family of plots obtained for $k_{a,AGS}$ as a function of Q and N using Eq. (5.3). To obtain a physiological k_a of 0.0402 min^{-1} of DPD [Eqs. (5.1) and (5.2)], an absorption module consisting of 25 hollow fibers and intraluminal receiver fluid flow rate of 225 µL/min was used. **(b)** Fraction of DPD remaining in the donor when DPD at initial saturation solubility concentration was absorbed by the optimized absorption module. The black line represents the fit of experimental data points to Eq. (5.4) to estimate $k_{a,AGS}$ value of 0.0402 ± 0.0005 min^{-1}.

5.4.2 Prediction of in vivo DPD intestinal concentration-time profile

In vivo dissolved DPD concentration profiles in the duodenum after administration of 30 and 90 mg doses solubilized in pH 2.7 HCl solution to human volunteers are shown as box-whisker plots in ***Figure 5.4.***[77] To simulate drug absorption *in vitro* from a small volume AGS donor, the drug doses were appropriately scaled down (***Table 5.1***). The entire dose was not dumped at once into the donor. Instead, fractions of DPD in HCl solution were spiked into FaSSIF-V2 media every 15 minutes for 75 minutes to simulate an overall first-order gastric emptying process (***Table 5.1***). This was done to generate supersaturation at a physiological rate, since evidence from earlier studies has suggested that excessively high initial supersaturation or a very fast rate of supersaturation generation, which occurs when the whole dose is dumped at once into the donor media, leads to a surge in maximum supersaturation followed by a sharp decline due to rapid nucleation and crystallization.[76,88]

The concentration of dissolved drug in the AGS donor and absorbed drug in the intraluminal fluid of the tuned absorption module was measured for 120 min by UV spectroscopy. AGS donor concentration-time profiles are overlaid on the *in vivo* profiles in ***Figure 5.4*** (black circles are interpolated for clear visualization).[77] At the initial few time points, concentration of drug measured in the AGS donor slightly underpredicted the *in vivo* concentration especially in the case 90 mg dose equivalent (***Figure 5.4b***). DPD has a relatively low solubility in FaSSIF-V2 media at pH > 6 which exists for 30 minutes. DPD is also a moderately fast crystallizer.[172] Upon addition of concentrated acidic stock solution of DPD to pH 6.5 FaSSIF-V2 media, supersaturated solutions are generated characterized by turbidity and subsequent formation of dispersed particles due to crystallization. This may not be the case in the intestinal lumen where the presence of additional components

such as free fatty acids and cholesterol can further solubilize DPD and possibly limit crystallization.[98] In fact, the mean solubility of DPD in human intestinal aspirates was greater than 450 µg/mL which is much higher than the measurement obtained in FaSSIF-V2 media.[77] Unsurprisingly, the fraction precipitated in the AGS donor (open black circles in ***Figure 5.5***), estimated using mass balance Eqs. (5.5)-(5.7) when simulating absorption of 90 mg equivalent DPD dose was much higher than that observed in the GI tract (open red squares in ***Figure 5.5***).[77] In case of 30 mg equivalent dose, DPD fraction precipitated in the donor (solid black circles in ***Figure 5.5***) was only slightly higher than the *in vivo* fraction (solid red squares in ***Figure 5.5***). At later time points, as absorption proceeds and the donor media becomes more acidic (***Table 5.1***), DPD precipitate redissolves.

Overall, we observe that the *in vitro* profiles quite adequately captured the *in vivo* data. We note here that about 55% of the drug was eliminated directly upon aspiration of AGS donor media with a pipette after each dose fraction addition. DPD has a bioavailability of only 43% as a large fraction of the dose administered was eliminated unchanged through the feces.[173] Thus, direct elimination of DPD from the donor media also simulates direct elimination from the intestine. Additionally, an experiment with the 90 mg equivalent dose was also conducted with a 'control' (no flow in the absorption module) to represent non-sink testing conditions. In this case, the decline in dissolved drug concentration (interpolated green stars in ***Figure 5.4b***) during the initial time points is due to crystallization. At later time points, drug concentration increases as a higher fraction of the dose is added to FaSSIF-V2 media. The fraction of DPD precipitated in the non-sink 'control' estimated using Eq. (5.7) (interpolated green stars in ***Figure 5.5***) is much higher than both AGS donor and *in vivo* observations, indicating that a much lower DPD

bioavailability will be predicted by non-sink dissolution testing relative to the AGS, consistent with our earlier observations with another weakly basic BCS-II compound, ketoconazole (Chapters 3 and 4).

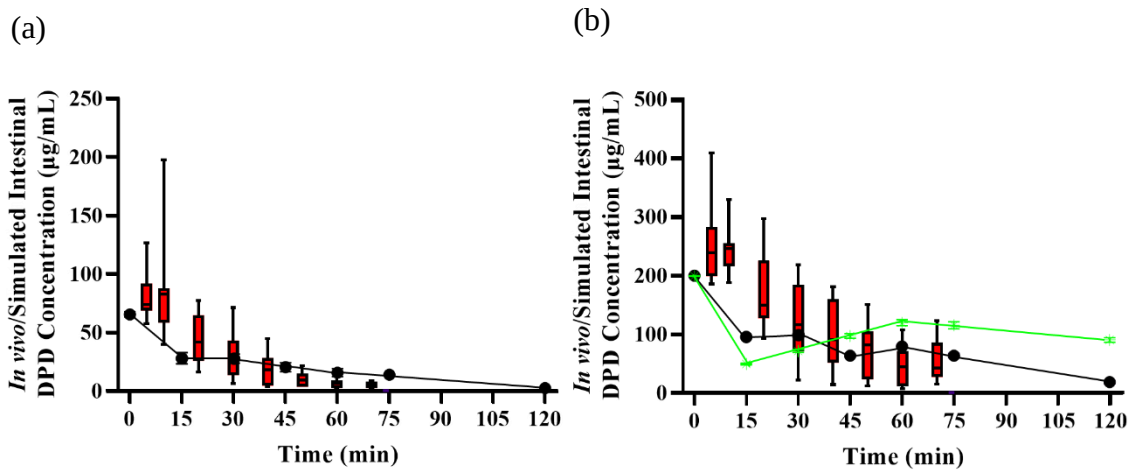

Figure 5.4. *In vivo* duodenal[77] (red box-whisker plot) and *in vitro* AGS donor (black circles) and non-sink control (green stars) concentration-time profiles obtained upon actual/equivalent administration of DPD **(a)** 30 mg, and **(b)** 90 mg doses.

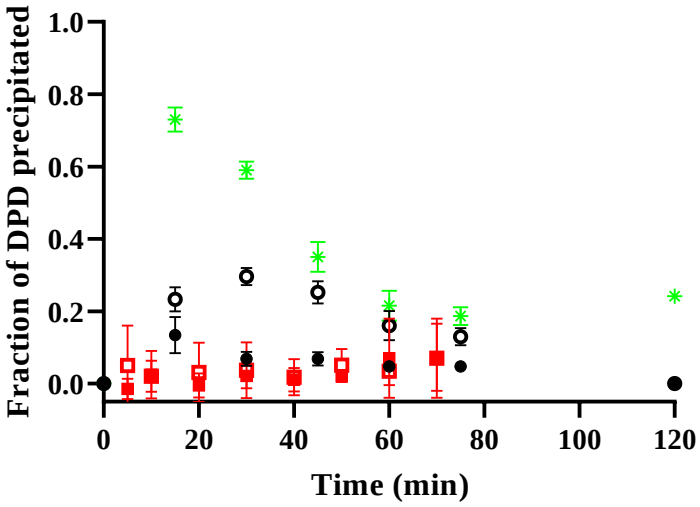

Figure 5.5. Fraction of DPD precipitated in the duodenum[77] (red solid squares, 30 mg dose; red open squares, 90 mg dose), AGS donor (black solid circles, 30 mg dose equivalent; black open circles, 90 mg dose equivalent) and non-sink control (green stars, 90 mg dose equivalent).

5.4.3 Prediction of in vivo DPD plasma concentration-time profile

The plasma concentration-time profile of DPD after oral administration of a 50 mg tablet was predicted by scaling up and inputting the drug concentration absorbed in the AGS intraluminal fluid (***Figure 5.6a)*** per unit time [Eq. (5.8)] into the central compartment of the drug disposition model (***Figure 5.2b***). The sudden decline in drug concentration in the intraluminal fluid at each point of addition of a fraction of drug dose is due to the removal of the AGS absorption module from the donor media resulting in absence of drug absorption, and dilution of intraluminal drug concentration, for less than a minute.

After oral administration, DPD tablet is known to show an absorption lag-time of 34 to 75 min due to slow tablet disintegration.[174] Since a pre-dissolved acidic solution of DPD was used here to make dose additions to the AGS donor, a 45 min time delay was introduced in the input to the PK model to account for disintegration. ***Figure 5.6b*** compares the plasma concentration-time profile predicted by the AGS (black circles) with observed the data (red circles).[158] The predicted profile agrees quite well with the *in vivo* profile including the observation of biexponential decline following the absorptive phase (inset in ***Figure 5.6b***). The first phase of decline seen in IV bolus dose disposition (***Figure 5.2a***) gets obscured by the absorptive phase,[33] so the decline does not appear triexponential.

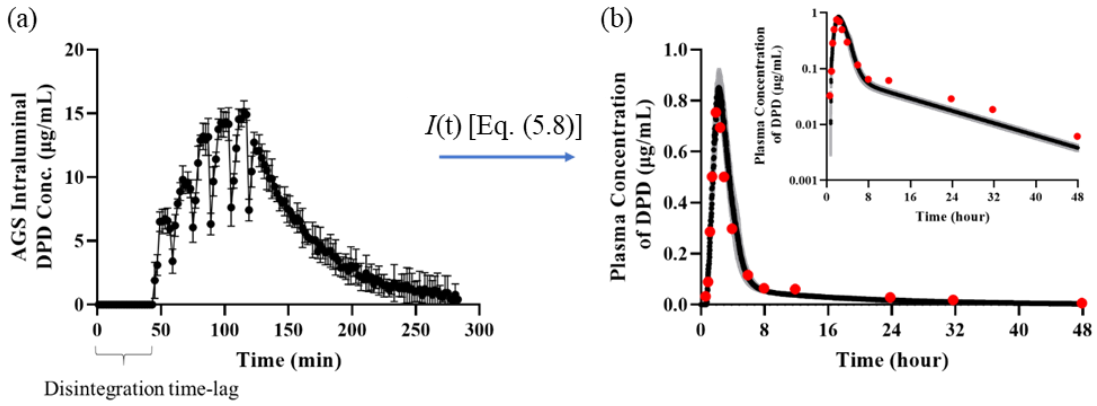

Figure 5.6. (a) Intraluminal DPD concentration-time profile as caffeine was absorbed from the donor medium. Peaks represent the points of addition of fractions of DPD dose to simulate gastric emptying at a first order rate constant, 2.8 hour^{-1} (***Table 5.1***). **(b)** Overlaid *in vivo* (red circles) and predicted (black circles) plasma concentration-time profiles using the three-compartment PK model (***Figure 5.2b*)** with AGS *in vitro* absorption data [Eq. (5.8)] as input.

5.5 Discussion

Developing IVIVCs has been encouraged by regulatory agencies for more than two decades, not just for supporting biowaiver applications, but also to facilitate decision making during early phases of drug development such as formulation optimization and design space establishment for critical material attributes and process parameters.[82] This would enhance product and process understanding and ensure predictable performance throughout the product's lifecycle. However, establishing IVIVC is not straightforward, and one of the frequently cited causes of failure is the lack of physiologically relevant methods to conduct dissolution testing.[82] The purpose of this study was to demonstrate how absorption data from the AGS, tuned to absorb drug at a physiological rate, can be scaled-up and input into a compartment-based PK model to predict *in vivo* intestinal and plasma concentration-time profiles of a BCS-II drug, DPD and establish Level A IVIVC.

Utilization of AGS is especially relevant for formulations of weakly basic drugs that supersaturate and precipitate in the neutral environment of the intestinal lumen after being transferred as concentrated solutions from acidic stomach.[77] Crystallization in the gut from the metastable supersaturated solution can significantly reduce the rate of oral absorption and drug bioavailability. This effect should be more pronounced at higher doses since rate of precipitation increases with increasing degree of supersaturation, indicated by a less-than-proportional increase in C_{max} and/or AUC of plasma concentration-time profile with increasing doses.[98] However, dose proportional increases in C_{max} and AUC have been observed with most of the weakly basic drugs tested including DPD even when precipitation was observed in the intestinal lumen.[12,13,34] This indicates that precipitation *in vivo* does not significantly influence the bioavailability of weakly basic drugs, probably due to a limited degree of precipitation and/or precipitate redissolution as the drug is continuously removed from the luminal media by absorption. This is inconsistent with the *in vivo* predictions of bioavailability made using closed dissolution testing methods that predict limited systemic drug exposure due to significant precipitation in the dissolution media.[30,35]

In the current study with the AGS tuned to absorb DPD at a physiological rate (***Figure 5.3***), the time profiles of dissolved concentration and precipitated fraction of the drug in donor predict the *in vivo* duodenal profiles better than the non-sink 'control' (***Figures 5.4 and 5.5***).[77] At a higher dose equivalent of 90 mg, a higher fraction of precipitate was observed with the AGS donor relative to *in vivo* measurements due to solubility limitation of the drug in FaSSIF-V2 media (***Table 1***) which can be resolved by making the media more biorelevant in composition by adding fatty acids and cholesterol.[98] DPD

concentration in the intraluminal fluid was scaled-up [Eq. (5.8)] and input into the 3-compartment disposition model for DPD (***Figure 5.2b***) to predict plasma concentration-time profile obtained after administration of 50 mg DPD tablet (***Figure 5.6***). The predicted profile was in good agreement with the *in vivo* profile, and Level A IVIVC was established.[158]

In general, the AGS can be useful in evaluating the effects of various gut physiological and formulation variables on drug absorption and ultimately, plasma concentration. For instance, addition of certain crystallization inhibiting polymers to the formulation or an increase in bile micelles in the intestinal lumen upon food intake is known to negatively influence absorption rate of certain drugs due to reduction in free fraction of the drug available for absorption.[36,37] This reduction in unbound drug species and absorption rate was also indicated in the AGS study conducted with ketoconazole in the presence of hypromellose acetate succinate polymer in Chapter 4. AGS can then be used to evaluate different formulations for supersaturation, precipitation and absorption of unbound drug species to determine the influence of different excipients on drug plasma concentration-time profile. Similarly, effect of food on drug absorption can also be predicted by simulating appropriate conditions in the AGS donor.

The paradigm implemented in the present work with the AGS can be used to guide future IVIVC studies. During the drug discovery/development phase, *in vivo* data to estimate k_a of the drug is often unavailable. The scheme introduced here can be used to estimate human k_a from the Caco-2 cell monolayer permeability coefficient which is relatively easy to obtain. The low volume donor solution used here can support early phase drug development activities by conducting tests in a material sparing manner. However,

for evaluating conventional dosage forms like tablets and capsules, the donor volume can be scaled up to, say, 100 mL to match the intestinal volume with proportional scale-up of the hollow fiber surface area. Moreover, to simulate selective absorption of unionized drug species, similar to the phospholipid intestinal epithelium, future studies can entail coating of the hollow fiber membrane with phospholipids to assess weakly acidic drugs and salt formulations.

5.6 Conclusion

A compartment-based approach was integrated with *in vitro* AGS test to establish IVIVC of a weakly basic, BCS-II drug. DPD was added to the AGS donor at a first order rate constant of 2.8 $hour^{-1}$ (gastric emptying rate constant) to simulate physiological rate of supersaturation generation. Simultaneously, DPD concentration in the donor depleted due to absorption at a rate constant of 0.0402 min^{-1} and precipitation. In case of 30 and 90 mg equivalent doses, time profiles of DPD concentration and fraction absorbed in the AGS donor matched adequately with the *in vivo* data. Non-sink control, on the other hand, overpredicted the fraction of drug precipitated. In case of 50 mg dose, drug concentration absorbed by the intraluminal fluid was input into the central compartment of a 3-compartment disposition model for DPD to predict the plasma-concentration time profile. The *in vitro* predicted and *in vivo* profiles agreed well with each other, establishing Level A IVIVC. This study demonstrates the importance of having an absorptive sink tuned to remove drug from the donor at a physiological rate to accurately simulate drug supersaturation and precipitation in the intestinal lumen.

Chapter 6. Conclusions and Recommendations for Future Work

6.1 Conclusions

This dissertation introduced a novel, convenient, inexpensive and material-sparing technique of conducting simultaneous, biorelevant dissolution and absorption testing of formulations of poorly soluble drugs by using the hollow-fiber based artificial gut simulator (AGS). The inherent flexibility of the system in terms of modifying the various operating parameters such as the number and length of hollow fibers (i.e. hollow fiber surface area for absorption), volume of the donor and intraluminal fluid flow rate, makes it attractive to be used with various drugs with differing absorption rate constants. For instance, in this study, the AGS was used with caffeine (k_a=0.029-0.039 min^{-1}), ketoconazole (k_a=0.013 min^{-1}) and dipyridamole (k_a=0.040 min^{-1}) by simply varying the operating parameters.

Chapter 2 described the design and working principle of the AGS in detail. A theory of mass transport across the hollow fiber membrane was developed and validated using a high aqueous solubility drug, caffeine. This theory was utilized to successfully tune the operating parameters of the AGS to match the *in vitro* and *in vivo* absorption rate constants of the model drugs used in this study. This step is key for conducting simultaneous dissolution and absorption tests with supersaturating dosage forms of BCS-II compounds.

In Chapter 3 it was demonstrated that reduction in drug concentration due to absorption simulated at a physiological rate reduced the driving force for precipitation in the AGS donor. This was unlike the non-sink 'control' where significantly higher precipitation was observed in the absence of an absorptive sink. Moreover, it was also demonstrated that absorption at a rate lower than the physiological rate also increased the extent of drug

precipitation in the AGS donor, indicating that it is critical to mimic *in vitro* absorption not just at a physiologically relevant rate, but at a physiologically observed rate.

In Chapter 4, simple analytical techniques used in conjunction with the AGS enabled decoupling of the impact of drug absorption on dissolution and crystallization as well as impact of bound drug species on absorption. Previously, such an analysis was done by dialysis methods which, while effective, can be labor-intensive and time-consuming .[149] The AGS testing method was carried out relatively simply and was used to elucidate the complex dissolution profiles of different ASDs.

In Chapter 5, the AGS was used to simulate gastric emptying and absorption of weakly basic, BCS-II compound, dipyridamole. The output of AGS i.e. the concentration of drug absorbed was scaled up and input into a 3-compartment disposition model for dipyridamole to accurately predict its *in vivo* plasma concentration-time profile, thereby establishing IVIVC.

Overall, this dissertation highlights the significance of drug removal at a physiological rate of absorption and exclusion of bound drug species from the absorption module in the AGS simultaneous dissolution and absorption testing system for BCS-II drug formulations that is far superior to the closed, non-sink dissolution apparati in terms of biorelevance.

6.2 Recommendations for Future Work

The experiments with the AGS described thus far provide a general framework for conducting simultaneous dissolution and absorption testing with BCS-II drug ASD formulations. However, there is much that remains to be explored to establish biorelevance in terms of hydrodynamics of the dissolution vessel and permeation through a phospholipid membrane (similar to the intestinal epithelium). The following subsections provide examples of avenues that are ripe for exploration.

6.2.1 Understanding the role of the unstirred water layer in BCS-II drug absorption

For some lipophilic, low aqueous solubility compounds, diffusion across the unstirred water layer (UWL) present adjacent to the epithelial membrane of the intestinal tract can be slower than absorption through the epithelial membrane itself.[177] In such cases UWL permeability can be increased by maximizing the total drug available for diffusion, which can be in the form of unbound drug as well as drug bound to micelles, colloids and complexes.[141,178,179] For instance, by introducing bile micelles and HPMCAS colloids in the dissolution media, the flux of itraconazole across the UWL was enhanced.[95,180] On the other hand, absorption of ketoconazole was limited by diffusion across only the lipid-filled artificial membrane and not UWL since addition of solubilizing micelles did not increase the flux.[180] To determine the rate-limiting steps to drug absorption as a function of drug properties, dose, pH and formulation characteristics, the hollow fibers can either be impregnated with phospholipids[115] or the aqueous intraluminal fluid can be replaced by more lipophilic 1-octanol[181] or 1-nonanol[182] to simulate drug partitioning across the intestinal membrane. If, for a drug, addition of solubilizing agents increases the flux across

the membrane coated with phospholipids, then the absorption of that drug is UWL permeability rate-limited.

6.2.2 Understanding the hydrodynamics in the AGS donor cuvette

The hydrodynamics in the dissolution vessel of the AGS is controlled by the stirring rate. In this study, the stirring rate was arbitrarily chosen to ensure homogeneous distribution on the dissolution media contents in the donor. However, similar to USP-I and II apparati, there may be inherent variability in the hydrodynamics each time a test is conducted along with hydrodynamic dead zones.[37] Poor hydrodynamics can also increase the thickness of the UWL adjacent to the hollow fiber surface, which can further slow down the mass transfer of a lipophilic drug.[183] *In vivo* UWL is thought to be 30-100 µm thick, consistent with very efficient mixing at the surface of the gastrointestinal tract.[184] However, UWL thickness adjacent to a PAMPA membrane in a well-stirred system was reported to be between 500-1200 µm.[185] It then becomes imperative to study the hydrodynamics in the AGS donor as a function of stirring speed and stirrer type to determine if it can be made to mimic the GI conditions. In an earlier study, laser doppler velocimetry and computational fluid dynamics were used to experimentally map and computationally predict the velocity distribution inside a standard USP-II apparatus.[37] These techniques may also be employed to the study the hydrodynamics in the AGS donor.

6.2.3. Conducting simultaneous dissolution and absorption testing with non-ASD supersaturating formulations

In the current state, both ionized and unionized drug species can indiscriminately diffuse across the hollow fiber membrane. However, *in vivo,* only the unionized species is

available for absorption.[33] Thus, the test should be made more selective to absorb only the unionized drugs to discriminate various formulations of salts and weakly acidic drugs. Impregnating the hollow fibers with phospholipids or replacing the aqueous intraluminal media with a more lipophilic solvent will be useful in this regard.

6.3.4. Incorporating the hollow-fiber based absorption module into an Artificial Stomach and Duodenum apparatus

An artificial stomach and duodenum (ASD) apparatus consists of gastric and duodenal compartments.[186] Media from the gastric compartment is emptied into the duodenal compartment at a first-order rate. The AGS absorption module can be incorporated into the duodenal compartment to use the ASD apparatus to simulate gastric emptying and absorption simultaneously. The volume of the gastric and duodenal compartments can be set at 240 and 100 mL, simulating *in vivo* volumes, so that disintegration and dissolution testing of whole oral dosage forms like capsules and tablets can be done at later stages of drug development.

6.3.5. High throughput screening of formulations

Due to simplicity of testing with the AGS and inclusion of absorption module in a small volume UV spectrophotometer cuvette for continuous, in-line concentration measurements in the donor and receiver, the AGS can be used to screen multiple formulations simultaneously in a high-throughput manner in a multi-cell UV spectrophotometer during the early stages of drug development.

Appendix

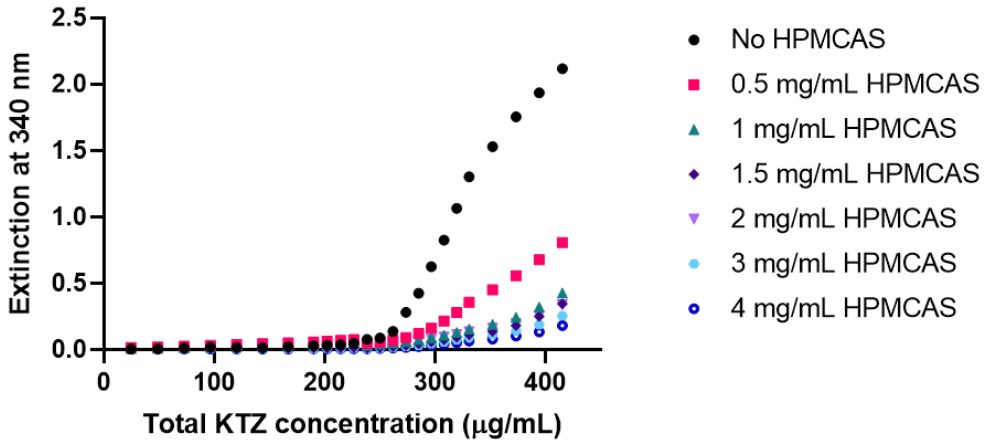

Figure A1. Extinction of KTZ solution at a non-absorbing wavelength of 340 nm plotted as a function of increasing drug concentration in FaSSIF-V2 media in the presence of 0 to 4 mg/mL dissolved HPMCAS polymer.

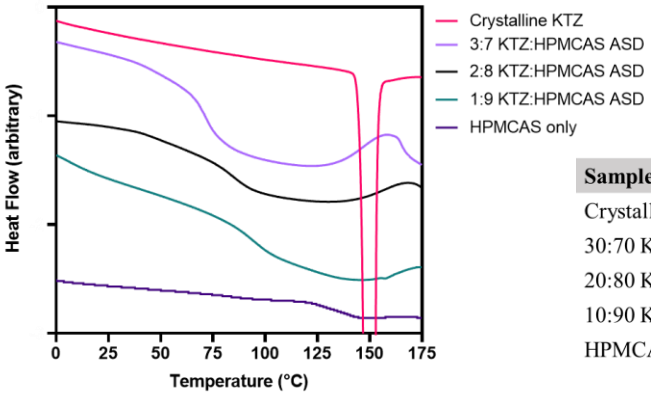

Sample	Phase Transition Temperature
Crystalline KTZ	T_m = 149°C
30:70 KTZ:HPMCAS ASD	T_g = 72°C
20:80 KTZ:HPMCAS ASD	T_g = 84°C
10:90 KTZ:HPMCAS ASD	T_g = 94°C
HPMCAS alone	T_g = 139°C

Figure A2. DSC thermograms of crystalline KTZ and HPMCAS alone as well as 1:9, 2:8 and 3:7 KTZ:HPMCAS ASDs. Their phase transition temperatures that is, melting point T_m and glass transition temperatures T_g are listed.

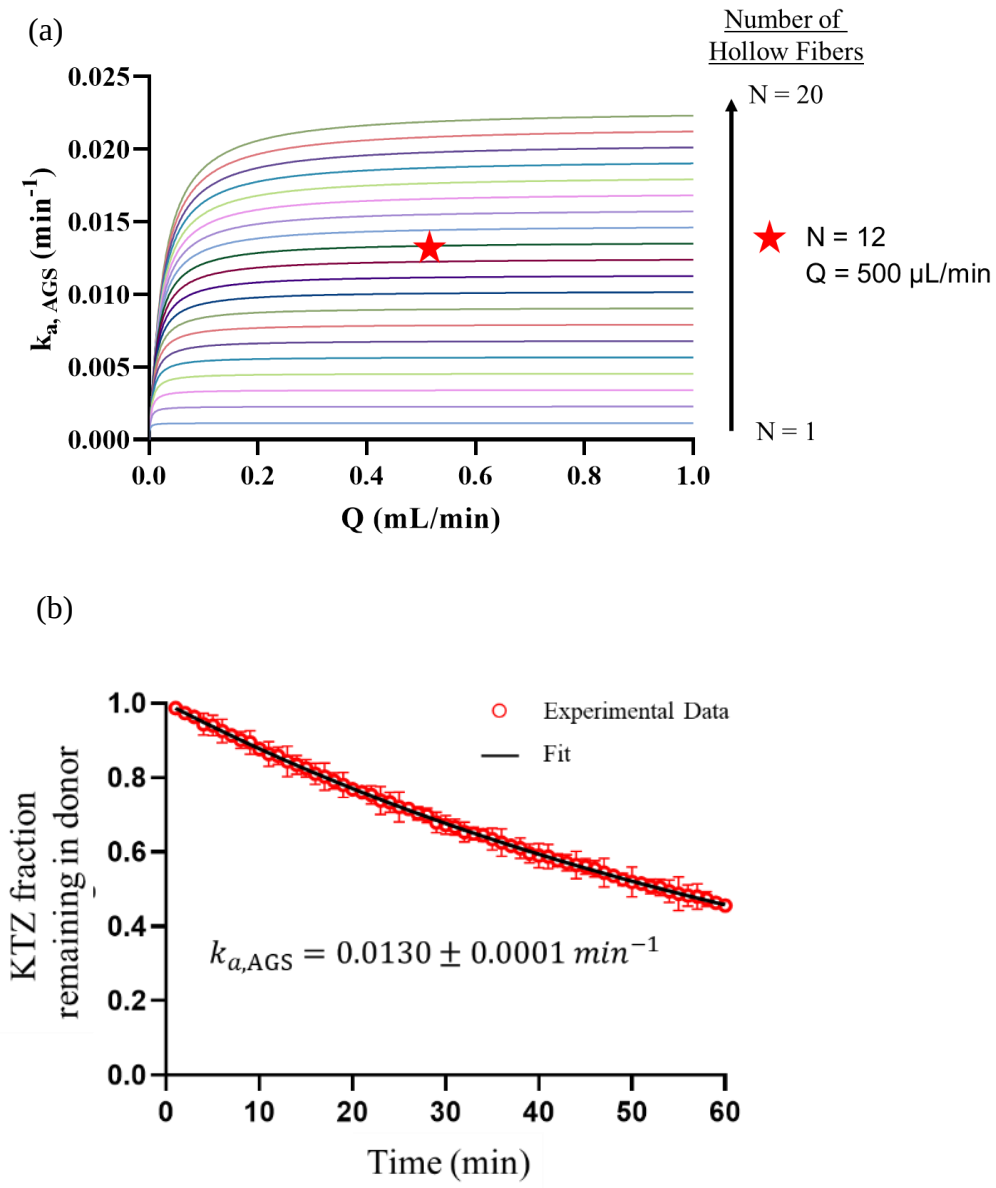

Figure A3. (a) Family of plots obtained for $k_{a,AGS}$ as a function of Q and N using Eq. (4.1). To obtain a physiological k_a of 0.013 min^{-1} of KTZ[38], an absorption module consisting of 12 hollow fibers and intraluminal receiver fluid flow rate of 500 µL/min was used. **(b)** Fraction of KTZ remaining in the donor when KTZ at initial saturation solubility concentration was absorbed by the tuned absorption module. The black line represents the fit of experimental data points to Eq. (4.2) to estimate $k_{a,AGS}$ value of 0.013 ± 0.0001 min^{-1}.

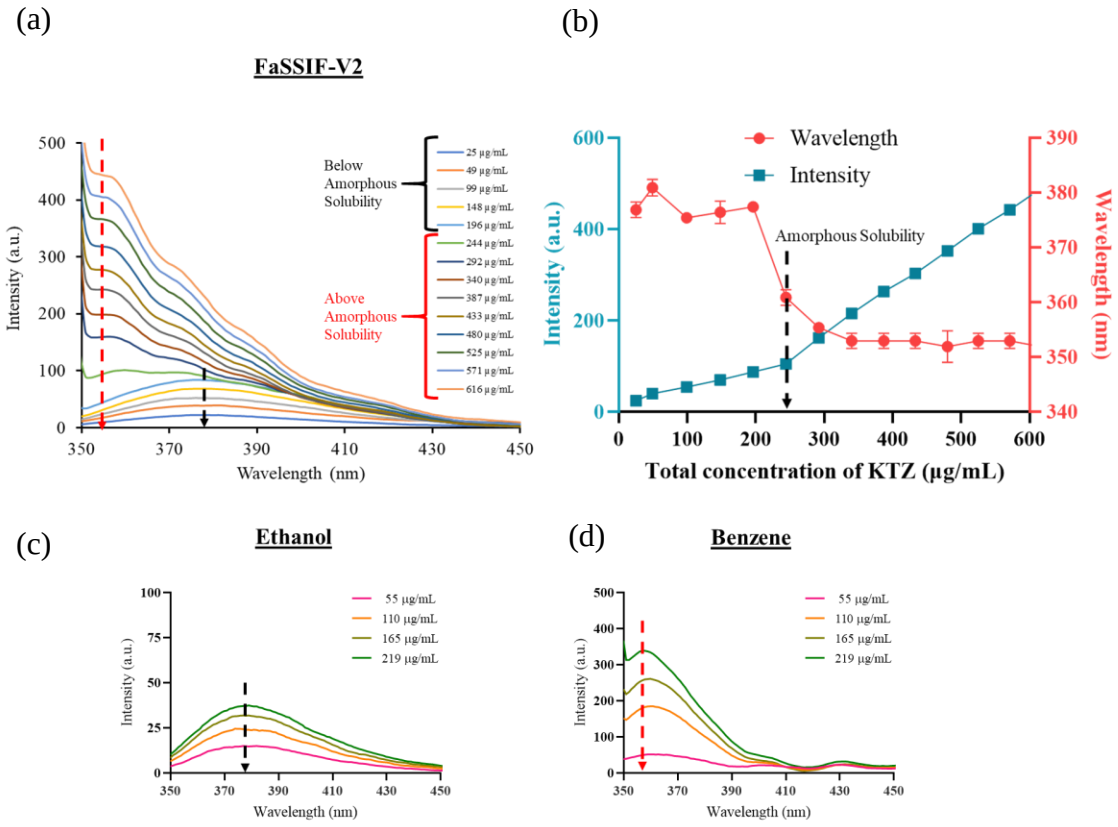

Figure A4. (a) Fluorescence emission spectra of auto-fluorescent KTZ solutions in FaSSIF-V2 media at concentration ranging from 25 to 616 µg/mL. **(b)** Abrupt increase in KTZ fluorescence intensity and decrease in emission maxima around amorphous solubility concentration (235 µg/mL) of KTZ in FaSSIF-V2 as the medium becomes increasingly non-polar upon LLPS. **(c)** Fluorescence emission spectra of KTZ in relatively polar ethanol simulating KTZ environment before LLPS and, **(d)** non-polar benzene simulating KTZ environment after LLPS.

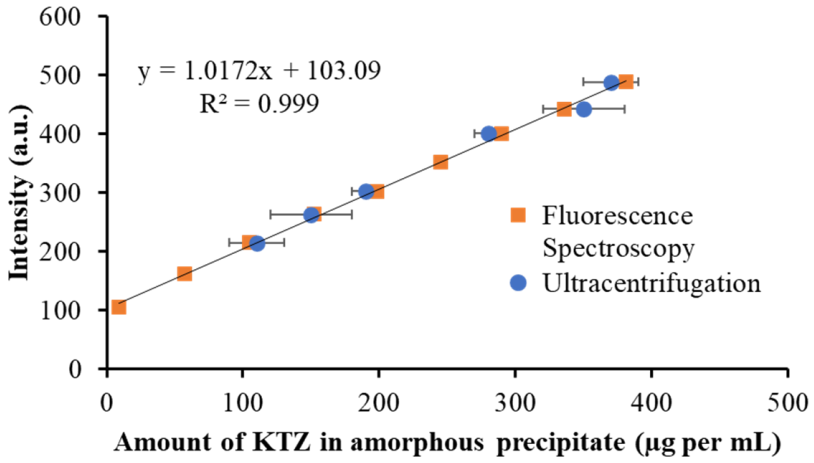

Figure A5. Calibration curve to determine mass of amorphous precipitate generated upon ASD dissolution obtained by plotting fluorescence intensity as a function of mass of KTZ amorphous precipitate determined by mass balance and independently by ultracentrifugation of reference supersaturated solutions and weighing the precipitate.

BIBLIOGRAPHY

1. Lipinski CA, Lombardo F, Dominy BW, Feeney PJ. Experimental and computational approaches to estimate solubility and permeability in drug discovery and development settings. *Adv Drug Deliv Rev*. 2012;64:4-17.

2. Dahan A, Miller JM, Amidon GL. Prediction of solubility and permeability class membership: Provisional BCS classification of the world's top oral drugs. *AAPS J*. 2009;11(4):740-746.

3. Ting JM, Porter WW, Mecca JM, Bates FS, Reineke TM. Advances in Polymer Design for Enhancing Oral Drug Solubility and Delivery. *Bioconjug Chem*. 2018;29(4):939-952.

4. Waring MJ, Arrowsmith J, Leach AR, et al. An analysis of the attrition of drug candidates from four major pharmaceutical companies. *Nat Rev Drug Discov*. 2015;14(7):475-486.

5. Qian K, Stella L, Jones DS, Andrews GP, Du H, Tian Y. Drug-Rich Phases Induced by Amorphous Solid Dispersion: Arbitrary or Intentional Goal in Oral Drug Delivery? *Pharmaceutics*. 2021;13(6):889.

6. Taylor LS, Zhang GGZ. Physical chemistry of supersaturated solutions and implications for oral absorption. *Adv Drug Deliv Rev*. 2016;101:122-142.

7. Williams HD, Trevaskis NL, Charman SA, et al. Strategies to address low drug solubility in discovery and development. *Pharmacol Rev*. 2013;65(1):315-499.

8. Poelma FGJ, Breäs R, Tukker JJ, Crommelin DJA. Intestinal Absorption of Drugs. The Influence of Mixed Micelles on on the Disappearance Kinetics of Drugs from the Small Intestine of the Rat. *J Pharm Pharmacol*. 1991;43(5):317-324.

9. Katneni K, Charman SA, Porter CJH. Permeability assessment of poorly water-soluble compounds under solubilizing conditions: The reciprocal permeability approach. *J Pharm Sci*. 2006;95(10):2170-2185.

10. Miller JM, Beig A, Krieg BJ, et al. The solubility-permeability interplay: Mechanistic modeling and predictive application of the impact of micellar solubilization on intestinal permeation. *Mol Pharm*. 2011;8(5):1848-1856.

11. Miller JM, Beig A, Carr RA, Webster GK, Dahan A. The solubility-permeability interplay when using cosolvents for solubilization: Revising the way we use solubility-enabling formulations. *Mol Pharm*. 2012;9(3):581-590.

12. Dahan A, Miller JM, Hoffman A, Amidon GE, Amidon GL. The solubility-permeability interplay in using cyclodextrins as pharmaceutical solubilizers: Mechanistic modeling and application to progesterone. *J Pharm Sci*. 2010;99(6):2739-2749.

13. Dahan A, Miller JM. The solubility-permeability interplay and its implications in formulation design and development for poorly soluble drugs. *AAPS J*.

2012;14(2):244-251.

14. Raina SA, Zhang GGZ, Alonzo DE, et al. Impact of Solubilizing Additives on Supersaturation and Membrane Transport of Drugs. *Pharm Res*. 2015;32(10):3350-3364.

15. Threlfall T. Structural and Thermodynamic Explanations of Ostwald's Rule. *Org Process Res Dev*. 2003;7(6):1017-1027.

16. Du Y, Wang H, Du S, et al. The liquid-liquid phase separation and crystallization of vanillin in 1-propanol/water solution. *Fluid Phase Equilib*. 2016;409:84-91.

17. Revalor E, Bottini O, Hoff C. Communications to the Editor Crystallization in the Presence of a Liquid-Liquid Phase Separation Abstract : *Org Process Res Dev*. 2006;(3):2183-2187.

18. Hancock BC, Parks M. What is the true solubility advantage for amorphous pharmaceuticals? *Pharm Res*. 2000;17(4):397-404.

19. Xiong X, Xu K, Du Q, et al. Effects of Temperature and Solvent on the Solid-State Transformations of Pranlukast During Mechanical Milling. *J Pharm Sci*. 2017;106(6):1680-1687.

20. Huang Y, Dai W-G. Fundamental aspects of solid dispersion technology for poorly soluble drugs. *Acta Pharm Sin B*. 2014;4(1):18-25.

21. Baghel S, Cathcart H, O'Reilly NJ. Polymeric Amorphous Solid Dispersions: A Review of Amorphization, Crystallization, Stabilization, Solid-State Characterization, and Aqueous Solubilization of Biopharmaceutical Classification System Class II Drugs. *J Pharm Sci*. 2016;105(9):2527-2544.

22. Mosquera-Giraldo LI, Taylor LS. Glass-liquid phase separation in highly supersaturated aqueous solutions of telaprevir. *Mol Pharm*. 2015;12(2):496-503.

23. Jackson MJ, Kestur US, Hussain MA, Taylor LS. Dissolution of Danazol Amorphous Solid Dispersions: Supersaturation and Phase Behavior as a Function of Drug Loading and Polymer Type. *Mol Pharm*. 2016;13(1):223-231.

24. Wilson V, Lou X, Osterling DJ, et al. Relationship between amorphous solid dispersion In Vivo absorption and In Vitro dissolution: phase behavior during dissolution, speciation, and membrane mass transport. *J Control Release*. 2018;292(August):172-182.

25. Indulkar AS, Gao Y, Raina SA, Zhang GGZ, Taylor LS. Exploiting the Phenomenon of Liquid-Liquid Phase Separation for Enhanced and Sustained Membrane Transport of a Poorly Water-Soluble Drug. *Mol Pharm*. 2016;13(6):2059-2069.

26. Jackson MJ, Toth SJ, Kestur US, et al. Impact of polymers on the precipitation behavior of highly supersaturated aqueous danazol solutions. *Mol Pharm*. 2014;11(9):3027-3038.

27. Ricarte RG, Li Z, Johnson LM, et al. Direct Observation of Nanostructures during

Aqueous Dissolution of Polymer/Drug Particles. *Macromolecules*. 2017;50(8):3143-3152.

28. Zhao Z, Katai H, Higashi K, Ueda K, Kawakami K, Moribe K. Cryo-TEM and AFM Observation of the Time-Dependent Evolution of Amorphous Probucol Nanoparticles Formed by the Aqueous Dispersion of Ternary Solid Dispersions. *Mol Pharm*. 2019;16(5):2184-2198.

29. Egami K, Higashi K, Yamamoto K, Moribe K. Crystallization of Probucol in Nanoparticles Revealed by AFM Analysis in Aqueous Solution. *Mol Pharm*. 2015;12(8):2972-2980.

30. Ueda K, Higashi K, Moribe K. Direct NMR Monitoring of Phase Separation Behavior of Highly Supersaturated Nifedipine Solution Stabilized with Hypromellose Derivatives. *Mol Pharm*. 2017;14(7):2314-2322.

31. Ueda K, Taylor LS. Polymer Type Impacts Amorphous Solubility and Drug-Rich Phase Colloidal Stability: A Mechanistic Study Using Nuclear Magnetic Resonance Spectroscopy. *Mol Pharm*. 2020;17(4):1352-1362.

32. Jha PK, Larson RG. Assessing the efficiency of polymeric excipients by atomistic molecular dynamics simulations. *Mol Pharm*. 2014;11(5):1676-1686.

33. Shore, Parkhurst A., Bernard B. Brodie and CAMH. The Gastric Secretion of Drugs: A pH-Partition Hypothesis. *J Pharmacol Exp Ther*. 1957;119(3):361-369.

34. Gray V, Kelly G, Xia M, Butler C, Thomas S, Mayock S. The science of USP 1 and 2 dissolution: Present challenges and future relevance. *Pharm Res*. 2009;26(6):1289-1302.

35. Zaborenko N, Shi Z, Corredor CC, et al. First-Principles and Empirical Approaches to Predicting In Vitro Dissolution for Pharmaceutical Formulation and Process Development and for Product Release Testing. *AAPS J*. 2019;21(3).

36. Cook AJ. Development strategies for IVIVC in an industrial environment. *Biopharm Drug Dispos*. 2012;33(3):349-353.

37. Bai G, Armenante PM, Plank R V., Gentzler M, Ford K, Harmon P. Hydrodynamic investigation of USP dissolution test apparatus II. *J Pharm Sci*. 2007;96(9):2327-2349.

38. Fuchs A, Leigh M, Kloefer B, Dressman JB. Advances in the design of fasted state simulating intestinal fluids: FaSSIF-V3. *Eur J Pharm Biopharm*. 2015;94:229-240.

39. Klumpp L, Leigh M, Dressman J. Dissolution behavior of various drugs in different FaSSIF versions. *Eur J Pharm Sci*. 2020;142(August 2019):105138.

40. Hate SS, Reutzel-Edens SM, Taylor LS. Insight into Amorphous Solid Dispersion Performance by Coupled Dissolution and Membrane Mass Transfer Measurements. *Mol Pharm*. 2019;16(1):448-461.

41. Stricker H. *In Vitro Studies on the Dissolution and Absorption Behaviour of Orally*

Administered Drugs, and the Connection To Their Bioavailability. Elsevier/North-Holland Biomedical Press; 1976.

42. Gao Z. In vitro dissolution testing with flow-through method: A technical note. *AAPS PharmSciTech*. 2009;10(4):1401-1405.

43. Van Eerdenbrugh B, Alonzo DE, Taylor LS. Influence of particle size on the ultraviolet spectrum of particulate-containing solutions: Implications for in-situ concentration monitoring using UV/Vis fiber-optic probes. *Pharm Res*. 2011;28(7):1643-1652.

44. Ginski MJ, Polli JE. Prediction of dissolution-absorption relationships from a dissolution/Caco-2 system. *Int J Pharm*. 1999;177(1):117-125.

45. Kataoka M, Takeyama S, Minami K, et al. In vitro assessment of supersaturation/precipitation and biological membrane permeation of poorly water-soluble drugs: a case study with albendazole and ketoconazole. *J Pharm Sci*. 2019:1-8.

46. Kataoka M, Yano K, Hamatsu Y, Masaoka Y, Sakuma S, Yamashita S. Assessment of absorption potential of poorly water-soluble drugs by using the dissolution/permeation system. *Eur J Pharm Biopharm*. 2013;85(3 PART B):1317-1324.

47. Kataoka M, Tsuneishi S, Maeda Y, Masaoka Y, Sakuma S, Yamashita S. A new in vitro system for evaluation of passive intestinal drug absorption: Establishment of a double artificial membrane permeation assay. *Eur J Pharm Biopharm*. 2014;88(3):840-846.

48. Kataoka M, Masaoka Y, Sakuma S, Yamashita S. Effect of food intake on the oral absorption of poorly water-soluble drugs: In vitro assessment of drug dissolution and permeation assay system. *J Pharm Sci*. 2006;95(9):2051-2061.

49. Motz SA, Schaefer UF, Balbach S, Eichinger T, Lehr CM. Permeability assessment for solid oral drug formulations based on Caco-2 monolayer in combination with a flow through dissolution cell. *Eur J Pharm Biopharm*. 2007;66(2):286-295.

50. Bibi HA, Di Cagno M, Holm R, Bauer-Brandl A. Permeapad^{TM} for investigation of passive drug permeability: The effect of surfactants, co-solvents and simulated intestinal fluids (FaSSIF and FeSSIF). *Int J Pharm*. 2015;493(1-2):192-197.

51. Berben P, Bauer-Brandl A, Brandl M, et al. Drug permeability profiling using cell-free permeation tools: Overview and applications. *Eur J Pharm Sci*. 2018;119(March):219-233.

52. Kerns EH, Di L, Petusky S, Farris M, Ley R, Jupp P. Combined application of parallel artificial membrane permeability assay and Caco-2 permeability assays in drug discovery. *J Pharm Sci*. 2004;93(6):1440-1453.

53. Kansy M, Senner F, Gubernator K. Screening : Parallel Artificial Membrane Permeation Assay in the Description of. *J Med Chem*. 1998;41(7):1007-1010.

54. Avdeef A, Bendels S, Di L, et al. PAMPA - Critical factors for better predictions of absorption. *J Pharm Sci*. 2007;96(11):2893-2909.

55. Raina SA, Zhang GGZ, Alonzo DE, et al. Enhancements and limits in drug membrane transport using supersaturated solutions of poorly water soluble drugs. *J Pharm Sci*. 2014;103(9):2736-2748.

56. Indulkar AS, Gao Y, Raina SA, Zhang GGZ, Taylor LS. Exploiting the Phenomenon of Liquid-Liquid Phase Separation for Enhanced and Sustained Membrane Transport of a Poorly Water-Soluble Drug. *Mol Pharm*. 2016;13(6):2059-2069.

57. Berben P, Brouwers J, Augustijns P. The artificial membrane insert system as predictive tool for formulation performance evaluation. *Int J Pharm*. 2018;537(1-2):22-29.

58. Sironi D, Rosenberg J, Bauer-Brandl A, Brandl M. Dynamic dissolution-/permeation-testing of nano- and microparticle formulations of fenofibrate. *Eur J Pharm Sci*. 2017;96:20-27.

59. Borbás E, Kádár S, Tsinman K, et al. Prediction of Bioequivalence and Food Effect Using Flux- and Solubility-Based Methods. *Mol Pharm*. 2019;16(10):4121-4130.

60. Minekus, Mans, Phillipe Marteau, Robert Havenaar and JHH in'T. V. A Multicompartme ntal Dynamic Computer- controlled Model Simulating the Stomach and Small Intestine. *Altern to Lab Anim*. 1995;23(2):197-209.

61. McAllister M. Dynamic dissolution: A step closer to predictive dissolution testing? *Mol Pharm*. 2010;7(5):1374-1387.

62. Blanquet S, Zeijdner E, Beyssac E, et al. A dynamic artificial gastrointestinal system for studying the behavior of orally administered drug dosage forms under various physiological conditions. *Pharm Res*. 2004;21(4):585-591.

63. Hate SS, Reutzel-Edens SM, Taylor LS. Absorptive Dissolution Testing of Supersaturating Systems: Impact of Absorptive Sink Conditions on Solution Phase Behavior and Mass Transport. *Mol Pharm*. 2017;14(11):4052-4063.

64. Hate SS, Reutzel-Edens SM, Taylor LS. Absorptive Dissolution Testing: An Improved Approach to Study the Impact of Residual Crystallinity on the Performance of Amorphous Formulations. *J Pharm Sci*. 2020;109(3):1312-1323.

65. Hate SS, Reutzel-Edens SM, Taylor LS. Interplay of Adsorption, Supersaturation and the Presence of an Absorptive Sink on Drug Release from Mesoporous Silica-Based Formulations. *Pharm Res*. 2020;37(8).

66. Zheng JM, Xu ZK, Li JM, Wang SY, Xu YY. Influence of random arrangement of hollow fiber membranes on shell side mass transfer performance: A novel model prediction. *J Memb Sci*. 2004;236(1-2):145-151.

67. Fung M, Bērziņš K, Suryanarayanan R. Physical Stability and Dissolution Behavior of Ketoconazole-Organic Acid Coamorphous Systems. *Mol Pharm*. 2018;15(5):1862-1869.

68. Dressman JB, Krämer J, editors. Pharmaceutical dissolution testing. Boca Raton, FL:: Taylor & Francis; 2005

69. Löbenberg R, Krämer J, Shah VP, Amidon GL, Dressman JB. Dissolution testing as a prognostic tool for oral drug absorption: Dissolution behavior of glibenclamide. *Pharm Res*. 2000;17(4):439-444.

70. Wendelboe J, Knopp MM, Khan F, Chourak N, Rades T, Holm R. Importance of in vitro dissolution conditions for the in vivo predictability of an amorphous solid dispersion containing a pH-sensitive carrier. *Int J Pharm*. 2017;531(1):324-331.

71. Dharani S, Barakh Ali SF, Afrooz H, Khan MA, Rahman Z. Development and Validation of a Discriminatory Dissolution Method for Rifaximin Products. *J Pharm Sci*. 2019;108(6):2112-2118.

72. Pudipeddi M, Serajuddin ATM. Trends in solubility of polymorphs. *J Pharm Sci*. 2005;94(5):929-939.

73. Duggirala NK, Perry ML, Almarsson Ö, Zaworotko MJ. Pharmaceutical cocrystals: Along the path to improved medicines. *Chem Commun*. 2016;52(4):640-655.

74. Elder DP, Holm R, De Diego HL. Use of pharmaceutical salts and cocrystals to address the issue of poor solubility. *Int J Pharm*. 2013;453(1):88-100.

75. Shono Y, Jantratid E, Dressman JB. Precipitation in the small intestine may play a more important role in the in vivo performance of poorly soluble weak bases in the fasted state: Case example nelfinavir. *Eur J Pharm Biopharm*. 2011;79(2):349-356.

76. Kostewicz ES, Wunderlich M, Brauns U, Becker R, Bock T, Dressman JB. Predicting the precipitation of poorly soluble weak bases upon entry in the small intestine. *J Pharm Pharmacol*. 2004;56(1):43-51.

77. Psachoulias D, Vertzoni M, Goumas K, et al. Precipitation in and supersaturation of contents of the upper small intestine after administration of two weak bases to fasted adults. *Pharm Res*. 2011;28(12):3145-3158.

78. Adhikari A, Polli JE. Characterization of Grades of HPMCAS Spray Dried Dispersions of Itraconazole Based on Supersaturation Kinetics and Molecular Interactions Impacting Formulation Performance. *Pharm Res*. 2020;37(10):4-7.

79. Li J, Tsinman K, Tsinman O, Wigman L. Using pH Gradient Dissolution with In-Situ Flux Measurement to Evaluate Bioavailability and DDI for Formulated Poorly Soluble Drug Products. *AAPS PharmSciTech*. 2018;19(7):2898-2907.

80. Hate SS, Reutzel-Edens SM, Taylor LS. Absorptive Dissolution Testing of Supersaturating Systems: Impact of Absorptive Sink Conditions on Solution Phase Behavior and Mass Transport. *Mol Pharm*. 2017;14(11):4052-4063.

81. Higaki K, Choe SY, Löbenberg R, Welage LS, Amidon GL. Mechanistic understanding of time-dependent oral absorption based on gastric motor activity in humans. *Eur J Pharm Biopharm*. 2008;70(1):313-325.

82. Suarez-Sharp S, Li M, Duan J, Shah H, Seo P. Regulatory Experience with In Vivo In Vitro Correlations (IVIVC) in New Drug Applications. *AAPS J*. 2016;18(6):1379-1390.

83. Dickinson PA, Rmaileh RA, Ashworth L, et al. An investigation into the utility of a multi-compartmental, dynamic, system of the upper gastrointestinal tract to support formulation development and establish bioequivalence of poorly soluble drugs. *AAPS J*. 2012;14(2):196-205.

84. Carlert S, Pålsson A, Hanisch G, et al. Predicting intestinal precipitation-A case example for a basic BCS class II drug. *Pharm Res*. 2010;27(10):2119-2130.

85. Linnankoski J, Ranta VP, Yliperttula M, Urtti A. Passive oral drug absorption can be predicted more reliably by experimental than computational models-Fact or myth. *Eur J Pharm Sci*. 2008;34(2-3):129-139.

86. Davies NM, Takemoto JK, Brocks DR, Yáñez JA. Multiple peaking phenomena in pharmacokinetic disposition. *Clin Pharmacokinet*. 2010;49(6):351-377.

87. Kambayashi A, Blume H, Dressman J. Understanding the in vivo performance of enteric coated tablets using an in vitro-in silico-in vivo approach: Case example diclofenac. *Eur J Pharm Biopharm*. 2013;85(3 PART B):1337-1347.

88. Sun DD, Lee PI. Haste Makes Waste: The Interplay Between Dissolution and Precipitation of Supersaturating Formulations. *AAPS J*. 2015;17(6):1317-1326.

89. Williams III RO, Watts AB, Miller DA, editors. Formulating poorly water soluble drugs. Springer; 2016

90. Taylor LS, Zhang GGZ. Physical chemistry of supersaturated solutions and implications for oral absorption. *Adv Drug Deliv Rev*. 2016;101:122-142.

91. Pudipeddi M, Serajuddin ATM. Trends in solubility of polymorphs. *J Pharm Sci*. 2005;94(5):929-939.

92. Hou H, Siegel RA. Enhanced permeation of diazepam through artificial membranes from supersaturated solutions. *J Pharm Sci*. 2006;95(4):896-905.

93. Terebetski JL, Cummings JJ, Fauty SE, Michniak-Kohn B. Combined use of crystalline sodium salt and polymeric precipitation inhibitors to improve pharmacokinetic profile of ibuprofen through supersaturation. *AAPS PharmSciTech*. 2014;15(5):1334-1344.

94. Childs SL, Kandi P, Lingireddy SR. Formulation of a danazol cocrystal with controlled supersaturation plays an essential role in improving bioavailability. *Mol Pharm*. 2013;10(8):3112-3127.

95. Stewart AM, Grass ME, Brodeur TJ, et al. Impact of Drug-Rich Colloids of Itraconazole and HPMCAS on Membrane Flux in Vitro and Oral Bioavailability in Rats. *Mol Pharm*. 2017;14(7):2437-2449.

96. Purohit HS, Trasi NS, Osterling DJ, et al. Assessing the Impact of Endogenously

Derived Crystalline Drug on the in Vivo Performance of Amorphous Formulations. *Mol Pharm*. 2019;16(8):3617-3625.

97. Unger EF. Weighing Benefits and Risks — The FDA's Review of Prasugrel. *N Engl J Med*. 2009;361(10):942-945.

98. Psachoulias D, Vertzoni M, Butler J, et al. An in vitro methodology for forecasting luminal concentrations and precipitation of highly permeable lipophilic weak bases in the fasted upper small intestine. *Pharm Res*. 2012;29(12):3486-3498.

99. Knopp MM, Chourak N, Khan F, et al. Effect of polymer type and drug dose on the in vitro and in vivo behavior of amorphous solid dispersions. *Eur J Pharm Biopharm*. 2016;105:106-114.

100. Sun DD, Wen H, Taylor LS. Non-Sink Dissolution Conditions for Predicting Product Quality and In Vivo Performance of Supersaturating Drug Delivery Systems. *J Pharm Sci*. 2016;105(9):2477-2488.

101. Mosquera-Giraldo LI, Taylor LS. Glass-liquid phase separation in highly supersaturated aqueous solutions of telaprevir. *Mol Pharm*. 2015;12(2):496-503.

102. Ilevbare GA, Taylor LS. Liquid-liquid phase separation in highly supersaturated aqueous solutions of poorly water-soluble drugs: Implications for solubility enhancing formulations. *Cryst Growth Des*. 2013;13(4):1497-1509.

103. Ruff A, Fiolka T, Kostewicz ES. Prediction of Ketoconazole absorption using an updated in vitro transfer model coupled to physiologically based pharmacokinetic modelling. *Eur J Pharm Sci*. 2017;100:42-55.

104. Kambayashi A, Yasuji T, Dressman JB. Prediction of the precipitation profiles of weak base drugs in the small intestine using a simplified transfer ("dumping") model coupled with in silico modeling and simulation approach. *Eur J Pharm Biopharm*. 2016;103:95-103.

105. Mudie, Deanna M., Yi Shi, Haili Ping, Ping Gao, Gordon L. Amidon and GEA. Mechanistic analysis of solute transport in an in vitro physiological two-phase dissolution apparatus. *Biopharm Drug Dispos*. 2012;33(7):378-402.

106. Van Eerdenbrugh B, Raina S, Hsieh YL, Augustijns P, Taylor LS. Classification of the crystallization behavior of amorphous active pharmaceutical ingredients in aqueous environments. *Pharm Res*. 2014;31(4):969-982.

107. Brown HS, Ito K, Galetin A, Houston JB. Prediction of in vivo drug-drug interactions from in vitro data: Impact of incorporating parallel pathways of drug elimination and inhibitor absorption rate constant. *Br J Clin Pharmacol*. 2005;60(5):508-518.

108. Jede C, Wagner C, Kubas H, Weber C, Weitschies W. In-line derivative spectroscopy as a promising application to a small-scale in vitro transfer model in biorelevant supersaturation and precipitation testing. *J Pharm Pharmacol*. 2018;70(10):1315-1323.

109. Rautiola D, Cloyd JC, Siegel RA. Conversion of a soluble diazepam prodrug to supersaturated diazepam for rapid intranasal delivery: Kinetics and stability. *J Control Release*. 2018;289(August):1-9.

110. Greco K, Bogner R. Solution-mediated phase transformation: Significance during dissolution and implications for bioavailability. *J Pharm Sci*. 2012;101(9):2996-3018.

111. Micali N, Mallamace F, Castriciano M, Romeo A, Scolaro LM. Separation of scattering and absorption contributions in UV/visible spectra of resonant systems. *Anal Chem*. 2001;73(20):4958-4963.

112. Bohren CF. Absorption and scattering of light by small particles. *Absorpt Scatt Light by small Part*. 1983.

113. Huang Y -C, Colaizzi JL, Bierman RH, Woestenborghs R, Heykants JJP. Pharmacokinetics and Dose Proportionality of Domperidone in Healthy Volunteers. *J Clin Pharmacol*. 1986;26(8):628-632.

114. Elkhabaz A, Moseson DE, Brouwers J, Augustijns P, Taylor LS. Interplay of Supersaturation and Solubilization: Lack of Correlation between Concentration-Based Supersaturation Measurements and Membrane Transport Rates in Simulated and Aspirated Human Fluids. *Mol Pharm*. 2019;(1).

115. Reuben BG, Perl O, Morgan NL, Stratford P, Dudley LY, Hawes C. Phospholipid coatings for the prevention of membrane fouling. *J Chem Technol Biotechnol*. 1995;63(1):85-91.

116. Frank KJ, Westedt U, Rosenblatt KM, et al. What is the mechanism behind increased permeation rate of a poorly soluble drug from aqueous dispersions of an amorphous solid dispersion? *J Pharm Sci*. 2014;103(6):1779-1786.

117. Saboo S, Moseson DE, Kestur US, Taylor LS. Patterns of drug release as a function of drug loading from amorphous solid dispersions: A comparison of five different polymers. *Eur J Pharm Sci*. 2020;155(August):105514.

118. Gautschi JT. Nonsink In Vitro Dissolution Testing of Amorphous Solid Dispersions. 2013:205-220.

119. Deng Y, Liang Q, Wang Y, Zhang X, Yan C, He Y. The inhibiting role of hydroxypropylmethylcellulose acetate succinate on piperine crystallization to enhance its dissolution from its amorphous solid dispersion and permeability. *RSC Adv*. 2019;9(67):39523-39531.

120. Jackson MJ, Kestur US, Hussain MA, Taylor LS. Dissolution of Danazol Amorphous Solid Dispersions: Supersaturation and Phase Behavior as a Function of Drug Loading and Polymer Type. *Mol Pharm*. 2016;13(1):223-231.

121. Sugano K, Kataoka M, da Costa Mathews C, Yamashita S. Prediction of food effect by bile micelles on oral drug absorption considering free fraction in intestinal fluid. *Eur J Pharm Sci*. 2010;40(2):118-124.

122. Stricker H. *In Vitro Studies on the Dissolution and Absorption Behaviour of Orally Administered Drugs, and the Connection To Their Bioavailability*. Elsevier/North-Holland Biomedical Press; 1976.

123. Phillips DJ, Pygall SR, Cooper VB, Mann JC. Overcoming sink limitations in dissolution testing: A review of traditional methods and the potential utility of biphasic systems. *J Pharm Pharmacol*. 2012;64(11):1549-1559.

124. Sinko PD, Harris S, Salehi N, Meyer PJ, Amidon GL, Amidon GE. Ultrathin, Large-Area Membrane Diffusion Cell for pH-Dependent Simultaneous Dissolution and Absorption Studies. *Mol Pharm*. 2020;17(7):2319-2328.

125. Borbás E, Sinkó B, Tsinman O, et al. Investigation and mathematical description of the real driving force of passive transport of drug molecules from supersaturated solutions. *Mol Pharm*. 2016;13(11):3816-3826.

126. Tsinman K, Tsinman O, Lingamaneni R, et al. Ranking Itraconazole Formulations Based on the Flux through Artificial Lipophilic Membrane. *Pharm Res*. 2018;35(8).

127. Chiang PC, Nagapudi K, Liu J, et al. An Integrated Analysis of Solid Form Change Impact on Solubility and Permeability: Case Study of Oral Exposure in Rats of an RAR Related Orphan Receptor C Inhibitor. *J Pharm Sci*. 2019;108(7):2256-2263.

128. Ueda K, Higashi K, Limwikrant W, et al. Mechanistic differences in permeation behavior of supersaturated and solubilized solutions of carbamazepine revealed by nuclear magnetic resonance measurements. *Mol Pharm*. 2012;9(11):3023-3033.

129. Berben P, Bauer-Brandl A, Brandl M, et al. Drug permeability profiling using cell-free permeation tools: Overview and applications. *Eur J Pharm Sci*. 2018;119(March):219-233.

130. Bibi HA, Di Cagno M, Holm R, Bauer-Brandl A. Permeapad™ for investigation of passive drug permeability: The effect of surfactants, co-solvents and simulated intestinal fluids (FaSSIF and FeSSIF). *Int J Pharm*. 2015;493(1-2):192-197.

131. Chen Y, Wang S, Wang S, et al. Initial Drug Dissolution from Amorphous Solid Dispersions Controlled by Polymer Dissolution and Drug-Polymer Interaction. *Pharm Res*. 2016;33(10):2445-2458.

132. Cristofoletti R, Dressman JB. Matching phosphate and maleate buffer systems for dissolution of weak acids: Equivalence in terms of buffer capacity of bulk solution or surface pH? *Eur J Pharm Biopharm*. 2016;103:104-108.

133. Jantratid E, Janssen N, Reppas C, Dressman JB. Dissolution media simulating conditions in the proximal human gastrointestinal tract: An update. *Pharm Res*. 2008;25(7):1663-1676.

134. Brown HS, Ito K, Galetin A, Houston JB. Prediction of in vivo drug-drug interactions from in vitro data: Impact of incorporating parallel pathways of drug elimination and inhibitor absorption rate constant. *Br J Clin Pharmacol*. 2005;60(5):508-518.

135. Wilson V, Lou X, Osterling DJ, et al. Relationship between amorphous solid dispersion In Vivo absorption and In Vitro dissolution: phase behavior during dissolution, speciation, and membrane mass transport. *J Control Release*. 2018;292(November):172-182.

136. Ueda K, Higashi K, Moribe K. Mechanistic elucidation of formation of drug-rich amorphous nanodroplets by dissolution of the solid dispersion formulation. *Int J Pharm*. 2019;561(December 2018):82-92.

137. Raina SA, Alonzo DE, Zhang GGZ, Gao Y, Taylor LS. Using Environment-Sensitive Fluorescent Probes to Characterize Liquid-Liquid Phase Separation in Supersaturated Solutions of Poorly Water Soluble Compounds. *Pharm Res*. 2015;32(11):3660-3673.

138. Sahoo A, Kumar NSK, Suryanarayanan R. Crosslinking: An avenue to develop stable amorphous solid dispersion with high drug loading and tailored physical stability. *J Control Release*. 2019;311-312(September):212-224.

139. Ueda K, Hate SS, Taylor LS. Impact of Hypromellose Acetate Succinate Grade on Drug Amorphous Solubility and In Vitro Membrane Transport. *J Pharm Sci*. 2020;109(8):2464-2473.

140. Chen Y, Liu C, Chen Z, et al. Drug-polymer-water interaction and its implication for the dissolution performance of amorphous solid dispersions. *Mol Pharm*. 2015;12(2):576-589.

141. Friesen, Dwayne T., Ravi Shanker, Marshall Crew, Daniel T. Smithey, W. J. Curatolo and JASN. Hydroxypropyl Methylcellulose Acetate Succinate-Based Spray-Dried Dispersions: An Overview. *Mol Pharm*. 2008;5(6):1003-1019.

142. Wang S, Liu C, Chen Y, Zhu A, Qian F. Aggregation of Hydroxypropyl Methylcellulose Acetate Succinate under Its Dissolving pH and the Impact on Drug Supersaturation. *Mol Pharm*. 2018;15(10):4643-4653.

143. Adachi M, Hinatsu Y, Kusamori K, et al. Improved dissolution and absorption of ketoconazole in the presence of organic acids as pH-modifiers. *Eur J Pharm Sci*. 2015;76:225-230.

144. Ueda K, Yamamoto N, Higashi K, Moribe K. Molecular Mobility Suppression of Ibuprofen-Rich Amorphous Nanodroplets by HPMC Revealed by NMR Relaxometry and Its Significance with Respect to Crystallization Inhibition. *Mol Pharm*. 2019;16(12):4968-4977.

145. Lubach JW, Chen JZ, Hau J, et al. Investigation of the rat model for preclinical evaluation of pH-dependent oral absorption in humans. *Mol Pharm*. 2013;10(11):3997-4004.

146. Indulkar AS, Mo H, Gao Y, Raina SA, Zhang GGZ, Taylor LS. Impact of Micellar Surfactant on Supersaturation and Insight into Solubilization Mechanisms in Supersaturated Solutions of Atazanavir. *Pharm Res*. 2017;34(6):1276-1295.

147. Saboo S, Mugheirbi NA, Zemlyanov DY, Kestur US, Taylor LS. Congruent release

of drug and polymer: A “sweet spot” in the dissolution of amorphous solid dispersions. *J Control Release*. 2019;298(January):68-82.

148. Kojima T, Higashi K, Suzuki T, Tomono K, Moribe K, Yamamoto K. Stabilization of a supersaturated solution of mefenamic acid from a solid dispersion with EUDRAGIT® EPO. *Pharm Res*. 2012;29(10):2777-2791.

149. Alonzo DE, Gao Y, Zhou D, Mo H, Zhang GGZ, Taylor LS. Dissolution and precipitation behavior of amorphous solid dispersions. *J Pharm Sci*. 2011;100(8):3316-3331.

150. Matsui K, Tsume Y, Amidon GE, Amidon GL. The Evaluation of In Vitro Drug Dissolution of Commercially Available Oral Dosage Forms for Itraconazole in Gastrointestinal Simulator With Biorelevant Media. *J Pharm Sci*. 2016;105(9):2804-2814.

151. Maincent J, Williams RO. Sustained-release amorphous solid dispersions. *Drug Deliv Transl Res*. 2018;8(6):1714-1725.

152. Sun DD, Lee PI. Evolution of supersaturation of amorphous pharmaceuticals: The effect of rate of supersaturation generation. *Mol Pharm*. 2013;10(11):4330-4346.

153. Kaur P, Jiang X, Duan J, Stier E. Applications of In Vitro–In Vivo Correlations in Generic Drug Development: Case Studies. *AAPS J*. 2015;17(4):1035-1039.

154. Lu Y, Kim S, Park K. In vitro-in vivo correlation: Perspectives on model development. *Int J Pharm*. 2011;418(1):142-148.

155. Fotaki N, Gray V, Kesisoglou F, Mayock S, Mirza T, Salt A, Selen A. Survey results for in vitro-in vivo correlations (IVIVC): critical variables for success. *Dissolution Technol*. 2013;20(2):48-50.

156. Stillhart C, Pepin X, Tistaert C, et al. PBPK Absorption Modeling: Establishing the In Vitro–In Vivo Link—Industry Perspective. *AAPS J*. 2019;21(2).

157. Tuszyński PK, Szlęk J, Polak S, Jachowicz R, Mendyk A. In vitro-in vivo correlation (IVIVC): From current achievements towards the future. *Dissolution Technol*. 2018;25(3):20-27.

158. Bjornsson, Thorir D. and CM. Clinical pharmacokinetics of dipyridamole. *Thromb Res*. 1983;29:93-104.

159. Buchwald P. Direct, differential-equation-based in-vitro–in-vivo correlation (IVIVC) method. *J Pharm Pharmacol*. 2010;55(4):495-504.

160. Roger E, Lagarce F, Benoit JP. The gastrointestinal stability of lipid nanocapsules. *Int J Pharm*. 2009;379(2):260-265.

161. Sugano K. Theoretical investigation of passive intestinal membrane permeability using Monte Carlo method to generate drug-like molecule population. *Int J Pharm*. 2009;373(1-2):55-61.

162. Skolnik S, Lin X, Wang J, Chen XH, He T, Zhang B. Towards prediction of in vivo

intestinal absorption using a 96-well Caco-2 assay. *J Pharm Sci*. 2010;99(7):3246-3265.

163. Sun D, Lennernas H, Welage LS, et al. Comparison of human duodenum and Caco-2 gene expression profiles for 12,000 gene sequences tags and correlation with permeability of 26 drugs. *Pharm Res*. 2002;19(10):1400-1416.

164. Klumpp L, Dressman J. Physiologically based pharmacokinetic model outputs depend on dissolution data and their input: Case examples glibenclamide and dipyridamole. *Eur J Pharm Sci*. 2020;151(May):105380.

165. Matsui K, Tsume Y, Takeuchi S, Searls A, Amidon GL. Utilization of gastrointestinal simulator, an in vivo predictive dissolution methodology, coupled with computational approach to forecast oral absorption of dipyridamole. *Mol Pharm*. 2017;14(4):1181-1189.

166. Pathak SM, Schaefer KJ, Jamei M, Turner DB. Biopharmaceutic IVIVE—Mechanistic Modeling of Single- and Two-Phase In Vitro Experiments to Obtain Drug-Specific Parameters for Incorporation Into PBPK Models. *J Pharm Sci*. 2019;108(4):1604-1618.

167. Rohatgi A. WebPlotDigitizer User Manual 4.3. *(http//arohatgi.info/WebPlotDigitizer/app/ Accessed June 2 2014)*. 2020:1-17.

168. Mudie DM, Murray K, Hoad CL, et al. Quantification of gastrointestinal liquid volumes and distribution following a 240 mL dose of water in the fasted state. *Mol Pharm*. 2014;11(9):3039-3047.

169. McCloy RF, Greenberg GR, Baron JH. Duodenal pH in health and duodenal ulcer disease: Effect of a meal, Coca-Cola, smoking, and cimetidine. *Gut*. 1984;25(4):386-392.

170. Koziolek M, Grimm M, Becker D, et al. Investigation of pH and Temperature Profiles in the GI Tract of Fasted Human Subjects Using the Intellicap® System. *J Pharm Sci*. 2015;104(9):2855-2863.

171. Ayazi S, Leers JM, Oezcelik A, et al. Measurement of gastric pH in ambulatory esophageal pH monitoring. *Surg Endosc*. 2009;23(9):1968-1973.

172. Alhalaweh A, Alzghoul A, Bergström CAS. Molecular Drivers of Crystallization Kinetics for Drugs in Supersaturated Aqueous Solutions. *J Pharm Sci*. 2019;108(1):252-259.

173. Nielsen-Kudsk F, Pedersen AK. Pharmacokinetics of Dipyridamole. *Acta Pharmacol Toxicol (Copenh)*. 1979;44(5):391-399.

174. Mahony C, Wolfram KM, Cocchetto DM, Bjornsson TD. Dipyridamole kinetics. *Clin Pharmacol Ther*. 1982;31(3):330-338.

175. Daneshmend TK, Warnock DW, Turner A, Roberts CJC. Pharmacokinetics of ketoconazole in normal subjects. *J Antimicrob Chemother*. 1981;8(4):299-304.

176. Strindberg S, Plum J, Stie MB, et al. Effect of supersaturation on absorption of indomethacin and tadalafil in a single pass intestinal perfusion rat model, in the absence and presence of a precipitation inhibitor. *Eur J Pharm Biopharm*. 2020;151(April):108-115.

177. Sugano K. Estimation of effective intestinal membrane permeability considering bile micelle solubilisation. *Int J Pharm*. 2009;368(1-2):116-122.

178. Harmon P, Galipeau K, Xu W, Brown C, Wuelfing WP. Mechanism of Dissolution-Induced Nanoparticle Formation from a Copovidone-Based Amorphous Solid Dispersion. *Mol Pharm*. 2016;13(5):1467-1481.

179. Brewster ME, Loftsson T. Cyclodextrins as pharmaceutical solubilizers. *Adv Drug Deliv Rev*. 2007;59(7):645-666.

180. Stewart AM, Grass ME, Mudie DM, Morgen MM, Friesen DT, Vodak DT. Development of a Biorelevant, Material-Sparing Membrane Flux Test for Rapid Screening of Bioavailability-Enhancing Drug Product Formulations. *Mol Pharm*. 2017;14(6):2032-2046.

181. Bao JJ, Liu X, Zhang Y, Li Y. The development of a high-throughput measurement method of octanol/water distribution coefficient based on hollow fiber membrane solvent microextraction technique. *J Chromatogr B Anal Technol Biomed Life Sci*. 2014;967:183-189.

182. Kou D, Zhang C, Yiu H, et al. In Vitro, in Silico, and in Vivo Assessments of Intestinal Precipitation and Its Impact on Bioavailability of a BCS Class 2 Basic Compound. *Mol Pharm*. 2018;15(4):1607-1617.

183. Avdeef A, Nielsen PE, Tsinman O. PAMPA - A drug absorption in vitro model: 11. Matching the in vivo unstirred water layer thickness by individual-well stirring in microtitre plates. *Eur J Pharm Sci*. 2004;22(5):365-374.

184. Lennernäs H. Human intestinal permeability. *J Pharm Sci*. 1998;87(4):403-410.

185. Adson A, Burton PS, Raub TJ, Barsuhn CL, Audus KL, Ho NFH. Passive diffusion of weak organic electrolytes across Caco-2 cell monolayers: Uncoupling the contributions of hydrodynamic, transcellular, and paracellular barriers. *J Pharm Sci*. 1995;84(10):1197-1204.

186. Carino SR, Sperry DC, Hawley M. Relative bioavailability estimation of carbamazepine crystal forms using an artificial stomach-duodenum model. *J Pharm Sci*. 2006;95(1):116-125.